

Process design in laser powder bed fusion: from single to graded multi materials

By

Seyyed Behzad Hosseini Rankouhi

A dissertation submitted in partial fulfillment
of the requirements for the degree of

Doctor of Philosophy
(Mechanical Engineering)

at the

UNIVERSITY OF WISCONSIN – MADISON

2021

Date of final oral examination: 7/28/2021

The dissertation is approved by the following members of the Final Oral Committee:
Frank E. Pfefferkorn, Professor, Mechanical Engineering
Dan J. Thoma, Professor, Materials Science and Engineering
Tim Osswald, Professor, Mechanical Engineering
Kumar Sridharan, Professor, Engineering Physics
Lianyi Chen, Assistant Professor, Mechanical Engineering

Acknowledgments

To my advisors:

Prof. Frank E. Pfefferkorn
Prof. Dan Thoma

To my committee:

Prof. Tim Osswald
Prof. Kumar Sridharan
Prof. Lianyi Chen

To my lab mates:

M³PL Lab Members
ADD Lab Members

Family and Friends

Table of Contents

List of Tables	vi
List of Figures	vii
Nomenclature	ix
Abstract.....	x
Chapter 1: Topology Optimization for Additive Manufacturing	1
1.1. Introduction.....	1
1.2. Materials and methods	4
1.2.1. Mechanical properties characterization	4
1.2.2. Topology optimization	6
1.2.3. Additive manufacturing.....	8
1.2.4. Microstructural characterization.....	10
1.3. Results and analysis.....	10
1.3.1. Tensile test results	10
1.3.2. Clevis TO and mechanical test results	12
1.3.3. Microstructural characterization.....	16
1.4. Discussion	24
1.4.1. Prediction of yield strength based on analysis of AM microstructures.....	25
1.4.2. Additional influence of TO design on strengthening.....	28
1.4.3. Influence of AM on accuracy of FEM predictions.....	29
1.4.4. Potential benefits of AM for TO	30
1.5. Conclusions.....	30
Chapter 2: Dimensional Analysis of SLM Process.....	32
2.1. Introduction.....	32
2.2. Materials and methods	33
2.2.1. Dimensional analysis	33
2.2.2. Additive manufacturing.....	34
2.2.3. Density measurement	35
2.3. Results	35
2.3.1. Dimensionless number.....	35

2.3.2. Predicting porosity modes	36
2.3.3. Universal scaling law	37
2.4. Conclusions	38
Chapter 3: Characterization of Multi-material 316L-Hastelloy X	40
3.1. Introduction	40
3.2. Experimental methods	42
3.2.1. Materials	42
3.2.2. Manufacturing	43
3.2.3. Surface metrology	44
3.2.4. Interfacial characterization	45
3.2.5. Mechanical characterization	45
3.3. Results	46
3.3.1. Surface roughness	46
3.3.2. Interface microstructure	47
3.3.3. Tensile test	51
3.3.4. Flexural test	52
3.3.5. Post-fracture analysis	54
3.4. Discussion	57
3.4.1. The diffusion zone	57
3.4.2. Mechanical properties	59
3.5. Conclusions	60
Chapter 4: Compositional Grading of 316L-Cu Using Machine Learning	62
4.1. Introduction	62
4.2. Materials and Methods	66
4.2.1. Overview	66
4.2.2. Powder characteristics and mixing	68
4.2.3. Additive manufacturing	69
4.2.4. Density measurements	71
4.2.5. Surface roughness	71
4.3. Experimental Data Set	71

4.3.1. Density measurements.....	71
4.3.2. Surface roughness	73
4.4. Multi-variate Gaussian Process Framework.....	75
4.4.1. Modeling framework.....	76
4.4.2. Cross validation.....	79
4.5. Predictions.....	81
4.5.1. Process maps and analysis.....	81
4.5.2. Predicting multi-material process parameters.....	88
4.6. Conclusions.....	90
References	92
Appendices	106
Appendix A – Supplementary figures.....	107
Appendix B – Mixing.....	110
Appendix C – Construction of Covariance Function.....	112

List of Tables

Table 1. Comparison of SS316L tensile properties as reported by machine manufacturer with those given in the literature.	5
Table 2. Examples of possible optimal topologies obtained from select mechanical properties reported in Table 1. Volume fraction is defined as the volume of the original design divided by the volume of the final design.	5
Table 3. EOS M290 main process parameters for SS316L.....	9
Table 4. Chemical composition of SS316L. Nominal values are reported by powder manufacturer while actual values are measured from as-built samples. All values are in wt%.	9
Table 5. Optomec® LENS MR7 main process parameters for SS316L.	10
Table 6. Mechanical properties of SS316L, obtained from tensile test specimens.	11
Table 7. Optimal topologies obtained from mechanical properties of heat-treated SS316L reported in Table 6.....	12
Table 8. Comparison of tensile test results with FEM for topology optimized clevises.....	15
Table 9. Summary of averaged microstructural features that may influence the yield strength.	26
Table 10. Calculated contributions to yield strength based on the Hall-Petch relationship and forest dislocation strengthening, and the difference between calculated estimates and measured values. All values are in (MPa).....	28
Table 11. Process variables appearing in the resulting dimensionless number.....	34
Table 12. Thermophysical properties of metals at room temperature.....	34
Table 13. Chemical composition (in wt %) of 316L and HX powders as provided by the supplier.	42
Table 14. Thermophysical properties of 316L and HX [86,135–137].....	43
Table 15. PBF process parameters for manufacturing of multi-material samples.....	44
Table 16. Summary of influential parameters and properties in multi-material processing of 316L and HX.....	59
Table 17. EOS M290 process parameters for 316L, copper, and compositions thereof used in high throughput design of experiment.	70
Table 18. Mean absolute prediction error of density and surface roughness for all 316L-Cu compositions.	80
Table 19. Predicted parameters and their corresponding density and surface roughness for 316L-Cu multi-material part.....	89

List of Figures

Fig. 1. Tensile test specimen geometry and build direction. Dimensions in (mm).....	5
Fig. 2. Clevis model with critical dimensions and BCs.....	7
Fig. 3. An example of a topology optimized clevis part without imposing manufacturing constraints (a) and with through-cut constraint (b). The TO problem is posed as described in section 2.2.	7
Fig. 4. Engineering stress-strain curves obtained from tensile test specimens. (a) SLM and (b) DED.....	11
Fig. 5. TO designs based on the mechanical properties of (a) heat-treated DED, and (b) heat-treated SLM. (c) Design 'b' is reconstructed for AM using conventional CAD operations. (d) Different views of von Mises stress distribution. Area where maximum von Mises stress occurred is indicated by the arrow.	14
Fig. 6. Clevises manufactured via (a) SLM, and (b) DED. Round ends and holes for DED clevises were later machined to net shape (c).	14
Fig. 7. Clevis tensile test results for (a) SLM and (b) DED fabricated samples, with and without heat treatment.....	15
Fig. 8. Schematic illustrating laser scanning path, grain structure, and microstructural characteristics for (a) SLM and (b) DED fabricated parts.	18
Fig. 9. EBSD orientation maps in the tensile loading direction of initial structures in (a) SLM as-built, (b) SLM heat-treated, (c) DED as-built, and (d) DED heat-treated tensile specimens, with grain boundaries indicated in black. Tensile axis vertical, build direction is out-of-plane. Dashed lines in (c) outline the edges of one laser scan path.....	18
Fig. 10. EBSD orientation maps of initial structures in (a) SLM as-built and (b) DED as-built clevis parts. Colorized according to orientations in the loading direction (vertical).....	20
Fig. 11. Bright-field diffraction-contrast STEM images of dislocation structures in (a) SLM as-built material, with dendritic dislocation cells (dashed lines) and precipitates (arrows), and (b) SLM heat-treated material, with grain boundaries extending diagonally from bottom left to upper right, aligned dislocations extending across grain boundaries indicated by the dashed lines, and precipitates (arrows). Diffraction pattern inset in (b) with spreading of diffraction peaks indicative of 5.7° misorientations between grains.....	23
Fig. 12. Bright-field diffraction-contrast STEM images of dislocation structures in (a) DED as-built material, with extended dislocation walls (parallel to the small dashed line), precipitates (arrows), and dendritic dislocation walls (outlined by the large dashed line) surrounding small, equiaxed dislocation cells. (b) DED heat-treated material with precipitates (arrow), a grain boundary running from top to bottom, and dislocation pileups on $\{111\}$ planes (parallel to the dashed line) near grain boundaries. Inset diffraction patterns in (b) shown for the two grains across the grain boundary.	24
Fig. 13. DfAM decision-making diagram. Arrows indicate the influence of each step on the other. More items can be added to each step as our understanding of the process matures.....	25
Fig. 14. Relative density as a function of dimensionless number Π_1 for select materials and estimation of porosity modes.....	37
Fig. 15. Dimensionless numbers for predicting density in SLM. (a) Dimensionless number Π_1 . (b) Dimensionless number Π_2	39
Fig. 16. Manufactured samples of 316L-HX and HX-316L. Critical dimensions are the same for both tensile and flexural specimens. Tensile test specimens gauge length is 30 mm.	44
Fig. 17. Surface roughness results. (a) Showing the scan locations and directions on samples' surfaces. (b) R_a and S_v values. (c) Surface profile of each scan.....	47
Fig. 18. SEM image of HX-316L interface: (a,d) low magnification overview of the interface, (b) melt pool vortices in the diffusion zone, (c,e) microstructural defects in HX.....	49

Fig. 19. SEM image of 316L-HX interface: (a,d) low magnification overview of the interface, (b) high magnification view of HX microstructure and defects, (c) melt pool vortices in the diffusion zone, and (e) HX dominant microstructure in the diffusion zone.....	50
Fig. 20. EDS line scans of (a) 316L-HX, and (b) HX-316L. The highlighted area indicates the diffusion zone for each multi-material system.....	52
Fig. 21. Tensile test results of 316L, HX, and multi-material samples. (a) stress-strain curves, (b) failed samples. The red dashed lines indicate the interface, (c) comparison of yield and ultimate strengths, and (d) comparison of strains.	53
Fig. 22. Strain map at four critical moments of the tensile test: (a) 316L-HX sample, (b) HX-316L sample. The color scale shows the strain distribution across the sample at every moment during the test.	54
Fig. 23. Flexural test results of 316L, HX, and multi-material samples. (a) stress-strain curves, (b) failed samples. The red dashed lines indicate the interface, (c) comparison of flexural yield and flexural strengths, (d) comparison of strains.	55
Fig. 24. Post-fracture EDS line scans of (a) 316L-HX, and (b) HX-316L. The highlighted area indicates the diffusion zone for each multi-material system.	56
Fig. 25. Post-fracture SEM analysis of multi-material samples at different magnifications: (a,b) 316L-HX, and (c,d) HX-316L. White dashed lines indicate melt pool boundaries at the interface.	56
Fig. 26. SEM image of fracture surfaces from low to high magnification. (a-c) 316L-HX, and (d-f) HX-316L.....	56
Fig. 27. An overview of the proposed method. The hexagonal samples were manufactured using pre-mixed compositions to represent an ideal continuous gradient zone.....	67
Fig. 28. (a) Particle size distribution of 316L and Cu powders. (b) Particle size distribution of 316L-Cu mixtures. (c) SEM image of 316L powder. (d) SEM image of Cu powder.....	68
Fig. 29. Density as a function of volumetric energy density for (a) 316L, (b) Cu, and (c) 316L-Cu compositions.	73
Fig. 30. Surface roughness and waviness as a function of VED for (a) 316L, and (b) Cu.	75
Fig. 31. (a) Surface roughness, and (b) waviness as a function of VED for 316L-Cu compositions.	75
Fig. 32. Structure of the proposed multivariate Gaussian process algorithm.....	78
Fig. 33. Cross validation plot based on density data set for the proposed multivariate Gaussian process algorithm.....	80
Fig. 34. Cross validation plot based on average surface roughness data set for the proposed multivariate Gaussian process algorithm.....	80
Fig. 35. Predicted process parameter maps for mfCu= 0.25.....	82
Fig. 36. Predicted process parameter maps for mfCu= 0.50.....	83
Fig. 37. Predicted process parameter maps for mfCu= 0.75.....	84
Fig. 38. Means of predicted values for density and surface roughness per hatch spacing.	85
Fig. 39. Tukey HSD results for comparison of means of (a) density and (b) surface roughness.	85
Fig. 40. Predicted VED values for 316L-Cu multi-material based on the best (a) density, and (b) surface roughness values. mfCu values are presented in percentages.	89

Nomenclature

S_a	Areal surface roughness
S_{wa}	Areal surface waviness
L	Characteristic melt pool length
CTE	Coefficient of thermal expansion
J	Compliance
cov	Covariance
D	Design space
Π_1	Dimensionless energy input 1
Π_2	Dimensionless energy input 2
ε	Elongation
Ω	Geometry/topology
h	Hatch spacing
d	Laser beam diameter
τ	Laser dwell time
P	Laser power
v	Laser scan speed
t	Layer thickness
R_a	Linear surface roughness
T_l	Liquidus temperature
Ma	Marangoni number
m_f	Mass fraction
S_v	Maximum valley depth of areal surface
f_i	Mean zero Gaussian process
ε_i	Measurement noise
ρ_{rel}	Relative density
T_s	Solidus temperature
C_p	Specific heat
γ	Surface tension
$d\gamma/dT$	Temperature coefficient for surface tension
k_l	Thermal conductivity of liquid
k_s	Thermal conductivity of solid
α	Thermal diffusivity
UTS	Ultimate tensile strength
σ_ε^2	Variance
μ	Viscosity
E_d (VED)	Volumetric energy density
YS	Yield strength
E	Young's (elastic) modulus

Abstract

Additive manufacturing (AM) has brought about a new age of design and manufacturing where traditional constraints are eased or in some areas completely lifted. The integration of topology optimization (TO) and AM has the potential to revolutionize modern design and manufacturing. However, few instances of manufactured optimized designs are documented, and even fewer examples of experimentally tested designs are available. The lack of validation combined with the influence of AM process on material properties leaves a gap in our understanding of process-microstructure-property relationships that is essential for developing holistic design optimization frameworks. In the first chapter of this thesis, a functional design was topologically optimized and fabricated using both directed energy deposition (DED) and selective laser melting (SLM), also known as powder bed fusion (PBF), methods. This is the first direct comparison of these AM methods in the context of TO. Mechanical properties of SS316L and the optimized components in as-fabricated and heat-treated conditions were investigated under uniaxial displacement-controlled tensile loading and compared to finite element modeling (FEM) predictions. Optimized samples provided regions of both compressive and tensile loading in the test specimen. Experimental results showed the FEM predictions to be conservative. Microstructural analysis revealed that this difference is due to refined microstructures formed during the additive manufacturing process that strengthen the material in regions with high stress levels. Moreover, SLM samples showed higher yield strength compared to DED samples due to a more refined grain size and denser dislocation structures. TO results are sensitive to the AM method, post-processing conditions, and differences in mechanical properties. Thus, a TO for AM framework can be best optimized with the incorporation of microstructure features to account for localized microstructural variations in fabricated components.

One of the main challenges facing SLM process is finding suitable process parameters to achieve maximum density (pore-free) parts. In chapter two, two newly discovered dimensionless

numbers are presented that correlate process parameters to a part's density allowing for an initial estimation of suitable process parameters without the need for extensive modeling or experimentation. The prediction is achieved by utilizing the Buckingham- Π theorem and the implementation of Pawlowski's matrix transformation method. The universality of the new dimensionless numbers is verified by applying them to selective laser melting data for eight different metals and alloy systems, obtained both experimentally and gathered from the literature. The dimensionless numbers allow for identification of process parameters that will result in a maximum density regime in the as-built part. Finally, a universal scaling law is introduced that can aid in quantitative prediction of process parameters that result in the highest as-built density.

Multi-material additive manufacturing using PBF has the potential to revolutionize the manufacturing landscape by producing parts with improved thermophysical properties and enhanced functionality. However, the complex nature of the process requires a case-by-case approach to multi-material characterization. The aim of chapter three is to provide firsthand knowledge of 316L stainless steel (316L) and Hastelloy X (HX) multi-material processing via PBF. Specifically, microstructure of the interface is studied using SEM and EDS analysis. Surface metrology is performed to characterize the resulting surface roughness at the interface followed by tensile and flexural testing of multi-material samples to characterize the mechanical properties of the interfaces. Finally, a post-fracture study is carried out to further assess the bonding integrity between 316L and HX with different order of printing. Results showed that using the proper process parameters for each individual material led to formation of a compositional gradient at the interface that stretched for 240 μm (10-12 layers) with no evidence of cracking or porosity. The interface exhibited higher surface roughness compared to 316L or HX as measured by S_a and S_v parameters. During tensile testing, samples failed in the 316L region away from the interface, with similar yield strength, ultimate strength, and ductility as compared to 316L samples. Finally, it was concluded that the "naturally" formed interface created a compositional gradient

which was defect free due to similar values of coefficient of thermal expansion, energy density, dimensionless number Γ_2 , and different Marangoni numbers of the materials.

The aim of chapter four is to propose a methodology for rapidly predicting suitable process parameters for additive manufacturing of multi-material parts with a compositional gradient by using machine learning and 316L-Cu bi-metal system. Specifically, an algorithm based on a multivariate Gaussian process is developed to predict part density and surface roughness for a given set of laser power, velocity, and hatch spacing values. The training data for the algorithm is collected using a high-throughput experimentation method that allows for rapid measurement of part density, and surface roughness. After the model is validated using leave-one-out cross validation method, process parameter maps are generated for 316L-Cu parts manufactured using selective laser melting with premixed powder at mass fractions of 0.25, 0.50, and 0.75. A set of suitable process parameters are predicted using the process maps. It is shown that process parameters are a nonlinear function of gradient composition and neither process parameters of 316L or Cu are suitable for the graded region of a 316L-Cu multi-material part. Generated process maps provide a firsthand knowledge of process-property relationships for regions of compositional grading in 316L-Cu parts.

Chapter 1: Topology Optimization for Additive Manufacturing

1.1. Introduction

Additive manufacturing (AM) can allow fabrication of designs that were previously impossible using conventional methods. AM technology has evolved as the manufacturing sector's adoption rate has grown by 80% since 2016 [1]. Benson et al. [2] investigated the improvement rate of AM technology based on the number of approved patents and determined that it is on an exponential growth rate, particularly with respect to manufacturing time and cost [3]. The increasing popularity of AM has also revitalized topology optimization (TO) [4]. TO is a mathematical technique in which material from a model of a structural component is selectively altered or removed to reduce weight while maintaining mechanical integrity or satisfying a geometrical constraint. Most geometrically complex designs generated by TO can only be manufactured through AM methods. As a result, TO is receiving growing attention among design engineers who are seeking to leverage the advantages of AM. Some of the recent attempts in design for AM (DfAM) include overhang-free designs which reduce or eliminate the need for support structures [5,6], diversified TO methods for porous metal structures [7], design with AM-induced anisotropy considerations [8,9], and microstructure control with TO [4]. However, resulting models are seldom manufactured and tested; see [10–12] for exceptions. This lack of experimental validation leaves a gap in our understanding of AM process-structure-properties-performance (PSPP) relationship and how it influences design optimization paradigms. More importantly, this knowledge gap prevents us from achieving a holistic design paradigm that couples design optimization with materials and process capabilities of AM [13].

This chapter aims to bridge the gap between design optimization and AM communities by realizing the light-weighting capabilities of TO through experimental validation of optimal designs. For the first time, this work directly compares the mechanical performance of topology optimized functional parts, manufactured via selective laser melting (SLM), and directed energy deposition

(DED). We discuss the microstructure differences and similarities of both AM methods and their contribution to mechanical performance of TO parts. Furthermore, we provide insight into how novel AM microstructures influence the mechanical properties that are essential in TO and how this understanding should inform the decision-making in DfAM. Finally, a quantitative connection between AM method, microstructure, and mechanical properties is established to explain the discrepancies between the finite element modeling (FEM) and the experimental results.

SLM and DED each provide advantages over conventional processes. SLM is used for the freedom in design offered due to its high precision and capability to create support structures for overhanging surfaces [14]. DED offers limited geometrical design freedom, since it cannot create overhanging features and the minimum feature size is up to ten times larger than that in SLM [14]. However, powder deposition in DED allows for instantaneous or gradual modification of the deposited composition, resulting in the ability to manufacture compositionally graded structures or high-throughput testing of new alloys in different designs [15–18]. Functional grading has the potential to allow for an additional layer of complexity in design optimization. For example, Mirzendehtel and Suresh [19] showed that multi-material TO can yield stiffer designs for a given volume fraction of material compared to single-material TO. Therefore, the ability to manufacture load-bearing, functional parts with DED allows us to take advantage of the unique mechanical, metallurgical and functionally graded properties of DED.

Variability in AM machines and the dependence of mechanical properties on microstructure mean that mechanical performance of a part can largely vary depending on the type of AM unit as well as what set of parameters or post-processing methods are used [20–24]. The mechanical response, particularly the yield strength and stiffness, has been shown to vary as a function of build orientation, heat-treatment method, and process parameters [25–32]. For example, the documented mechanical properties of AM SS316L, shown in **Table 1**, differ from those of conventionally manufactured SS316L and vary significantly between different AM

methods. As a result, it is possible to compute different optimal topologies for the same design due to variations in the Young's modulus and yield strength.

Examples of optimal designs are shown in **Table 2**. These designs are obtained using mechanical properties reported in **Table 1**. For the design obtained from ASTM properties, the target volume fraction is not achieved due to significantly lower yield strength. For designs obtained from SLM and DED properties, the final topology depends on which mechanical properties are selected by the user. These designs signify the need for mechanical properties characterization prior to TO. Moreover, the variance in mechanical properties and its influence on TO indicates that design optimization solutions should encompass these variations to ensure accuracy and robustness. Until such design solutions are available, developing widely applicable predictions of mechanical performance for optimized designs fabricated via AM will remain a challenge [13].

The rapid, directional solidification and complex thermal cycling in both SLM and DED processes modify microstructural development compared to conventionally-fabricated materials [32]. In SLM parts, the synthesis leads to a dense, cellular dislocation microstructure and the formation of small precipitates as well as typically high yield strength and ductility [33]. Less is known about the microstructure in DED parts, although they have also been shown to exhibit a high yield strength [32]. Although the influence of characteristics such as grain size, texture, and dislocation structure development on mechanical response have been phenomenologically investigated extensively in conventional materials, the physical relationships between the AM microstructures and the improved mechanical response are less defined. Several efforts have been made to predict the resulting mechanical properties of AM material by microstructure characterization [29,33–39]. Currently, these approaches are time consuming, cost prohibitive and impractical in an industrial setting. However, they highlight an untapped potential of AM to locally control material properties at voxel level whereby AM process, microstructure, and mechanical properties can be incorporated in design optimization [13]. Such optimization

schemes can produce designs that meet requirements with margins, but first, the gap in our understanding of PSPP relationship must be filled.

1.2. Materials and methods

1.2.1. Mechanical properties characterization

SS316L is a commonly used material in AM and thus it was chosen for this study. The stainless-steel alloy does not experience any solid-state phase transformations during deformation, and the alloy is nominally single-phase after manufacture. To characterize the mechanical properties of the AM materials, tensile test specimens (**Fig. 1**) were mechanically ground on both sides with sandpaper to 600 grit, then additionally on one side with diamond, alumina, and finally 0.05 μm colloidal silica grits to minimize the effects of surface roughness and possible mechanical damage from electrical discharge machining (EDM) used to remove the samples from the build plate. Room temperature tensile tests were performed using an MTS[®] Sintech load frame with a 50 kN load cell and 2.20 mV/V sensitivity. Tests were carried out at constant crosshead separation rate of 1 mm/min (strain rate of 0.04 s^{-1}) and data were collected at 10 Hz. Strain measurements were conducted by digital image correlation (DIC) system provided by Correlated Solutions[®]. Zero-normalized squared difference algorithm was used to calculate the displacement of speckles on each sample. Collected data were then translated to longitudinal principal strains. Results were used to calculate the mechanical properties of SS316L in the elastic regime, including the Young's modulus and yield strength (calculated based on the 0.2% offset method).

In mechanical testing of topology-optimized parts, the same procedure was followed as for the tensile test specimens; however, to accurately capture part displacement and avoid adding the fixture strain to the data set, an MTS extensometer with gauge length of 25 mm and travel range of (+12.5, -2.5) mm was used. Force-displacement data was collected for further analysis.

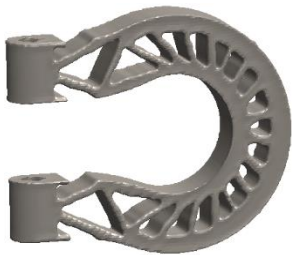
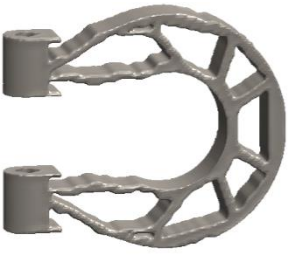

Table 1. Comparison of SS316L tensile properties as reported by machine manufacturer with those given in the literature.

Properties	Values*			
	SLM		DED	
Manufacturing technique	Machine Manufacturer	Literature [22]	Machine Manufacturer	Literature [40,41]
Young's modulus (E) GPa	typ. 185	188 ± 29	-	193
Ultimate tensile strength (UTS) MPa	640 ± 50	592 ± 69	799	685 ± 66
Yield strength (Y) MPa	530 ± 60	453 ± 54	500	465 ± 78
Elongation (ϵ) %	40 ± 15	30 ± 6	50	35 ± 3

Annealed bar ASTM SS316L: UTS = 485 MPa, Y = 170 MPa, ϵ = 40% [42].

* Values are obtained from as-built tensile samples, pulled perpendicular to build direction.

Table 2. Examples of possible optimal topologies obtained from select mechanical properties reported in Table 1. Volume fraction is defined as the volume of the original design divided by the volume of the final design.

	Mechanical Properties used in TO as reported by		
	ASTM	SLM	DED
Desired % vol. fraction	50	50	50
Topology			
% vol. fraction achieved	32	50	50

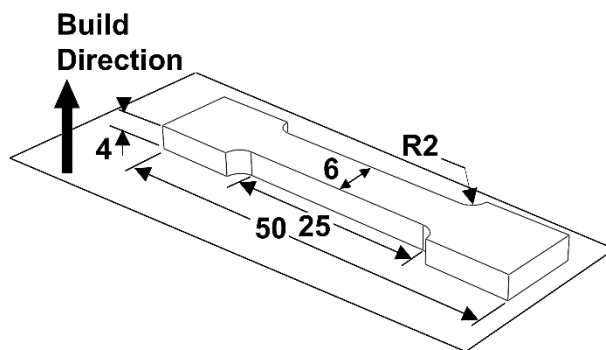


Fig. 1. Tensile test specimen geometry and build direction. Dimensions in (mm).

1.2.2. Topology optimization

Three criteria were considered for selecting the suitable case study. First, the part geometry should allow the use of a simple test fixture without the need for assembly. Using intricate testing fixtures alters the load distribution path throughout the part and can cause premature failure in assembled joints [11]. Moreover, complex fixtures can hinder our ability to accurately measure force and displacement during testing. Second, the component should be a load-bearing part that represents real world scenarios where both compressive and tensile stresses are present. Third, the final topology should be manufacturable via both SLM and DED methods. The clevis part that meets the above-mentioned criteria was chosen for optimization.

Fig. 2 shows the model's critical dimensions and the selected boundary conditions (BCs).

The TO algorithm used in this work is Pareto, developed at UW-Madison [43], now commercially available (www.sciartsoft.com). Pareto is a topological-sensitivity based method that can generate numerous Pareto-optimal topologies up to a desired volume fraction. Readers are referred to [43] and [44] for more details on the Pareto method. The TO problem is posed as below and solved with 100,000 hexahedral elements by taking advantage of symmetry.

$$\begin{aligned} & \text{Min } J \\ & \Omega \subset D \\ & \text{subject to} \\ & \text{Stress, volume and manufacturing constraints} \end{aligned} \tag{1}$$

Where:

J : Compliance

Ω : Geometry/topology to be computed

D : Design space

In order to impose performance (stress) constraints, appropriate yield strengths for SLM and DED fabricated parts were determined using standard tensile testing described in section 2.1. In addition, an arbitrary volume fraction constraint of 50% was chosen for this case study. Here, the

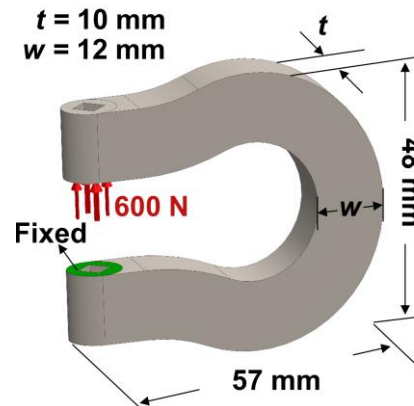


Fig. 2. Clevis model with critical dimensions and BCs.

volume fraction is defined as the original volume of the design divided by the final volume of the design after TO.

The optimal topologies computed without explicit manufacturing constraints are not manufacturable via DED method due to the presence of hollow features. Although these designs can be fabricated via SLM, the hollow features prohibit the removal of required support structures, making them impractical for SLM as well (**Fig. 3. (a)**). Thus, it was critical to impose manufacturing constraints on the problem. A through-cut constraint was applied to ensure that the cross-section remained constant along the build direction, eliminating the need for support structures (**Fig. 3. (b)**).

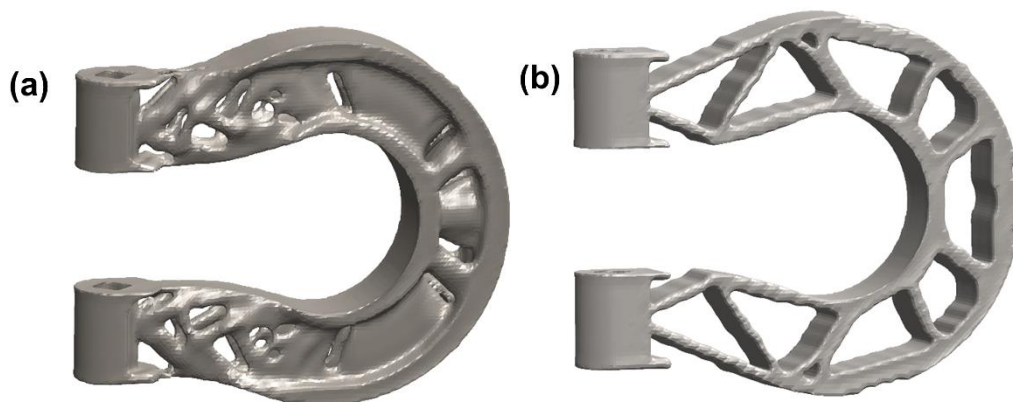


Fig. 3. An example of a topology optimized clevis part without imposing manufacturing constraints (a) and with through-cut constraint (b). The TO problem is posed as described in section 2.2.

1.2.3. Additive manufacturing

An EOS® M290 system was used to manufacture six clevis samples using recommended process parameters in **Table 3** [45]. It is known that SLM parts exhibit anisotropic behavior based on build direction [25], i.e. ultimate tensile strength is lower along the build direction. Therefore, samples were fabricated in the orientation perpendicular to the direction of applied force shown in **Fig. 2**. to mitigate the effects of anisotropy in tensile testing. Furthermore, six tensile specimens were cut using wire electrical discharge machining (EDM), from rectangular bars manufactured using the same build direction relative to the loading direction and process parameter set as clevises. **Fig. 1** shows the dimensions of these specimens. In both cases, three samples were used as-built as a control while the other three were subjected to a heat treatment of 1000°C for 1 hour, followed by a water quench. Heat treatment process was in accordance with the procedure mentioned in [46]. Heat treatment is commonly used for AM parts to alleviate the effects of residual stresses on the mechanical properties [27,47].

The material used in manufacturing was SS316L powder, particle size less than 60 µm, provided by EOS®. Nominal chemical composition of the powder (as supplied) and as-built samples are presented in **Table 4**. Actual chemical compositions were measured with combustion infrared detection (C and Si), inert gas fusion (O and N), and direct current plasma emission spectroscopy (all others).

An Optomec® laser engineered net shaping (LENS®) MR7 system was used to manufacture clevis and tensile testing specimens using the same approach used for the SLM parts. The main process parameters used during manufacturing are presented in **Table 5**. Process-induced anisotropy has also been reported for parts manufactured via DED, although it is typically not as pronounced as with SLM [28]. The same build orientations used in the SLM approach were used for DED parts. Parts were cut off the build plates using wire EDM and rounded ends and holes were later machined. Tensile testing specimens were fabricated using the same process parameters in **Table 5**, and the same dimensions as depicted in **Fig. 1**, except

for a thickness of 2.5 mm. The same sample size and heat-treatment process was repeated for the DED experiment. SS316L powder used for DED process was provided by Carpenter® with particle size range of 45 to 150 μm . The nominal composition of the DED powder and actual chemical composition of the samples are provided in **Table 4**.

Table 3. EOS M290 main process parameters for SS316L.

Parameter	Values
Contour	2 layers
Laser power	
Infill	195 W
Contour	110 W
Laser speed	
Infill	1083 mm/sec
Contour	800 mm/sec
Hatch rotation angle	67°
Hatch distance	0.09 mm
Layer thickness	0.02 mm
Platform temperature	80° C

Table 4. Chemical composition of SS316L. Nominal values are reported by powder manufacturer while actual values are measured from as-built samples. All values are in wt%.

Element	SLM			DED		
	Nominal		Actual	Nominal		Actual
	Min	Max		Min	Max	
Fe	Balance		Balance	Balance		Balance
Cr	17.000	19.000	18.390	16.000	18.000	18.060
Ni	13.000	15.000	13.940	10.000	14.000	13.790
Mo	2.250	3.000	2.860	2.000	3.000	2.860
C	-	0.030	0.004	-	0.030	0.005
Mn	-	2.000	1.470	-	2.000	1.580
Cu	-	0.500	0.002	-	-	0.010
P	-	0.025	0.017	-	0.045	0.008
S	-	0.010	0.004	-	0.030	0.004
Si	-	0.750	0.300	-	1.000	0.320
N	-	0.100	0.065	-	-	0.072
O	-	-	0.043	-	-	0.037
H	-	-	0.00008	-	-	-
Co	-	-	0.0036	-	-	0.0054
Al	-	-	0.002	-	-	0.001

Table 5. Optomec® LENS MR7 main process parameters for SS316L.

Parameter	Values
Contour	2 layers
Contour offset	0.38 mm
Laser power	
Infill	275 W
Contour	275 W
Feed rate	508 mm/min
Hatch rotation angle	67°
Hatch distance	0.38 mm
Layer thickness	0.254 mm

1.2.4. Microstructural characterization

The influences of processing method and heat treatments on the microstructure were analyzed across multiple length scales to include microstructural characteristics known to influence the mechanical properties. Grain size and grain morphology were analyzed using scanning electron microscopy (SEM) in a Zeiss LEO-1 microscope operated at 3-20 kV accelerating voltage, as well as with electron backscatter diffraction (EBSD) in a FEI Helios G4 PFIB CXe with an Elstar™ SEM column equipped with an Hikari EBSD camera and accelerating voltage of 230 kV. EBSD maps were approximately 1-2 mm x 2-3 mm with step sizes of 1-3 μm. Some specimens were sectioned in the undeformed state and mechanically ground, then 3 mm disks were punched out. Disks were polished to electron transparency with a Stuers Tenupol twin-jet electropolisher in A2 electrolyte at -20°C and 17 V for approximately 15 minutes for TEM analysis. TEM samples were analyzed in a Tecnai TF-30 S/TEM operated at 300 kV for diffraction contrast imaging and diffraction analysis of dislocation structures and crystallography.

1.3. Results and analysis

1.3.1. Tensile test results

The data in **Table 6** presents the means and standard deviations of mechanical properties of SS316 tensile test specimens for SLM and DED. Stress-strain curves are presented in . Overall,

the effect of heat treatment on both SLM and DED samples were similar with the yield strength as the most affected property. After heat treatment, the yield strength dropped by 49% and 50% for SLM and DED samples, respectively. Standard deviations indicated that DED demonstrated better consistency in mechanical properties in the elastic regime compared to SLM. However, the same cannot be said for elongation at failure, where DED showed larger deviations compared to SLM. It should be noted that further experiments are needed to confirm this initial observation and provide a scientific basis for this conclusion. Nonetheless, all samples indicated at least 40% elongation to failure in tension, and this ductility was more than adequate for the scope of this work.

Table 6. Mechanical properties of SS316L, obtained from tensile test specimens.

		Young's modulus (E) GPa	Ultimate tensile strength (UTS) MPa	Yield strength (YS) MPa	Elongation at UTS (%)	Elongation at YS (%)
SLM	as-built	190 ± 45	671 ± 33	560 ± 25	24 ± 0.8	0.52 ± 0.07
	heat-treated	147 ± 32	616 ± 13	377 ± 19	33 ± 0.4	0.48 ± 0.06
DED	as-built	198 ± 16	645 ± 10	489 ± 8	52 ± 2	0.47 ± 0.02
	heat-treated	188 ± 12	600 ± 8	325 ± 4	60 ± 6	0.39 ± 0.02

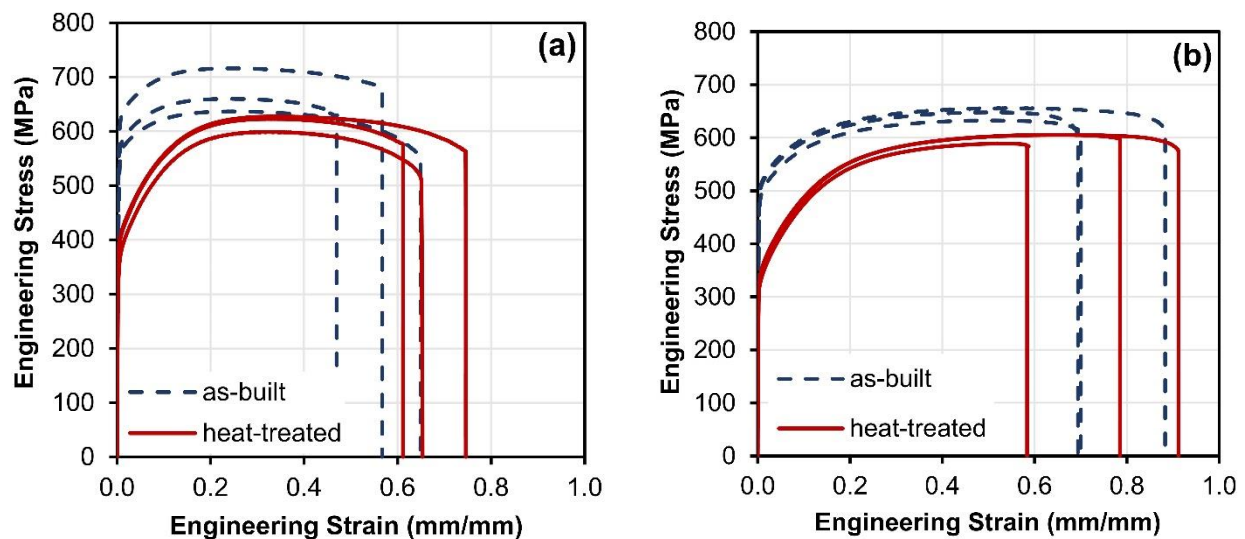
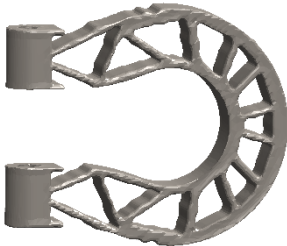
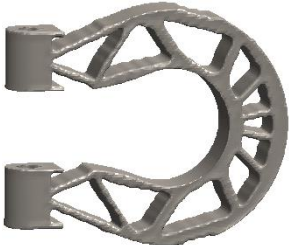


Fig. 4. Engineering stress-strain curves obtained from tensile test specimens. (a) SLM and (b) DED.

1.3.2. Clevis TO and mechanical test results

After mechanical properties characterization, TO was carried out using the reported Young's modulus and yield strength of heat-treated samples in **Table 6**. The final optimal designs for SLM and DED clevises obtained are shown in **Table 7**. It should be noted that the measured difference in Young's modulus and yield strength between SLM and DED resulted in a subtle difference in final designs. A comparison between (a) and (b) revealed that clevis design for SLM has 12 reinforcing struts distributed along its arch while clevis design for DED has 10. However, for a meaningful comparison, the design shown in (b) was chosen for fabrication using both AM methods.

Table 7. Optimal topologies obtained from mechanical properties of heat-treated SS316L reported in Table 6.

	Mechanical Properties used in TO	
	SLM	DED
Desired % vol. fraction	50	50
Topology		
% vol. fraction achieved	50	50

Artifacts from the TO process were manifested as mesh irregularities, as shown in the inset in (b). These irregularities can cause stress concentration and premature failure during testing. As of today, fully automated feature-based geometry reconstruction for TO remains an unsolved problem [48–51]. Therefore, to alleviate the concerns regarding the mesh irregularities, the design shown in (b) was used as a reference to create the design shown in (c) using conventional CAD operations. It should be noted that this method of geometry reconstruction is

limited to standard CAD operations and the resulting features may not fully capture the complexity of the original design. However, in this case study, the through-cut constraint simplified the design to a level that conventional CAD operations were able to closely capture the features of the original design. More importantly, as shown in (d), the maximum von Mises stress occurred on the outer surface of the clevis' arch, and this surface was unaffected during TO. As a result, this critical feature was perfectly preserved throughout the geometry reconstruction process. The final optimal designs were then manufactured using AM, as shown in **Fig. 6**.

Although the optimized design achieved the target of 50% volume fraction, and the same model was used to manufacture the samples, the volume of manufactured clevises differed from the 50%. The average volume fraction of samples fabricated via SLM was measured at 45.6% while the average volume fraction of samples fabricated via DED was measured at 61.8%. The difference in the volume of the SLM samples is negligible and can be attributed to machining during support structure removal. The difference in the volume of the DED samples can be explained by considering the larger laser beam diameter of LENS system ($\approx 600 \mu\text{m}$) compared to EOS system ($\approx 80 \mu\text{m}$) which can result in oversized features in designs with intricate geometries.

The resulting force-displacement graphs from clevis tensile tests are shown in **Fig. 7**. Tests were terminated once the extensometer reached its maximum displacement. Heat-treated SLM samples yielded at approximately 1500 N, compared to 1950 N for as-built samples. Similarly, heat-treated DED samples yielded at approximately 1710 N, compared to 2240 N for as-built samples. Results agree with the standard tensile test results wherein the heat-treatment process had a similar effect on the yield strength of both DED and SLM samples.

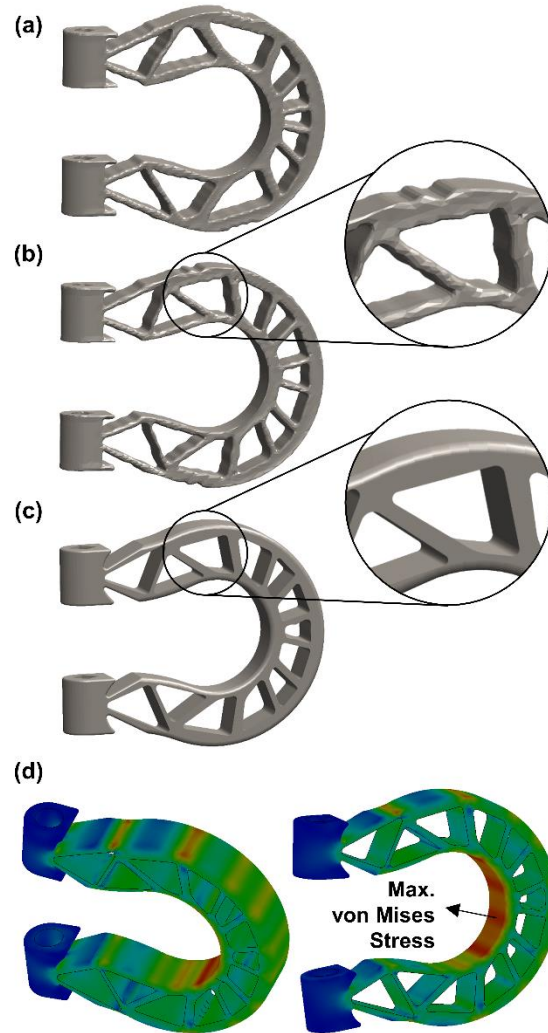


Fig. 5. TO designs based on the mechanical properties of (a) heat-treated DED, and (b) heat-treated SLM. (c) Design 'b' is reconstructed for AM using conventional CAD operations. (d) Different views of von Mises stress distribution. Area where maximum von Mises stress occurred is indicated by the arrow.

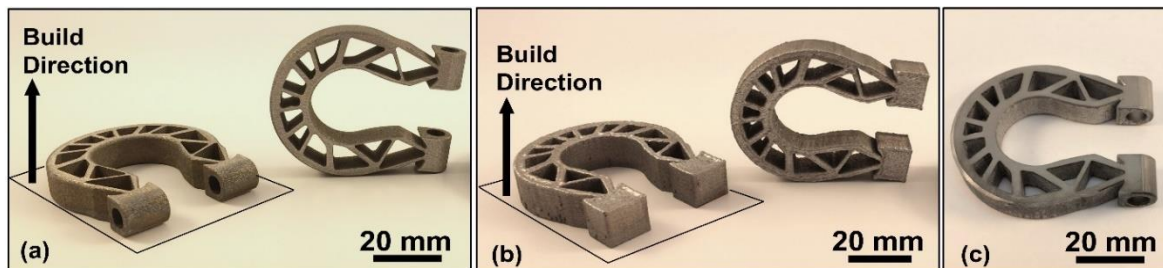


Fig. 6. Clevises manufactured via (a) SLM, and (b) DED. Round ends and holes for DED clevises were later machined to net shape (c).

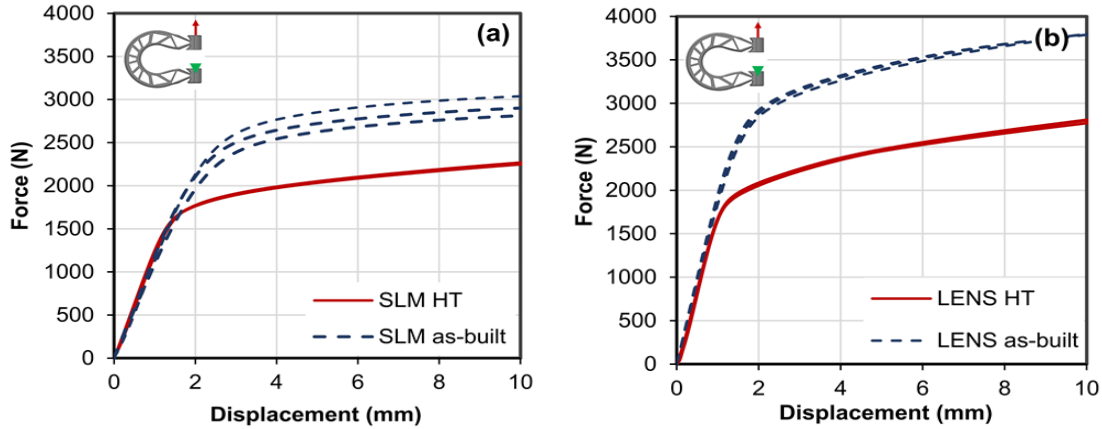


Fig. 7. Clevis tensile test results for (a) SLM and (b) DED fabricated samples, with and without heat treatment.

Finally, the data in **Table 8** shows averaged results from the tensile tests against FEM using the properties presented in **Table 6**. Initially, results for DED samples showed larger deviance from FEM calculated values compared to SLM. The larger deviation can be attributed to the extra volume of the DED samples which increased the experimental yield load. To compensate for the increase in volume, the experimental yield loads of the DED samples were scaled. Since the thickness of the DED samples (denoted by t in **Fig. 2**) was kept the same after machining, the increase in volume was solely due to a uniform increase in samples' width (denoted by w in **Fig. 2**). According to basic bending stress calculations, 11.8% increase in volume results in 25% decrease in bending stress, and consequently, the yield load. After applying this adjustment, yield loads for both SLM and DED samples showed similar deviations from FEM predictions. Scaled yield loads for DED samples are presented in **Table 8**.

Table 8. Comparison of tensile test results with FEM for topology optimized clevises.

		FEM yield load (N)	Experimental yield load (N)	Scaled experimental yield load ^(a) (N)	Error ^(b) (%)
SLM	as-built	1825	1950	-	6.4
	heat-treated	1227	1500	-	18.2
DED	as-built	1590	2240	1680	5.7
	heat-treated	1058	1710	1282	21.2

(a) experimental yield load for DED is scaled to reflect the increased volume of DED clevises during manufacturing.

(b) for DED, the error is based on the difference between the FEM and scaled yield loads.

1.3.3. Microstructural characterization

The microstructures were found to be spatially heterogeneous in 3D and exhibited directionality dependence on the laser scan path and AM method. These dependencies are illustrated in the simplified schematic shown in **Fig. 8** for reference. The following sections will frequently refer to this schematic and discuss the microstructural features depicted therein.

1.3.3.1. Grain structure in SLM

The initial grain structures in the tensile test specimens indicated a strong dependence on laser scan direction, AM process, and thermal history, as shown in the EBSD maps in **Fig. 9**. These maps are colorized according to the crystallographic orientation aligned with the loading direction (vertical in **Fig. 9**) and the stereographic triangle color key (inset), with grain boundaries indicated in black. The as-built SLM structure consisted of grains that were columnar in the build direction, as indicated in **Fig. 8**, but exhibited a “mosaic” structure when viewed in the plane perpendicular to the build direction, as shown in **Fig. 9**. (a). The mosaic structure, previously reported in steels manufactured using an EOS M270 SLM unit [52], consists of large grains (diameter greater than approximately 50 μm) aligned in rows along the laser scanning direction surrounded by small grains. Although large grains appeared equiaxed in the scanning plane shown in **Fig. 9**. (a), many of the small grains were elongated along the laser scanning direction, yielding an average grain aspect ratio of 2.07 in the scanning plane. Grains were 20 μm in diameter on average in the scanning plane. Grains were elongated in the build direction, typically reaching 100-400 μm long, and extending across multiple layers. The grains appeared organized along the laser scanning direction, or 45° to the loading direction in the uniaxial tension specimens, as indicated parallel to the dashed lines in **Fig. 9**. (a). There was no strong preferred orientation along the loading direction in the SLM as-built material. A $\langle 011 \rangle$ texture developed in the build direction (out-of-plane in **Fig. 9**) in the SLM materials but this was not expected to strongly influence the tensile response, since there was no texture in the loading direction.

Heat treatment of the SLM material led to little change in grain size, with an apparent slight refinement from 20 μm to approximately 16 μm in diameter on average, **Fig. 9.** (b). No significant change in the aspect ratio was observed in the scanning plane, although the mosaic structure became less apparent, and the laser scanning path was no longer as evident in the final microstructure. The SLM microstructures have been shown to persist in annealing treatments up to 1200 °C for up to an hour [53–57], indicating high stability against heat treatment. The underlying mechanisms responsible for this enhanced stability in AM SS316L dislocation structures are still not fully understood, and are outside the scope of the current work. The slight refinement in grain size was likely a result of recovery processes and the inhibition of grain growth. Recovery and reorganization of deformation/dislocation microstructures, which are present in the as-built SLM material, can lead to an increased appearance of grain boundaries, as discussed in section 3.3.5. Despite the changes to the grain morphology, the original texture in the build direction was maintained after heat treatment in SLM material.

1.3.3.2. Grain structure in DED

The DED as-built structures consisted of elongated grains aligned approximately 20-30° to the laser scan direction, which was oriented approximately 45° to the loading axis, as indicated in **Fig. 9.** (c) by dashed lines. Within each laser scanning pass, grains were elongated within +/- 10° of the scan path, as indicated between the dashed lines in **Fig. 9.** (c). The scan strategy of scanning 45° with respect to the sample loading axis, alternating 180° between passes and rotating 90° between layers, led to grains being elongated in various directions with respect to the loading axis dependent on the local laser scan direction. This directionality was also observed in the build direction, where grains were oriented either +45° or -45° with respect to the build direction depending on the layer, as shown schematically in **Fig. 8.** (b). Grains exhibited an average aspect ratio of 3.09 in the laser scanning plane. Grains were elongated at various angles with respect to the build direction as well, in directions that changed depending on the layer, as

indicated in **Fig. 8**. Although many grains were elongated, many regions between layers or between scan passes exhibited primarily equiaxed grains, as shown in the lower right corner of **Fig. 9**. (c). The average grain diameter for all grains, weighted by their respective areas, was approximately 80 μm . No significant texture was observed in the DED material. Heat treatment induced a significant increase in grain size, such that the average was approximately 140 μm , and a reduction in grain elongation, with an average aspect ratio of 2.14.

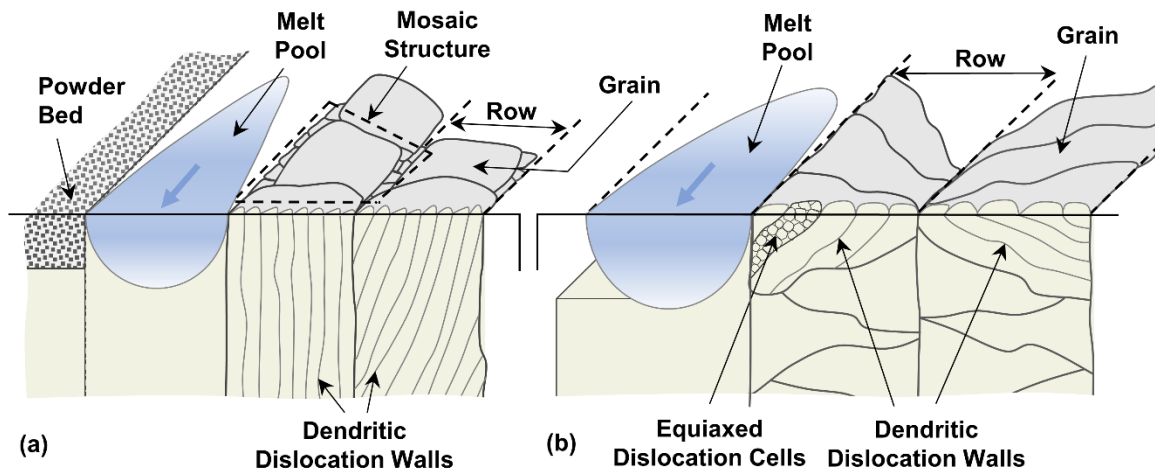


Fig. 8. Schematic illustrating laser scanning path, grain structure, and microstructural characteristics for (a) SLM and (b) DED fabricated parts.

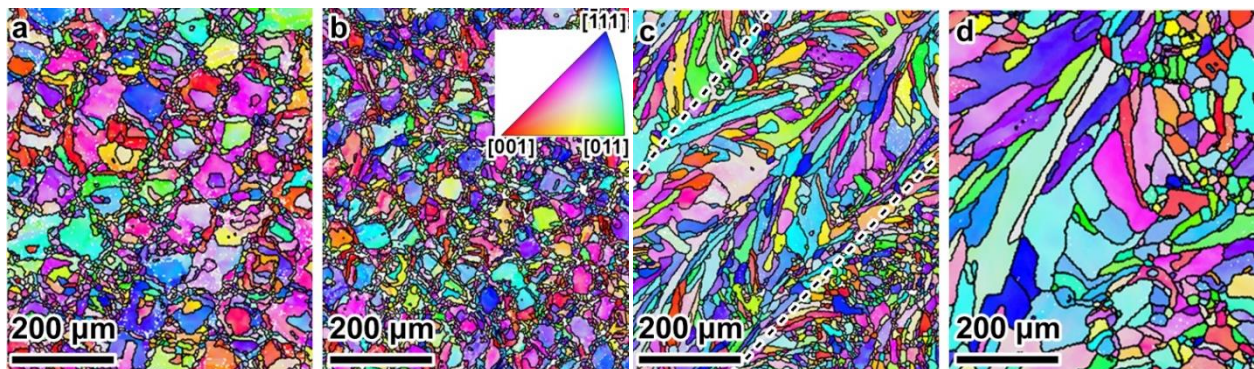


Fig. 9. EBSD orientation maps in the tensile loading direction of initial structures in (a) SLM as-built, (b) SLM heat-treated, (c) DED as-built, and (d) DED heat-treated tensile specimens, with grain boundaries indicated in black. Tensile axis vertical, build direction is out-of-plane. Dashed lines in (c) outline the edges of one laser scan path.

1.3.3.3. Comparison of response to heat treatment in SLM vs DED

The increase in grain size observed in DED material compared to the reduction observed in SLM material for the same heat treatment is considered to be a reflection of the microstructural

differences. Differences between the initial dislocation structures likely influenced recovery and the formation of new grain boundaries, as discussed in section 3.3.5 and 3.3.6. However, differences in the microstructural evolution due to heat treatment are only relevant with respect to their influence on the mechanical response of heat-treated material; the mechanism responsible for any difference in the thermal stability of dislocation structures is outside the scope of this work. Together, these effects could have contributed to the difference in microstructural evolution between SLM and DED material subject to the same heat treatment.

1.3.3.4. Effects of scan strategy on grain structure

The influence of scan strategy on microstructure had an additional effect on the clevises due to the variations in relatively thinner and thicker sections of the design. EBSD maps of grain structures at the base of a strut in the clevis part are shown for SLM and DED as-built materials in **Fig. 10.** (a) and (b), respectively. These maps are colorized according to the vertical loading direction using the same color key shown in **Fig. 9**, with grain boundaries traced in black. The region from which maps were taken on the clevis parts are shown in the inset; large black regions near the top left and lower right corners of **Fig. 10.** (a) and (b) indicate empty space around the strut.

In the SLM material, grains were still organized along the laser-scanning path, as indicated parallel to the dashed lines in **Fig. 10.** (a). However, the orientation of these rows changed in some regions, for example where the upper dashed line curves in **Fig. 10.** (a). Another example is the orientation of rows in the thin strut compared to the bulk of the material, see dashed line in the lower section of **Fig. 10.** (a). These changes in grain elongation direction were observed most frequently near the edges of the specimen, where different printing parameters and different scan strategies were used for contours; see **Table 3**. The dependence of the grain structure and elongation on laser scan path indicates an additional factor that may be considered when choosing scanning strategies for parts with complex geometries.

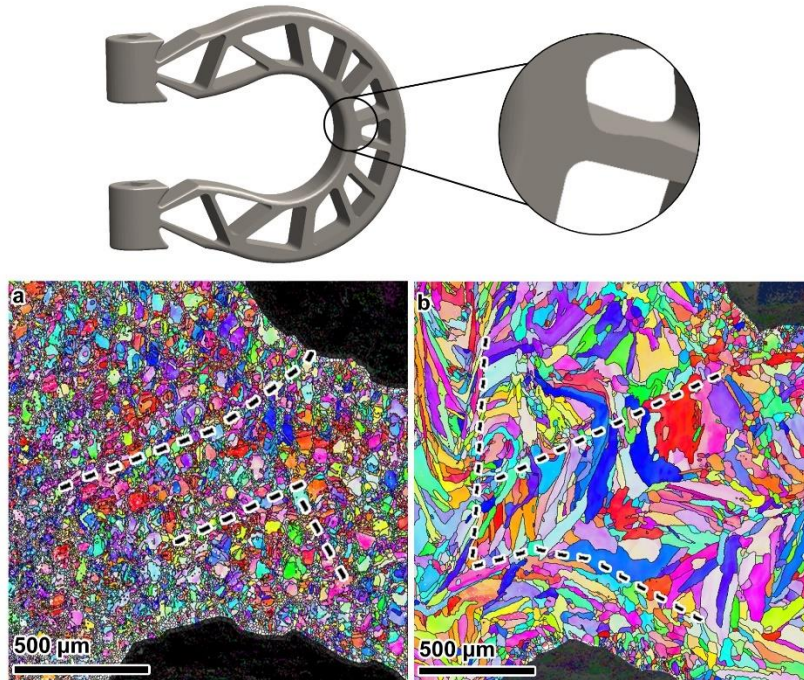


Fig. 10. EBSD orientation maps of initial structures in (a) SLM as-built and (b) DED as-built clevis parts. Colorized according to orientations in the loading direction (vertical).

This influence of scan path was even more apparent in the DED parts, where grain alignment with the laser scanning path changed within approximately 400 μm of edge of the part. Within 50-100 μm of the edges, grains became smaller, as highlighted by the dashed lines in **Fig. 10. (b)**. The scanning strategy also influenced the grain elongation direction in different sections of the part's interior. For example, the grains at the leftmost side of **Fig. 10. (b)** are finer than those in the middle of the strut, as indicated by dashed lines.

1.3.3.5. Dislocation microstructures in SLM

At the sub-grain level, microstructures influenced by AM processes were observed. In the SLM as-built material, a dislocation structure consisting of elongated, dendritic dislocation cells was observed, as shown in the bright-field STEM image in **Fig. 11. (a)** and **Fig. 8**. Cell walls are indicated by dashed lines. The walls consisted of dense, tangled dislocations and tended to lie on $\{001\}$ -type planes when viewed edge-on, as is typical for SLM 316L [33], with average spacing approximately 450 nm. The crystallographic directionality of the dislocation cells indicates that solidification was dendritic. Si, Mn, and Cr oxide precipitates were observed, typically ranging in

size from 5-20 nm in diameter, examples of which are indicated by arrows in **Fig. 11. (a)**, as reported in [58]. In the as-built material, oxides were found to be primarily Si- and Mn-rich. The precipitates were observed both in cell interiors and within dislocation walls, although the density of precipitates was difficult to determine particularly inside walls due to the local density of dislocations. Precipitates frequently appeared to pin dislocations.

Heat treatment of SLM material qualitatively reduced the dislocation density and caused a reorganization of dislocation structures. Dislocation walls were observed, but with spacings typically ranging from 400-600 nm, slightly larger than that observed for the as-built material, as shown in **Fig. 11. (b)**. Higher-magnification imaging revealed that walls were qualitatively less dense than in the SLM as-built material, such that individual dislocations were more clearly defined and less tangled. Dislocation structures in the heat-treated specimens frequently corresponded to in-plane rotations of up to 10° between adjacent regions, which exceeds the threshold misorientation of 3° used to identify grain boundaries in EBSD mapping.

An example of these dislocation boundaries is shown in **Fig. 11. (b)**, where elongated boundaries can be seen aligned diagonally across the image. The diffraction pattern of this region, shown in the inset in **Fig. 11. (b)**, indicates that over approximately ten of these low-angle boundaries, in-plane rotations were measured up to approximately 5.7° . Many of the low-angle boundaries appeared to result from incomplete recovery and reorganization of the preexisting dislocation structures, such that they remained aligned and elongated. This is consistent with observations of the stability of the SLM microstructure against heat treatments below approximately 1100°C [53–57].

Dislocation structures within grains, in other words those that were unambiguously not part of a grain boundary, in SLM heat-treated material frequently consisted of aligned dislocations with fewer tangles than observed in SLM as-built dislocation cells. Example are indicated parallel to the dashed lines in **Fig. 11. (b)**. Oxide precipitates were larger in the heat-treated material, with sizes on the order of 40-60 nm, indicated by the arrows in **Fig. 11. (b)**. Precipitates in the heat-

treated material were found via EDS analysis to be Cr- and Mn-rich oxides without Si- enrichment. Frequently, precipitates were surrounded by tangled, pinned dislocations in the heat-treated SLM structure.

1.3.3.6. Dislocation microstructures in DED

As-built DED microstructures were qualitatively less refined than as-built SLM structures, as shown in **Fig. 12**. The as-built DED microstructure consisted of large, dendritic dislocation cells 1-2.5 μm in diameter, delineated by the large dashed line in **Fig. 12**. (a), superimposed on a background of smaller, equiaxed dislocation cells with an average diameter approximately 370 nm in diameter. The large cell structures consisted of dislocations with Cr segregation and Fe depletion in the walls, indicating that they are dendritic, while the small cell structures exhibited uniform composition. Although the large, dendritic dislocation walls appeared equiaxed in electron-transparent foils, FIB machining and SEM analysis indicated that these walls were elongated similar to the SLM dislocation cells, but in the foil normal direction (which coincides with the build direction). The small dislocation cells with uniform composition were not found to be elongated. Both types of DED dislocation structures appeared qualitatively less dense than the cell walls in the SLM as-built structure, for example compare the wall indicated by the dashed line in **Fig. 12**. (a) with that in **Fig. 11**. (a). Additionally, a significant density of dislocation walls and tangles aligned on multiple $\{111\}$ -type planes were observed, for example parallel to the small, straight dashed line in **Fig. 11**. (a). These structures were typically spaced 1-2 μm apart and extended across multiple large and small cells. Precipitates were observed throughout the microstructure, although more frequently in the walls of the large cells with segregation and ranged in size from 70-200 nm; examples are arrowed in **Fig. 12**. (a). Precipitates in as-built DED material were Si- and Mn-rich oxides.

Heat treatment of the DED material induced a decrease in dislocation density, as shown in the image taken across a grain boundary in **Fig. 12**. (b). Dislocations accumulated in the

proximity of grain boundaries, such that structures were sparser in grain interiors than those shown in **Fig. 12. (b)**. Dislocation pileups were found on $\{111\}$ -type planes near grain boundaries, as indicated by the dashed lines in **Fig. 12. (b)**. These pileups consisted primarily of aligned dislocations with few dislocation tangles, although dislocations became more tangled with 1-2 μm of grain boundaries. Occasionally, extended dislocations, dislocation dipoles, or nodes were observed. Precipitates were less frequently observed, and those that remained ranged from 150-250 nm in size, for example as indicated by the arrow in **Fig. 12. (b)**. These precipitates were found both in the matrix and along grain boundaries and were primarily Mn- and Cr-rich oxides without Si enrichment.

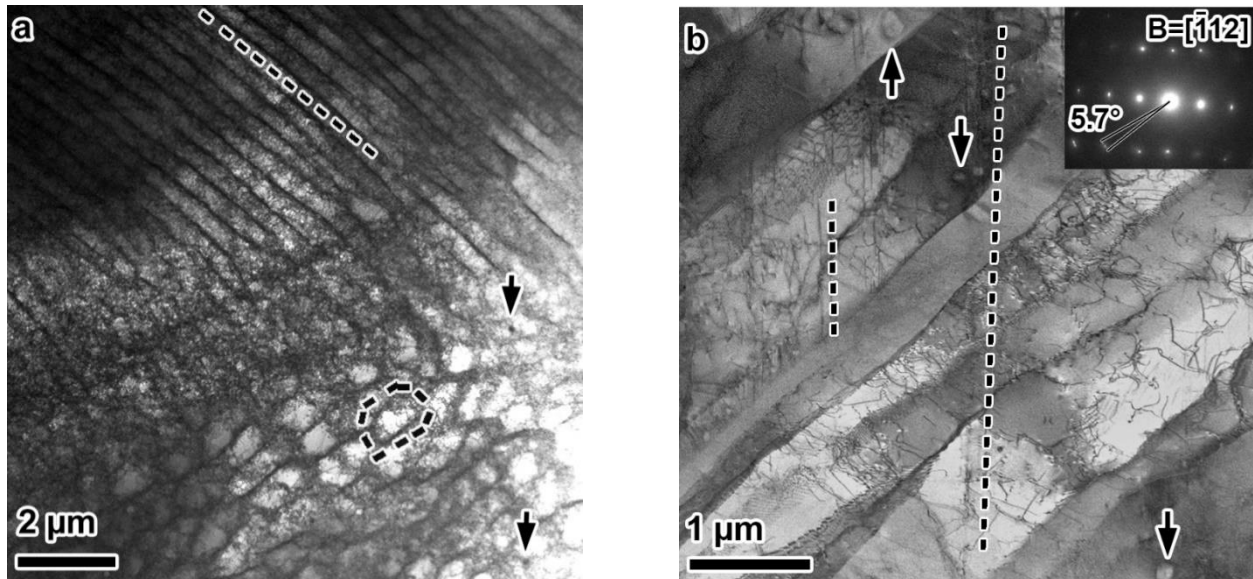


Fig. 11. Bright-field diffraction-contrast STEM images of dislocation structures in (a) SLM as-built material, with dendritic dislocation cells (dashed lines) and precipitates (arrows), and (b) SLM heat-treated material, with grain boundaries extending diagonally from bottom left to upper right, aligned dislocations extending across grain boundaries indicated by the dashed lines, and precipitates (arrows). Diffraction pattern inset in (b) with spreading of diffraction peaks indicative of 5.7° misorientations between grains.

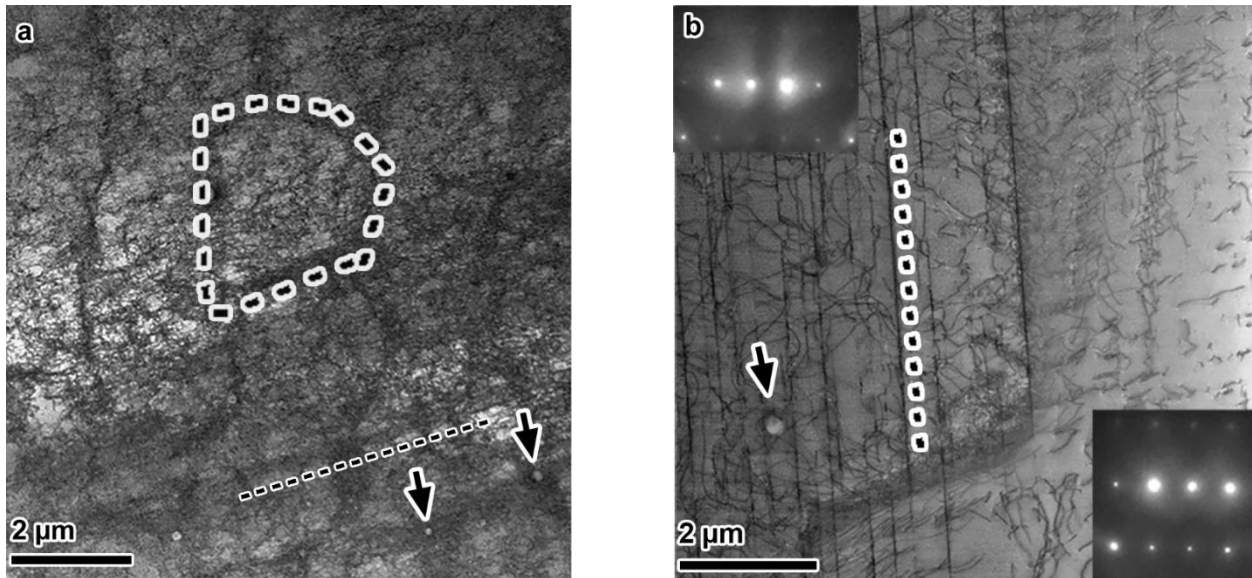


Fig. 12. Bright-field diffraction-contrast STEM images of dislocation structures in (a) DED as-built material, with extended dislocation walls (parallel to the small dashed line), precipitates (arrows), and dendritic dislocation walls (outlined by the large dashed line) surrounding small, equiaxed dislocation cells. (b) DED heat-treated material with precipitates (arrow), a grain boundary running from top to bottom, and dislocation pileups on $\{111\}$ planes (parallel to the dashed line) near grain boundaries. Inset diffraction patterns in (b) shown for the two grains across the grain boundary.

1.4. Discussion

The influence of AM processing on microstructures has important implications for mechanical properties, and consequently TO design. These implications are summarized in **Fig. 13** in the form of an influence diagram that can help guide the decision-making process in DfAM. The diagram depicts the TO for the AM process as a closed loop, where changes in one step can affect the entire process. The results from this study indicate that until a holistic optimization framework is developed which encompasses all the steps included in **Fig. 13**, TO for AM must be examined and experimentally validated on a case-by-case basis due to the variance in microstructure and overall mechanical response. The difficulties in estimating the mechanical response of TO parts from FEM and material response based on AM microstructures, and the subsequent need for experimental validation, are discussed in the following sections.

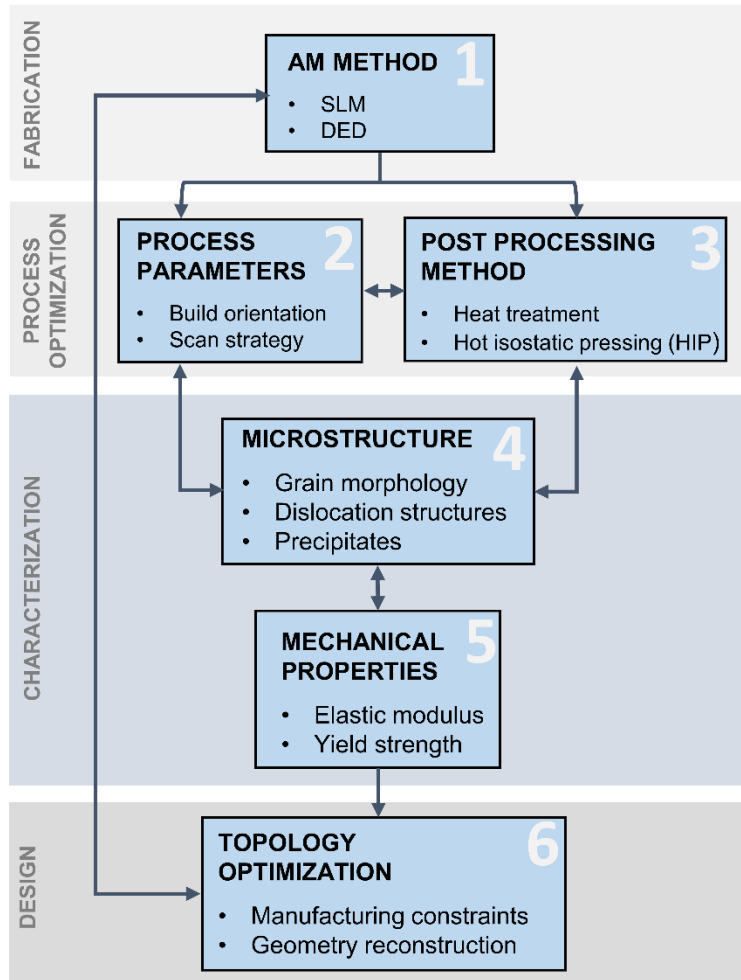


Fig. 13. DfAM decision-making diagram. Arrows indicate the influence of each step on the other. More items can be added to each step as our understanding of the process matures.

1.4.1. Prediction of yield strength based on analysis of AM microstructures

The yield strength in a material is an essential input to TO and FEM, but it can be greatly influenced by several microstructural features developed during AM, particularly the dislocation structures, grain structure, and precipitate distribution. A summary of the microstructural features in the different materials is shown in **Table 9**. Dislocation densities are reported from the literature as measured by x-ray diffraction techniques for similar materials and heat treatments [35,59,60]. In the SLM heat-treated case, the dislocation density is estimated to be similar to that measured by Bronkhorst et al. for heat-treated DED 316L [35]. Experimental line intercept methods in this study were consistent with these published values.

Table 9. Summary of averaged microstructural features that may influence the yield strength.

		Equiaxed dislocation cell size (nm)	Dendritic dislocation wall spacing (nm)	Dislocation density (m^{-2})	Precipitate diameter (nm)	Grain size (μm)
SLM	as-built	-	450	3.8×10^{14} [60]	15	20
	heat-treated	-	-	9×10^{13} [35]	40	16
DED	as-built	370	1750	2.5×10^{14} [35,59,60]	120	80
	heat-treated	-	-	9×10^{13} [35]	200	140

The potential influences of these different parameters on the yield strength are as follows. First, increasing dislocation content increases material yield strength, and the dislocation content in the AM materials was shown to be high. The dense, elongated dislocation cells that occur in as-built SLM material, as shown in **Fig. 11**, are well-documented [33,61–63], and the high yield strengths observed in SLM SS316L compared to conventional annealed material are frequently attributed to the presence of these structures. DED dislocation structures have received less attention in the literature but appear to be influential on mechanical response given the differences in mechanical response after heat treatment. Although the dislocation density remains high, structures are less organized than in SLM material, with less organization of dislocations into cell walls. Additionally, in the DED material, although segregation was observed, it did not overlap with all dislocation cells, leading to a dual cell structure with two types of walls, one dendritic with segregation and one equiaxed with uniform composition. Although outside the scope of this study, the additional solid-solution strengthening effect afforded by segregation to some of these walls would be expected to contribute to strengthening as well.

Precipitates can also strengthen the material due to particle hardening effects by presenting barriers to dislocation motion [64]. Grain morphology can also impact the mechanical response, such that decreasing grain size increases the yield strength according to the well-known Hall-Petch effect [64,65].

In order to assess the relative contributions of different microstructural features on the yield strength, calculations of the strengthening afforded by each of these microstructural features were performed. The effect of dislocation strengthening based on dislocation densities reported for similar materials in the literature [35,59,60] was estimated using a forest-hardening model, the effect of grain size was calculated via the Hall-Petch effect, and precipitate strengthening due to Orowan hardening was calculated, as summarized in **Table 10**. For SLM as-built material, the Hall-Petch effect was calculated treating dislocation cells as the grain size, since the walls have been shown to be effective barriers to dislocation motion and such treatment has yielded good approximations for others in the literature [33]. For other materials, the combined effects of grain size and forest dislocation hardening were used. Particle hardening was estimated for SLM material, using estimates of the volume fraction of precipitates as reported in [58].

In all cases, this approach led to overestimation of the actual hardening. The differences between actual results and microstructurally-based estimates indicate a need to validate the mechanical properties of the AM material separately before use in TO models. Not only do the microstructures vary substantially between conventional materials and AM materials, but also the same heat treatment can have different effects, as observed with grain refinement in SLM material and grain growth in DED material subject to the same heat treatment.

Dislocation density appeared to have the most significant effect on the strengthening, whether due to treating the cells as contributing to a Hall-Petch type effect or due to forest hardening. Particle hardening was not observed to be significant in the SLM material, due to the relatively low overall volume fraction of precipitates.

Grain boundary strengthening similarly appeared to contribute little to the total strengthening. For SLM as-built material, the thin, columnar grains and dislocation cells contribute to an enhanced yield strength compared to many conventional recrystallized materials with grain sizes on the order of 50-100 μm [33], or for example the DED materials. Upon heat treatment, the particular rearrangement of the dislocation structures only slightly influenced the grain structure

in the SLM materials, although the heat-treated structures were significantly different than the preexisting dislocation cells. This suggests that the grain structure was not as influential a factor in determining the overall yield strength as the dislocation structures.

Table 10. Calculated contributions to yield strength based on the Hall-Petch relationship and forest dislocation strengthening, and the difference between calculated estimates and measured values. All values are in (MPa).

		Hall-Petch contribution (cell size)	Hall-Petch contribution (grain size)	Dislocation density contribution	Particle hardening	Yield based on calculated contributions	Actual yield	Δ
SLM	as-built	429	-	-	65	677	560	117
	heat-treated	-	63	180 [35]	36	462	377	85
DED	as-built	-	28	300 [35,59,60]	-	511	489	22
	heat-treated	-	21	180 [35]	-	384	325	60

In DED as-built material, the grain size alone fell within the range of about 20-120 μm in diameter and is not expected to have significantly influenced yield compared to conventional material. The heat treatment of DED material caused grain growth, but the yield strength after heat treatment was approximately 67% of the initial yield strength. This is an equivalent yield drop to that observed in SLM specimens with heat treatment, even though the grain sizes barely changed in the SLM specimens, indicating that grain size had less influence on yield in the AM materials than other factors like dislocation structure. Further, this indicates that the dislocation structures that developed near grain boundaries in the heat-treated DED material were more influential on the mechanical response than the grain boundaries themselves.

1.4.2. Additional influence of TO design on strengthening

The orientation of grain boundaries may influence elastic response in different orientations. Since grains in the DED as-built material are elongated in the laser scanning direction, the distance between grain boundaries is smaller perpendicular to the scan path than parallel to it, leading to a different effective grain size in different directions. If the material is loaded perpendicular to the laser scan path, the shorter effective grain size could lead to a greater

Hall-Petch strengthening effect. This behavior was confirmed recently by Mukherjee [34], who showed that the yield strength in DED material loaded in different orientations increased with decreasing effective grain size based on the orientation of the scanning direction with respect to the loading direction. This result has important implications for TO. Since the laser scan path can affect the effective grain size in different regions, as was observed in **Fig. 10**, the yield strength may change locally within the part depending on the local stress state. Since TO parts typically exhibit complex, spatially-varying stress states due to their complex geometries, the interactions between processing parameters, microstructure, and properties is even more complex and difficult to predict, necessitating experimental testing prior to TO, as indicated in **Fig. 13**. This effect may also contribute to differences between FEM predictions and actual part performance.

1.4.3. Influence of AM on accuracy of FEM predictions

According to **Table 8**, clevis samples performed better than FEM predictions in all cases. This positive deviance can be explained by considering the effects of process parameters on microstructure and the fact that FEM does not account for material anisotropy due to local microstructural variations. As indicated in **Fig. 10**, grain orientation and size are different on sample's periphery due to different scan strategies used to print the outline (shell) of the clevis, particularly in DED samples. It so happens that the maximum von Mises stress occurs on the sample's periphery where this microstructure refinement takes place. As a result, samples exhibited higher yield loads than FEM predictions. This result was more pronounced for DED samples according to **Fig. 10**. Moreover, the DED clevises had 11.8% more volume than the model used in FEM, which if not accounted for, can result in larger deviations from FEM predictions. For more accurate results, machine manufacturers can implement scaling factors in their part-preparation software to correct for this manufacturing induced enlargement.

1.4.4. Potential benefits of AM for TO

Understanding the PSPP relationship within the context of TO has the potential to become a powerful tool. Exploiting this relationship may allow manufacturers to: create parts that are better suited for tension or compression in different areas of the part (by manipulating texture or grain boundary orientation); change the mechanical response by changing laser scan strategy to have different grain orientations, elongations, or sizes; and to adjust the microstructure to have maximum strength in some areas and maximum ductility in others, all dependent on what is most beneficial within the complex stress fields that correspond to these complex geometries. In other words, there is opportunity to exceed the current practices of design optimization; to simultaneously optimize process parameters, microstructure features, and final topology to achieve properties that are locally tailored to specific applications at the voxel level [13,66].

1.5. Conclusions

In this chapter, topology optimized designs were manufactured using SLM and DED methods and their mechanical performance were experimentally compared with FEM. Effects of AM method and heat treatment on microstructure were studied and correlated to mechanical properties that are essential in TO. Discrepancies between the FEM and experimental results were investigated and correlated to process-induced microstructure features in clevis samples. The following conclusions can be drawn from the experimental results:

- Topology optimized clevis samples outperformed the FEM predictions for both SLM and DED methods by 6% and 29% in as-built state, and 18% and 38% in heat-treated state, respectively. This difference is attributed to changes in the microstructure of the boundary (shell) layers that is caused by different scan strategies and process parameters used to fabricate those layers. In SLM, grain size and alignment between scan path direction were changed whereas in DED, grain size and grain elongation direction were changed. These microstructure alterations strengthened regions of the sample where the maximum von

Mises stress occurred, resulting in higher yield loads. Typical FEM does not consider such manufacturing-induced anisotropies, suggesting that more mesoscale-based models would help refine the conservative estimates.

- SLM samples showed higher yield strength compared to DED, and they both showed higher yield strength compared to conventionally-made SS316L. The most influential microstructural feature in increasing the yield strength proved to be the dislocation structures in both AM methods, in as-built and heat-treated states, whereas grain size contribution was not as significant. The difference in yield strength between SLM and DED was partially responsible for the slight difference in the optimal topologies computed for both AM methods.

In summary, the topology optimization approach was shown to be sensitive to AM method, process parameters and heat treatment. The main differences are attributed to the varied microstructural evolutions, illustrating a need for a comprehensive understanding of the PSPP relationships to provide holistic design optimization schemes.

Chapter 2: Dimensional Analysis of SLM Process

2.1. Introduction

SLM is the most widely adopted and studied metal additive manufacturing AM technique [67,68]. SLM owes its popularity to its ability to produce complex geometrical features, desirable mechanical properties, and versatility in processing a large variety of metals. Most SLM systems have numerous process parameters that are often material dependent. Consequently, the first challenge in fabrication is finding a suitable set of process parameters for pore-free processing of metals since it is shown that porosity adversely affects mechanical properties and can cause premature failure [32,69,70]. Experimental [71–73] and machine learning solutions [74–76], albeit proven effective on a case by case basis, are not universal or scalable.

Another approach to try to consolidate the number of influential process parameters and provide universal scaling laws is dimensional analysis. There are four advantages in applying this technique to the SLM process [77]. First, it reduces the number of parameters that are required to draw a meaningful relationship between input and output. Second, a reliable scale-up of the suitable process conditions from research to full-scale plants can be achieved. Third, for processes with a high number of variables, full factorial design of experiments is cumbersome, time intensive, and potentially expensive. Finally, although major process parameters can be the same for any SLM system, local differences in implementation, design and components can result in different outputs for the same parameter values and materials. A dimensional analysis circumvents this issue because it allows for comparison of results across different SLM systems and metals.

Researchers have introduced several well-known and newly derived dimensionless numbers for AM [78–83]. However, these numbers require melt pool characteristics data that is not readily available to most AM users and is generally not available a priori. In this chapter, a dimensional analysis was applied to the SLM process which led to the discovery of two

dimensionless numbers that correlate the major process parameters to a part's density (porosity) for a wide range of metals and alloy systems. The predictive and descriptive power of the dimensionless numbers is validated experimentally by manufacturing bulk specimens from a variety of metals and alloys. The universality of the new dimensionless numbers was further verified by applying it to data from the literature produced by other researchers, where different SLM systems and different measurement methods were used.

2.2. Materials and methods

2.2.1. Dimensional analysis

The dimensional analysis carried out in this work is based on Buckingham- Π theorem [84]. The theory is implemented through Pawlowski's matrix transformation method to derive a complete set of dimensionless groups for the SLM process based on the chosen process variables [85]. Here, only the newly discovered dimensionless numbers are reported. Readers are referred to [78–80] for a more comprehensive list of other dimensionless numbers pertaining to the SLM process. The variables that appear in the newly discovered dimensionless numbers are listed in **Table 11**. The thermophysical properties of materials used by the authors and those which are later used in case studies are listed in **Table 12**. Thermal diffusivity (α) is included to highlight the wide range of materials that is covered in this study. Thermal diffusivity is more representative of the differences during a transient heat transfer process like SLM compared to thermal conductivity or specific heat. It is well known that thermophysical properties of materials are temperature dependent. Here, the thermophysical properties are chosen at room temperature. Effects of varying thermophysical properties on the results remain a topic for future work.

Table 11. Process variables appearing in the resulting dimensionless number.

Process Variable	Description	Unit	Dimension
P	laser power	(W)	ML^2T^{-3}
v	laser scan speed	(mm/s)	LT^{-1}
t	nominal layer thickness	(mm)	L
d	laser beam diameter	(mm)	L
h	hatch spacing	(mm)	L
C_p	specific heat capacity	(J/kgK)	$L^2T^{-2}\theta^{-1}$
k	thermal conductivity	(W/mmK)	$MLT^{-3}\theta^{-1}$

Table 12. Thermophysical properties of metals at room temperature.

	Specific Heat, C_p (J/kgK)	Thermal Conductivity, k (W/mK)	Thermal Diffusivity, α (mm ² /s)
316L stainless steel [86]	450	13.8	3.9
Al10SiMg [87]	915	111	45.4
Cu [86]	384	330	95.9
Hastelloy X [88]	439	10.4	2.9
IN718 [88]	435	12	3.4
Ta [86]	151	70	28.3
Ti6Al4V [89]	546	7.3	3.0
W [86]	136	90	34.3

2.2.2. Additive manufacturing

Samples of 316L stainless steel, Hastelloy X, Cu, and IN718 were manufactured on a commercial SLM machine (EOS M290) equipped with a 400 W fiber laser and constant laser beam diameter of 100 μm . Gas atomized, spherical powder with average particle diameter of $\leq 60 \mu\text{m}$ were used per manufacturer's recommended specification. A set of 27 hexagonal shaped samples were manufactured per material with circumscribed circle diameter of 8 mm and height of 4 mm. Four process parameters were chosen as variables in this study: laser power (P), laser speed (v), laser hatch spacing (h), and nominal layer thickness (t). Samples were made using infill parameters only, meaning that other scanning strategies that are typically used for part's top and bottom surfaces or contours were not applied to these samples. A stripe scanning strategy with 5 mm width was used at a rotation angle of 67 degrees. The build plate temperature was kept constant at 80°C.

2.2.3. Density measurement

Archimedes method was used to measure the density of the samples [90]. After samples were removed from the build plate and before density measurement, they were ground to eliminate any remaining support structure from the bottom surface. Residual support structures could easily entrap air bubbles during submergence into the fluid and potentially contribute to measurement errors. Samples were weighed while dry, and then weighed while suspended in Fluorinert™ FC-40 ($\rho = 1855 \text{ kg/m}^3$) to collect the data required to calculate the density.

2.3. Results

2.3.1. Dimensionless number

After implementing Pawlowski's method and investigating the resulting 14 dimensionless groups, the newly discovered dimensionless number can be defined as:

$$\Pi_1 = \frac{C_p P}{k v^2 h} \quad (2)$$

where, C_p is specific heat, P is laser power, k is thermal conductivity, v is laser scan speed, and h is hatch spacing.

To better understand the physical meaning of the discovered dimensionless number, two new parameters were introduced. First, the well-known volumetric energy density defined as:

$$E_{in} = \frac{P}{v h t} \text{ (J/mm}^3\text{)} \quad (3)$$

This term quantifies the input energy to the powder bed. The second parameter is the dwell time, τ , and it is defined as the ratio of laser beam diameter, d , to laser scan speed, v .

$$\tau = \frac{d}{v} \text{ (sec)} \quad (4)$$

Dwell time quantifies the amount of time it takes for the laser beam to traverse a distance equal to its diameter. Guided by Π_1 and considering eqns. (3) and (4), one can derive a new dimensionless number:

$$\Pi_2 = \frac{C_p}{k} E_{in} \tau \quad (5)$$

The Π_2 term provides more flexibility than Π_1 in translating volumetric energy density analyses between different SLM machines with different lasers because it accounts for laser beam diameter and nominal layer thickness. The term also clearly represents the dimensionless number as a product of a material's thermophysical properties, the processing input energy, and laser dwell time.

2.3.2. Predicting porosity modes

The correlation between the dimensionless number Π_1 and relative density of various metals is shown in **Fig. 14**. Here, relative density is defined as the ratio of the measured density to maximum achieved density, except for Cu where measured density is divided by the theoretical density of pure copper. There are several mechanisms that lead to porosity in SLM processes [32,91]. Most of the pores observed in SLM are due to lack of fusion that is caused by insufficient energy input [71] or keyhole phenomenon that is caused by excessive energy input [92]. Cross-sectional microscopy of 316L samples revealed that Π_1 can be used to provide a coarse-grained estimate of the porosity modes. As Π_1 increases to 61, the relative density approaches 99.5% indicating a decrease in lack of fusion porosity. The relative density maintains its value until Π_1 reaches 146 after which it starts to decrease again, indicating the beginning of the keyhole regime. As a result, when $61 < \Pi_1 < 146$ there is a window where process parameters resulting in relative density of $\geq 99.5\%$ can be defined, we designated this window the green zone. These values are determined based on the equation of the curve that is fitted to the entire data set. These equations are introduced in the following section.

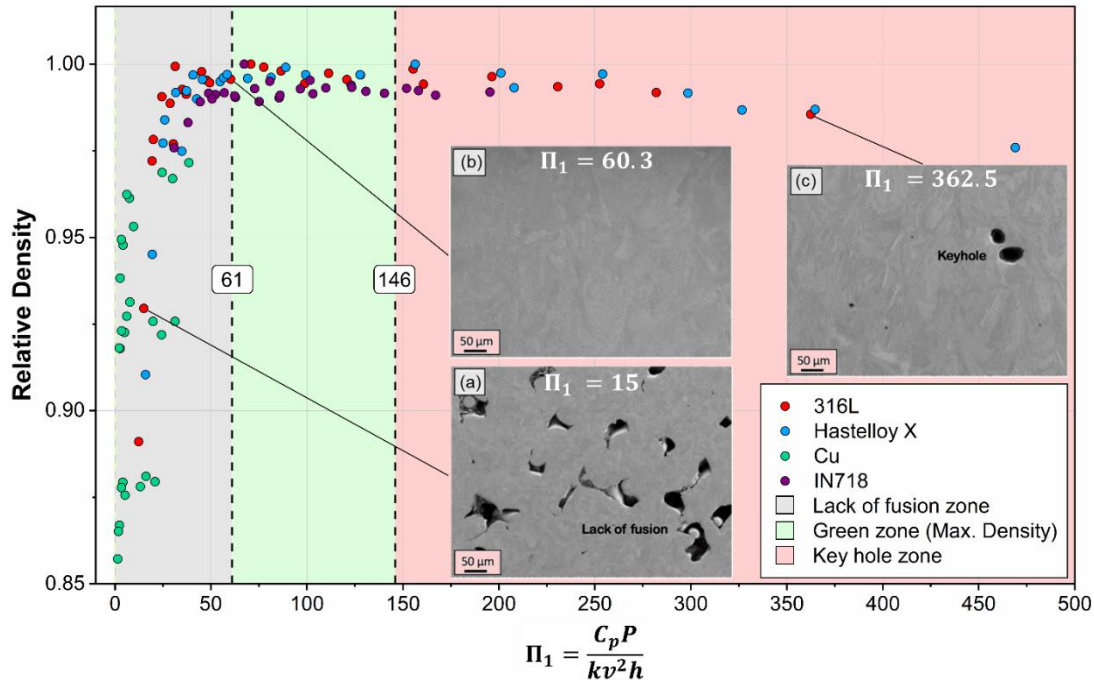


Fig. 14. Relative density as a function of dimensionless number Π_1 for select materials and estimation of porosity modes.

2.3.3. Universal scaling law

To verify the universality of the relationship, the dimensionless numbers are applied to data for SLM of various materials available in the literature (**Fig. 15**). Pal et al. [93] investigated the pore morphology of Ti6Al4V processed by SLM. According to the reported data, parameters that resulted in maximum density fall within the range predicted by this study. Read et al. [94] investigated the influence of process parameters on mechanical response of AlSi10Mg and most of the recorded data fell within the lack of fusion zone. It should be noted that multi-phase alloys such as Ti6Al4V, AlSi10Mg, and IN718 can have two-phase microstructures. The overall density of these alloys is a function of the volume fraction of these phases, which in turn depends on the kinetics of phase transformation and process cooling rates. Although this data shows excellent agreement with the curve in **Fig. 15**, more rigor is required to quantify the density of such alloy systems. Finally, data from tantalum [95], and tungsten [96] were used to further verify the predictive capability of the dimensionless numbers for refractory metals. As shown in **Fig. 15**, the

dimensionless energy input can successfully predict porosity modes and levels for these materials.

A two-part exponential function is introduced as a universal scaling law. The exponential nature of the law agrees with the energy coupling mechanisms discussed in [97]. For both dimensionless numbers, an adjusted R-square of 96% is achieved. Although the predictive capability of both dimensionless numbers are statistically the same, the additional process variables, laser beam diameter and layer thickness, that are embedded in the definition of Π_2 offer more flexibility in capturing and translating the behavior of different SLM systems compared to Π_1 . If laser beam diameter or layer thickness are constant, or values are unavailable, the following universal scaling law can be used for predictions:

$$\rho_{rel} = 0.9985 \exp\left(-2.391 \times 10^{-5} \times \frac{C_p P}{k v^2 h}\right) - 0.1504 \exp\left(-0.06688 \times \frac{C_p P}{k v^2 h}\right) \quad (6)$$

If layer thickness and laser beam diameter are variables or of importance to the users, the following scaling law can be used:

$$\rho_{rel} = 0.9984 \exp\left(-4.54 \times 10^{-6} \times \frac{C_p E_{in} t}{k}\right) - 0.1557 \exp\left(-0.01735 \times \frac{C_p E_{in} t}{k}\right) \quad (7)$$

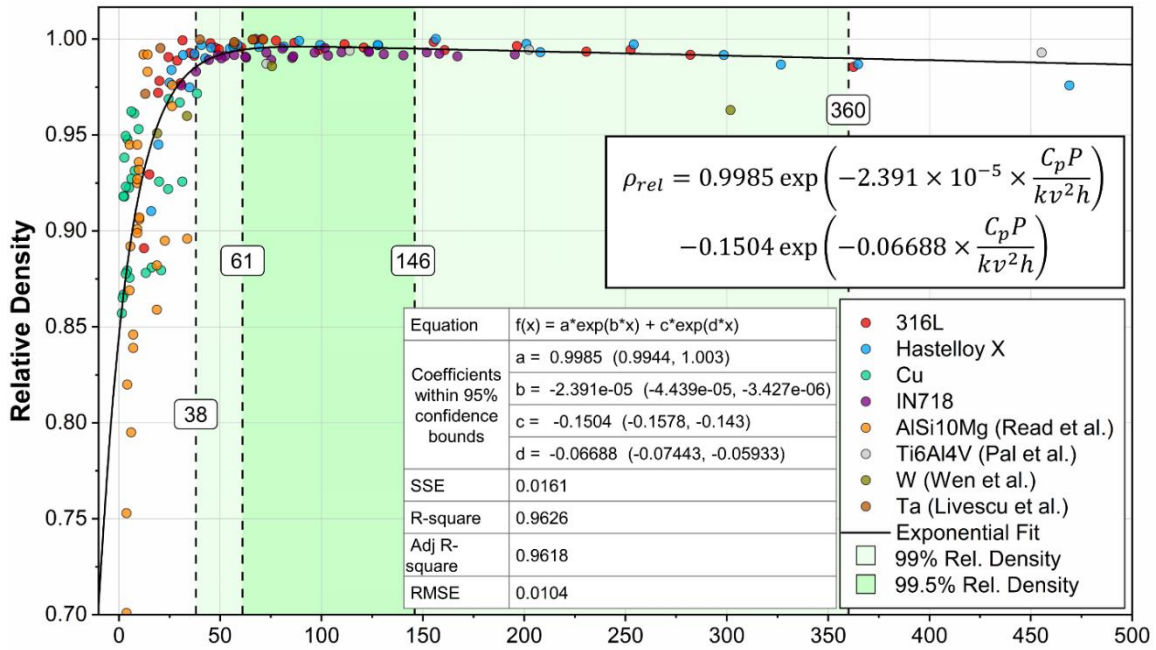
Considering the evidence provided in **Fig. 15**, for any metal and any SLM system, it appears that relative density can be expressed as a function of the following variables:

$$\rho_{rel} = f(P, v, h, t, d, C_p, k) \quad (8)$$

2.4. Conclusions

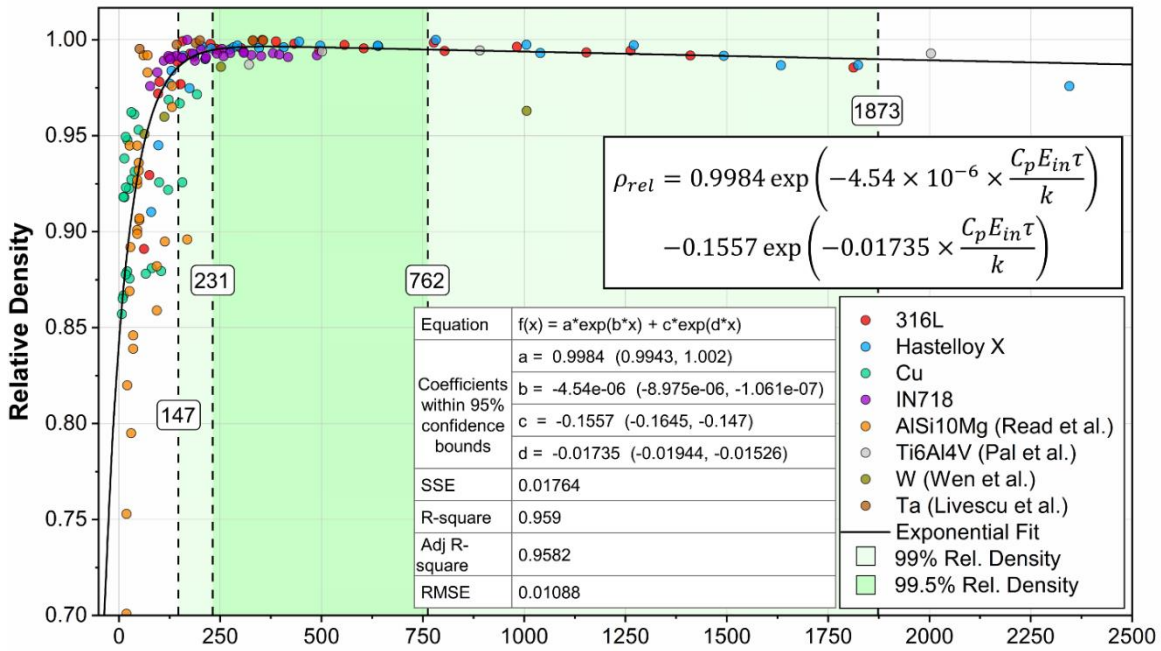
This chapter presents two dimensionless numbers for the SLM process that correlate process parameters to density (porosity). These dimensionless numbers provide a coarse-grained estimation of pore typology for a wide range of materials. The proposed dimensionless numbers scale well with different metals and alloy systems that are produced with various SLM systems. Finally, universal scaling laws are derived from the experimental data that yield the relative density of any material processed by SLM using values that are readily available to all

users. Although density was the focus of this communication, the ability to adapt the dimensionless analyses to other properties and features may be possible.



(a)

$$\Pi_1 = \frac{C_p P}{k v^2 h}$$



(b)

$$\Pi_2 = \frac{C_p E_{in} \tau}{k}$$

Fig. 15. Dimensionless numbers for predicting density in SLM. (a) Dimensionless number Π_1 . (b) Dimensionless number Π_2 .

Chapter 3: Characterization of Multi-material 316L-Hastelloy X

3.1. Introduction

Multi-material additive manufacturing (MMAM) holds the promise of multi functionality and tailored physical properties; hence, it has become an attractive subject of study within the AM community in the recent years [98,99]. Among the two most popular metal AM processes, DED and PBF, DED offers more flexibility for multi-material processing due to its deposition mechanism which allows for mixing of different materials at different ratios. Hence, the majority of MMAM research has been focused on DED process [100]. Newly developed deposition mechanisms for PBF, has captured attention for multi-material processing [101]. Within the PBF context, MMAM is defined as an AM process capable of creating complex geometries from multiple metals and alloys where the positioning of each material within the part is designed and controlled to serve a specific function or enhance a specific property [102]. Unlocking multi-material capability for PBF will have a transformative impact on the industry given that PBF offers superior surface roughness, dimensional accuracy, and geometrical complexity compared to DED processes.

Parts with enhanced functionality and improved thermo-physical properties will find many applications within the aerospace, automotive, nuclear, and petrochemical industries. For example, high electrical and thermal conductivity can be achieved in tandem with high strength with steel-copper alloy systems [103–106], Ti6Al4V wear resistance can be improved by manufacturing a protective TiB₂ layer [107], light-weight design and electrical conductivity can be achieved by AlSi10Mg-C18400 system [108], or high strength at high temperature together with good damage tolerance can be obtained from maraging steel-H13 bimetal system [109,110]. After steel-copper alloy systems, the most studied bimetal system is steel-nickel alloys. Steel-nickel alloy multi-material parts can be used in high temperature and corrosive environments such as light water reactors, power and chemical plants, and gas turbines [111,112].

IN718 is the most studied nickel alloy in the context of multi-material PBF. Mei et. al. [113] investigated SS316L-IN718 parts manufactured using PBF. They reported good metallurgical bonding supported by microscopy and tensile testing results. The interface was determined to be ~100 μm with some cracks and porosity near the interface. In another study, Chen et. al. [114] used *in-situ* high speed x-ray imaging to monitor the printing of IN718 on SS316L substrate via PBF. They discovered the formation of the Laves phase due to non-equilibrium solidification and chemical inhomogeneity at the interface. It was also reported that the same chemical inhomogeneity may have improved mechanical properties by providing more interlocking at the interface. Finally, Yusuf et. al. [115] characterized the SS316L-IN718 diffusion zone with intermixed fused Fe and Ni with low porosity (~0.27%) and no cracks.

Another nickel superalloy with exceptional combination of oxidation and corrosion resistance and high temperature strength is Hastelloy X (HX) [116–119]. This alloy is known to be susceptible to hot cracking, namely solidification and ductility dip cracking, due to rapid cooling rates (~ 10^6 K/s) associated with PBF process [120]. Early efforts to process HX using PBF revealed ultrafine primary dendrite arms of less than 1 μm grown across several layers with fine precipitates formed in between [121,122]. In another early work, Tomus et. al. [123] showed that nucleation and propagation of cracks most likely occurs at grain boundaries due to microsegregation of Mn and Si. Optimizing the process parameters such as laser power, scanning speed, and hatch spacing and post processing treatments such as hot isostatic pressing (HIP) have shown to reduce the occurrence of micro-cracks and internal pores while improving mechanical properties [124,125].

Use of HX at large scale can be costly due to the presence of expensive alloying elements such as Co, Mo, and W. A multi-material approach using SS316L as the pairing alloy can reduce the material costs given that mechanical and metallurgical properties of a multi-material 316L-HX remain desirable. 316L stainless steel is arguably the most studied material for PBF process [126–128]. A typical 316L fabricated via PBF is known to have a FCC austenite phase with a

cellular microstructure and elongated columnar grains along the temperature gradient (build direction) [126,129]. 316L has a similar chemical composition and lattice structure to HX making it a promising pairing candidate for multi-material PBF [130].

To this aim, the present chapter provides first-hand knowledge of mechanical properties and interfacial characteristics of 316L-HX multi-material parts manufactured via PBF. Post-build examination of the interface is carried out using scanning electron microscopy (SEM) and energy dispersive spectroscopy (EDS). In depth study of mechanical properties using tensile and flexural testing is presented with a focus on plastic deformation and elongation followed by fractography of the fracture surfaces. It is shown that among various surface parameters, maximum valley depth (S_v) is inversely correlated to fatigue life [131–133]. Hence, surface metrology of the interface is performed to gain a better understanding of requirements for surface treatment procedures such as laser polishing to improve fatigue life and mechanical properties. Finally, the interface is revisited after tensile testing to investigate the presence of potential cracks and pores.

3.2. Experimental methods

3.2.1. Materials

Gas atomized 316L and HX powders used in this study were provided by EOS (GmbH, Germany) with particle diameter range of 10-50 μm . The chemical composition of both materials is listed in **Table 13**. It is well known that melt pool anatomy and dynamics significantly affects solidification and defect formation in PBF process [134]. Melt pool characteristics depends on process parameters and thermophysical properties of the material. For comparison, common thermo-physical properties of 316L and HX materials is listed in **Table 14**.

Table 13. Chemical composition (in wt %) of 316L and HX powders as provided by the supplier.

Element	Fe	Ni	Cr	Mo	Co	Mn	W	C	S
316L	Bal.	13-15	17-19	2.25-3	-	<2	-	<0.03	<0.004
HX	17-20	Bal.	20.5-23	8-10	0.5-2.5	<1	0.2-1	<0.1	<0.03

Table 14. Thermophysical properties of 316L and HX [86,135–137].

Symbol	Property	316L	HX
T_l	Liquidus temperature (K)	1723	1628
T_s	Solidus temperature (K)	1658	1533
C_p	Specific heat ($J.kg^{-1}.K^{-1}$) at 298 K	450	439
k_s	Thermal conductivity of solid ($W.m^{-1}.K^{-1}$) at T_l	13.8	10.4
k_l	Thermal conductivity of liquid ($W.m^{-1}.K^{-1}$) at T_l	16.8	29.0
α	Thermal diffusivity ($mm^2.s^{-1}$)	3.9	2.9
μ	Viscosity ($kg.m^{-1}.s^{-1}$) at T_l	0.008	0.0075
CTE	Coefficient of thermal expansion ($10^{-6}.K^{-1}$) at 773 K*	18.17	14.55
γ	Surface tension (N/m) at T_l	1.55	1.88
$d\gamma/dT$	Temperature coefficient for surface tension ($N.m^{-1}.K^{-1}$)**	-0.24×10^{-3}	-0.40×10^{-3}

* For samples fabricated via PBF in z direction

** Assumes negligible traces of sulfur and oxygen

3.2.2. Manufacturing

An EOS M290 (GmbH, Germany) system was used to manufacture 12 multi-material samples (three samples per group) as shown in **Fig. 16**. In this process, the first material was fully printed, then powder was swapped in the machine and the secondary material was printed directly over the already solidified first material. The system is equipped with a 400 W Yb/YAG fiber laser with a 1060 nm wavelength and beam diameter of 100 μm with Gaussian shape profile. The base plate was preheated to 80 °C, and an inert argon atmosphere was maintained during the fabrication process. Samples were made on 3 mm of support structure to avoid contamination by intermixing the base plate material during melting. As indicated in **Fig. 16**, 316L-HX refers to samples with 316L manufactured first followed by HX, and HX-316L refers to samples with HX manufactured first followed by 316L. This approach allows for a more comprehensive study of the interface since it accounts for gravity effects on melt pool formation, order of solidification, and material diffusion. Process parameters used to manufacture each material are adopted from the authors' previous work and are listed in **Table 15** [138]. These parameters have proven to yield the highest density (>99.5%) parts. It should be noted that samples were made with no contouring or modified parameters for top and bottom facing surfaces.

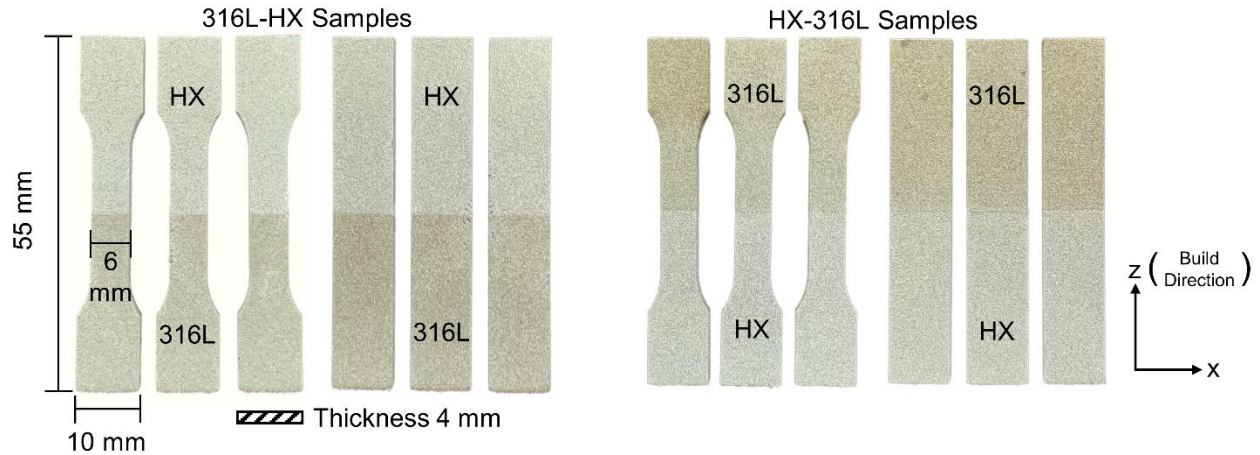


Fig. 16. Manufactured samples of 316L-HX and HX-316L. Critical dimensions are the same for both tensile and flexural specimens. Tensile test specimens gauge length is 30 mm.

Table 15. PBF process parameters for manufacturing of multi-material samples (recommended by the manufacturer).

Symbol	Parameter	316L	HX
P	Laser power (W)	195	195
v	Laser speed (mm/s)	1083	1150
h	Hatch spacing (mm)	0.09	0.09
t	Layer thickness (mm)	0.02	0.02
-	Scanning stripe width (mm)	5	5
-	Hatch reorientation (deg)	67	67

3.2.3. Surface metrology

A focus variant optical microscope (Alicona, InfiniteFocus G4, Austria) was used to measure the surface roughness across the interface of as-built multi-material samples and compare it with 316L and HX values. Surface profiles were acquired at 20x objective across a $1.4 \times 1 \text{ mm}^2$ area with $2.5 \mu\text{m}$ and 100 nm of lateral and vertical resolution, respectively. The overall form of the scanned surface was removed by removing the least-square plane with a robust fitting algorithm. The roughness profile was separated from the primary profile using a Gaussian filter with a cut-off wavelength of $250 \mu\text{m}$. The arithmetical mean height (S_a), and the maximum valley depth (S_v) of the surface were measured from an areal scan across a 1 mm^2 area. Calculations were in accordance with ISO 4287 [139] and ISO 25178 [140] guidelines, respectively.

3.2.4. Interfacial characterization

To characterize the microstructure at the interface, samples were cold mounted using epoxy resin. They were then polished using a diamond slurry in a series of steps with a reducing particle size of 9, 6, 3, and 1 μm . Final polishing was accomplished with 50 nm colloidal silica. All samples were thoroughly cleaned with acetone and isopropanol followed by deionized (DI) water. To reveal the microstructure features such as melt pool geometry, grain boundaries, and dendrites, samples were electrochemically etched in 70% phosphoric acid (H_3PO_4) and 30% DI water at 6 V for up to 30 seconds. It should be noted that this solution is more effective in etching HX. High magnification SEM micrographs of the interface microstructure were captured using a ZEISS LEO 1530 equipped with a field emission gun (FEG) and an EDS detector. Large area EDS analysis was performed across 2 mm with sampling increment of 10 μm for Fe, Ni, Cr, and Mo. It should be noted that EDS analysis was performed on samples prior to electrochemical etching. Same procedure was carried out for samples after tensile testing for post-fracture analysis.

3.2.5. Mechanical characterization

Tensile and flexural testing were carried out at room temperature using an MTS Sintech load frame (MN, USA) with a 5 kN load cell and 2.20 mV/V sensitivity. Tensile tests were performed at constant crosshead displacement rate of 2 $\text{mm}\cdot\text{min}^{-1}$ (strain rate of 0.001 s^{-1}) with data acquisition rate of 10 Hz. Strain measurements were conducted using digital image correlation (DIC) provided by Correlated Solutions (SC, USA). Zero-normalized squared difference algorithm was used to calculate longitudinal principal strains. It should be noted that true stress and true strain values were calculated from engineering stress and engineering strain data obtained from testing.

Flexural testing (3-point bending) was carried out with crosshead displacement rate of 5 mm/min with data collection frequency of 10 Hz. The downward force was exerted exactly on the interface while the support span was calculated to be 18 mm according to ASTM E290 [141].

3.3. Results

3.3.1. Surface roughness

Resulting surfaces from PBF process are typically irregular, with steep sided and re-entrant features [142]. One of the most commonly used surface parameters used to qualify surfaces is S_a , as defined previously. However, recent studies have shown that other surface parameters, specifically S_v , can better capture the relationship between surface roughness and mechanical properties of parts made via PBF [132]. Averaged S_a and S_v values with their standard deviations are presented in **Fig. 17**. According to **Fig. 17**. (b), both 316L-HX and HX-316L interfaces have higher values of S_v , followed by HX and 316L, respectively. This indicates that formation of interface between 316L and HX, regardless of printing order, diminishes the surface quality of multi-material PBF samples. Higher S_v values are associated with lower fatigue life, particularly in low cycles [132]. This observation has important implications for the design of multi-material components for fatigue.

A surface profile of each sample is shown in **Fig. 17**. (c). Samples exhibit a periodic peak and valley profile along the build direction which is indicative of the layer-wise manufacturing process of PBF. Both multi-material samples created large peaks in between two large valleys with the depth of approximately $40\ \mu\text{m}$ spanning across several layer thicknesses. According to **Fig. 17**. (c), the effect of multi-material interface on S_a and S_v is estimated to be $200\ \mu\text{m}$, i.e. ~ 10 layers. A more detailed look at the interface is presented in section 3.2. Overall, 316L exhibits the best surface quality, as represented by S_a and S_v values. Therefore, the surface quality of 316L should be considered as the base line for any surface improvement processes such as laser polishing for 316L and HX multi-material parts.

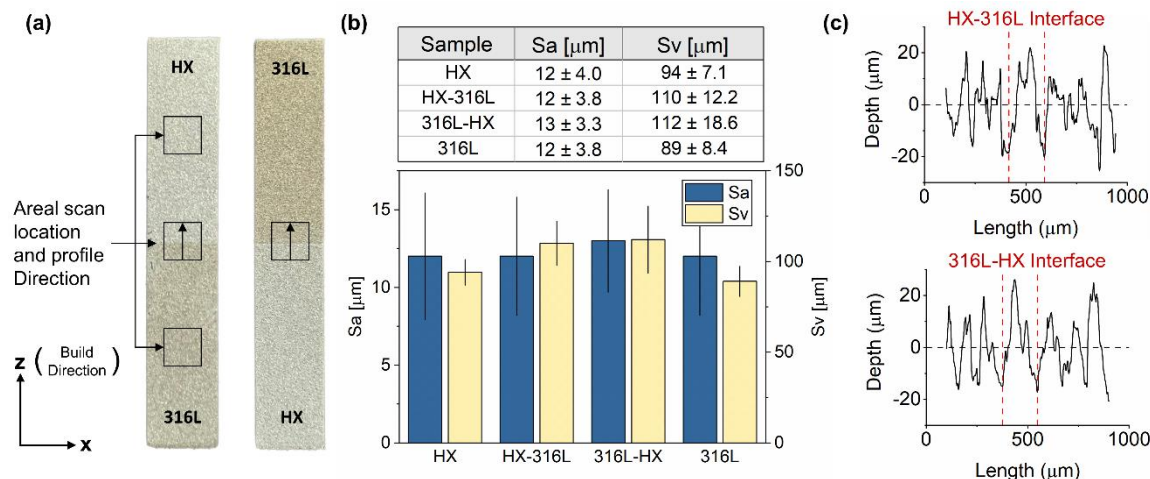


Fig. 17. Surface roughness results. (a) Showing the scan locations and directions on samples' surfaces. (b) Sa and Sv values. (c) Surface profile of each scan.

3.3.2. Interface microstructure

3.3.2.1. SEM analysis

The interfacial microstructure of HX-316L is shown in **Fig. 18**. Low magnification overviews of the interface in **Fig. 18. (a)** and **Fig. 18. (d)** reveal a sound graded interface with no visible pore or crack. **Fig. 18. (b)** and **Fig. 18. (e)** show the melt pool boundaries (white lines) formed in HX side and in the diffusion zone. Grain boundaries are shown in red, almost perpendicular to the melt pool boundary. These columnar grains are formed along the thermal gradient and in some instances continue across multiple melt pool boundaries indicating epitaxial growth. Formation of melt pool vortices are shown in **Fig. 18. (b)** using yellow arrows. Studies have shown that in PBF process, Marangoni force drives the flow from high temperature regions to low temperature regions thus creating two fluid vortices with opposite rotations in front and back of the laser beam path [134,143]. These vortices are also observed for other multi-material systems where the constituent materials possess different Marangoni numbers [104,105,110].

The typical cellular/dendritic solidification microstructure of HX is depicted in **Fig. 18. (c)** and **Fig. 18. (e)** with primary dendritic arm spacing (PDAS) of $0.4 \pm 0.03 \mu\text{m}$ and melt pool depth and width of ~ 60 and $\sim 100 \mu\text{m}$, respectively (supplementary **Fig. A1**). Several defects were

identified on the grain boundary as shown by red arrows. According to the magnified inset in **Fig. 18. (c)**, these defects were sub-micron in size and appeared to be caused by intermetallic inclusions that were pulled out during sample preparation. Evidence for existence of these inclusions is provided in Supplementary **Fig. A2**. The same defects were previously observed for HX and characterized to be carbides formed as a result of thermal cycling during PBF process [144,145]. In addition to formation of intermetallics, some gas pores were observed on grain boundaries and within grains as shown by white arrows in **Fig. 18. (e)**. These defects are common in PBF processing and are due to key-hole instability during laser melting [32]. There were no noteworthy defects observed in 316L side of the samples. Overall, there were no defects observed at the diffusion zone to suggest multi-material processing of HX-316L as the primary cause.

Microstructural analysis of 316L-HX samples revealed similar features and defects as HX-316L (**Fig. 19**). Intermetallic defects on grain boundaries of HX, and melt pool vortices due to Marangoni convection in the diffusion zone are shown in **Fig. 19. (b)** and **Fig. 19. (c)**, respectively. The cellular/dendritic microstructure with columnar grains in the diffusion zone is shown in **Fig. 19. (e)**. The presence of the same intermetallic defects on grain boundaries and the same PDAS indicate that HX microstructure is dominant within the diffusion zone. No other visible defects were observed at the interface that suggest multi-material processing as the cause.

The diffusion zone appears to be larger than that of HX-316L as indicated in **Fig. 19. (a)** and **Fig. 19. (d)**. However, the electrochemical etching solution was more effective in revealing the HX microstructure than 316L. The diffusion zone for HX-316L is rich in Fe, as a result the etching did not fully reveal the melt pool boundaries. On the other hand, the diffusion zone in 316L-HX is rich in Ni which resulted in a stronger reaction with the etchant revealing the melt pool

boundaries and microstructure of the entire diffusion zone. This is later confirmed by EDS analysis presented in section 3.3.2.2.

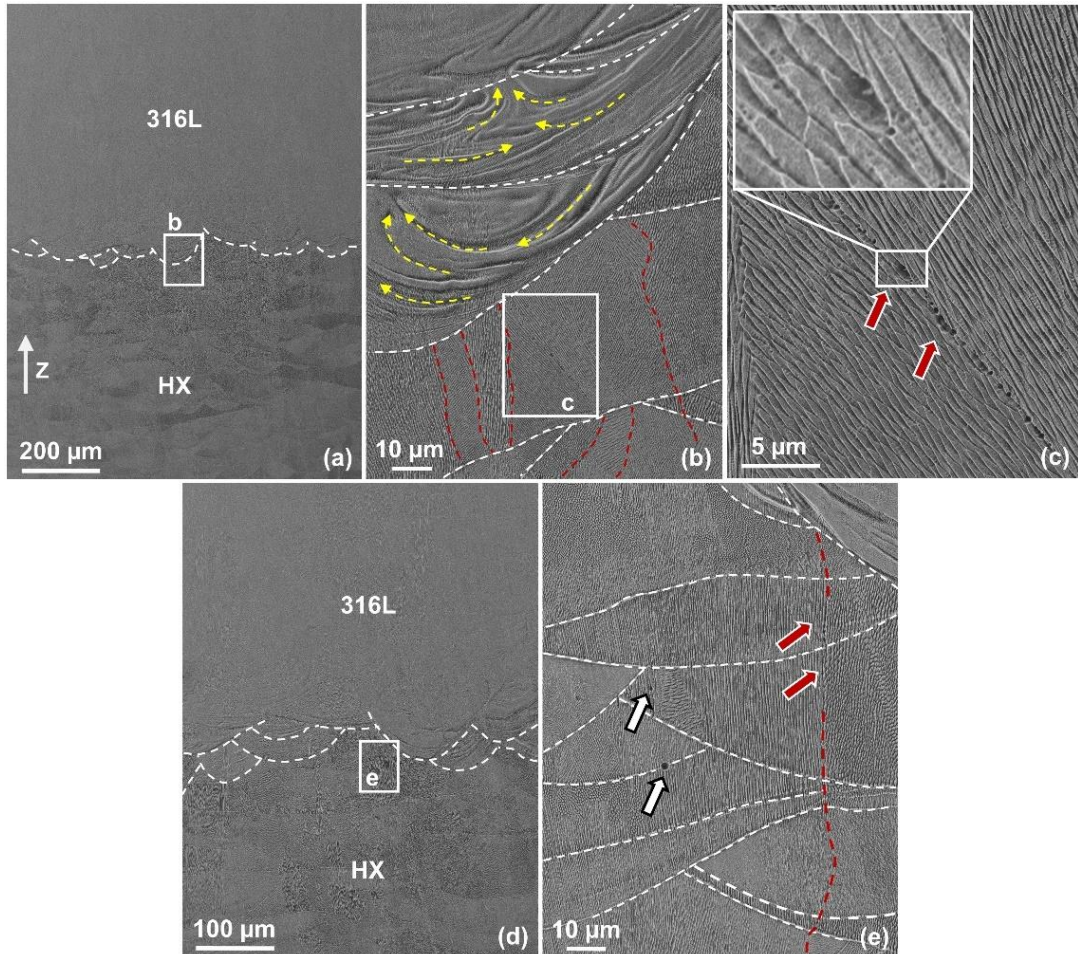


Fig. 18. SEM image of HX-316L interface: (a,d) low magnification overview of the interface, (b) melt pool vortices in the diffusion zone, (c,e) microstructural defects in HX.

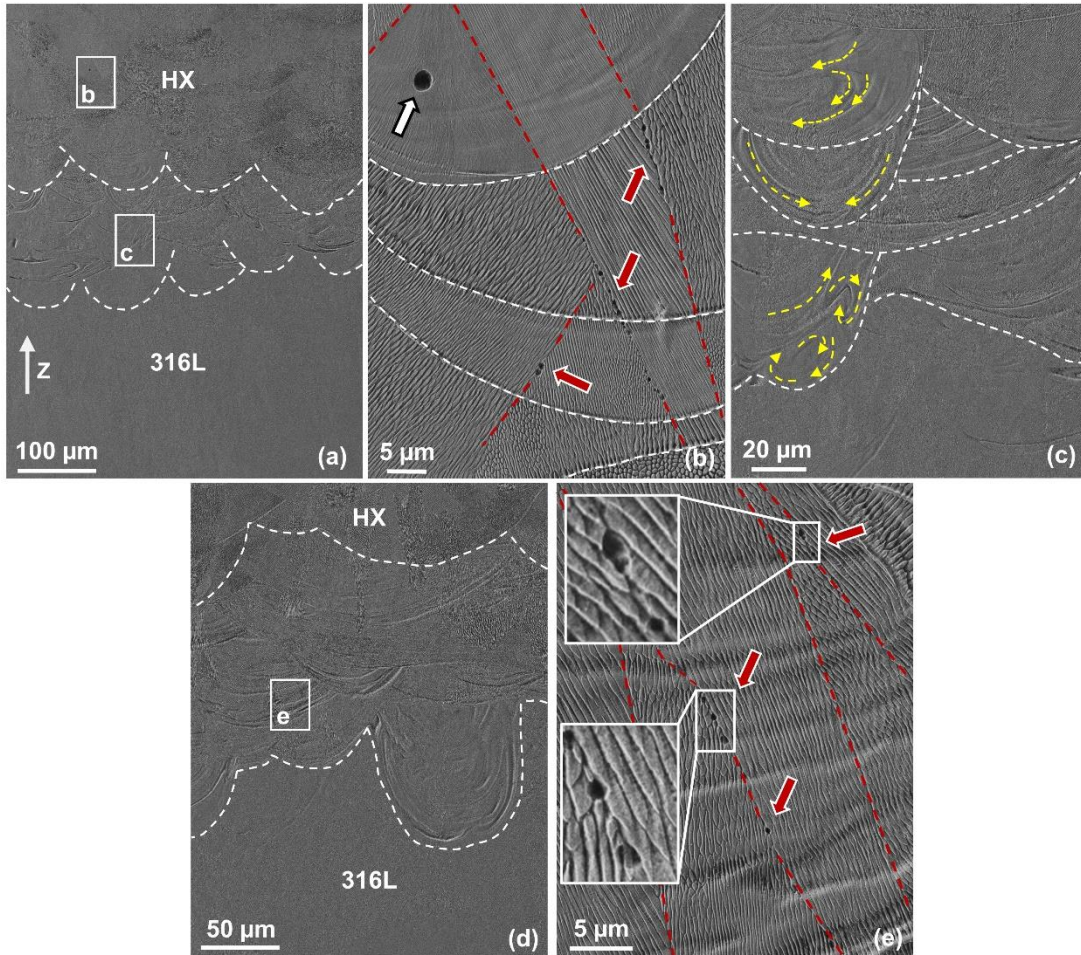


Fig. 19. SEM image of 316L-HX interface: (a,d) low magnification overview of the interface, (b) high magnification view of HX microstructure and defects, (c) melt pool vortices in the diffusion zone, and (e) HX dominant microstructure in the diffusion zone.

3.3.2.2. EDS analysis

To quantify the length of the diffusion zone between 316L and HX at the interface, EDS analysis of 316L-HX and HX-316L is shown in **Fig. 20. (a)** and **Fig. 20. (b)**, respectively. The diffusion zone, highlighted in yellow, starts when the content of the main alloying element for each material, i.e. Fe for 316L and Ni for HX, deviates from their average value. The end of the diffusion zone is marked by the return of these elements to their average weight % for each alloy. According to **Fig. 20**, the diffusion zone for 316L-HX and HX-316L are both approximately 240 μm . This is in agreement with the estimates from surface metrology and SEM analysis. The similar diffusion zones indicate that gravity and buoyancy forces have little effect on melt pool dynamics.

According to the weight % of each element shown in **Fig. 20**, the diffusion zone for 316L-HX is rich in Ni, while the diffusion zone in HX-316L is rich in Fe. In both cases Cr has the second largest weight % in the diffusion zone. This supports the argument made in section 3.2.1 regarding the etchant interaction with the elements within the diffusion zone. It can also be concluded that the secondary material, i.e. the material printed on top of the primary material, dominates the composition of the diffusion zone. It has been shown that the depth of melt pools formed in key hole mode covers multiple layer thicknesses for 316L and HX [125,146]. However, the melt pool depth greatly diminishes for the first few layers that are printed above a solid substrate [110,114], because the energy required to melt a solid substrate is much greater than the energy required to melt the same material in powder form [147]. Therefore, the remelted material from the primary material diffuses into the melt pool during the printing of the first few layers, and as the print progresses the melt pool no longer penetrates the primary material causing the diffusion to dissipate. Fluid vortices that are caused by Marangoni flow help stir the elements, creating a compositional gradient within the diffusion zone. In case of 316L and HX, the material diffusion dissipates after $\sim 240 \mu\text{m}$, or about 10-12 layers. **Fig. 20. (a)** also showed that Fe and Ni reached their respective inflection points almost in the middle of the diffusion zone, whereas **Fig. 20. (b)** showed that the inflection points were reached at the beginning of the diffusion zone. This indicates that 316L-HX experienced more intermixing than HX-316L.

More rigorous work is required to understand the underlying mechanisms of elemental distribution across the interface which will be the subject of future studies.

3.3.3. Tensile test

Tensile tests were performed to evaluate the bond strength of 316L and HX interface. Stress-strain curves and mechanical properties are presented in **Fig. 21**. Three 316L, and three HX samples were tested to create a baseline for comparison. HX exhibits higher values of yield

and ultimate strength compared to 316L at 527 and 649 MPa, respectively. Both HX and 316L exhibit similar ductility with 62.1% and 62.7% rupture strain, respectively.

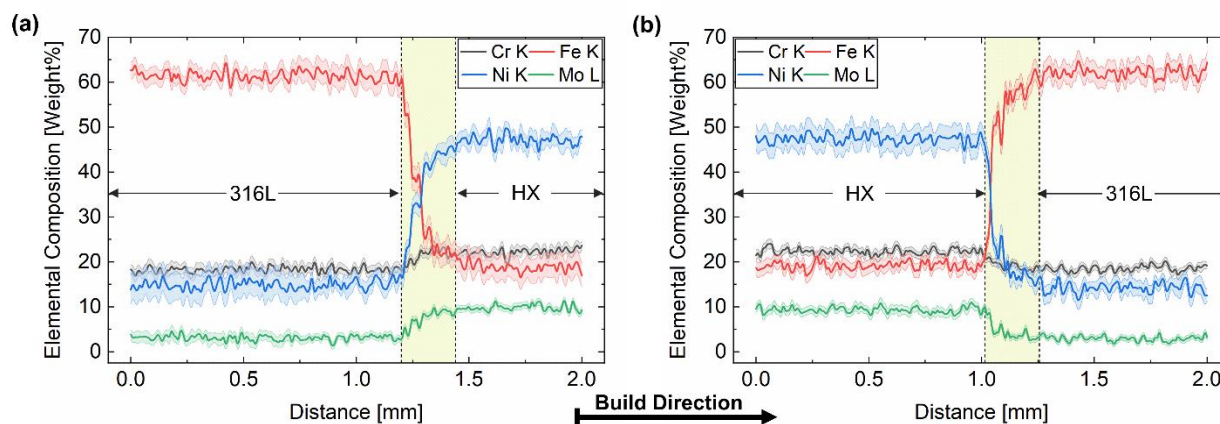


Fig. 20. EDS line scans of (a) 316L-HX, and (b) HX-316L. The highlighted area indicates the diffusion zone for each multi-material system.

The images of fractured samples in **Fig. 21. (b)** show that failure occurred in 316L side of the samples and about 7 mm away from the interface. Both HX-316L and 316L-HX performed similarly during testing. **Fig. 22** shows the strain map of both multi-material samples at four critical points during the tensile test: onset, yield, ultimate, and fracture. It is evident that samples yielded at 316L side away from the interface while the HX side of the samples experienced very little to no strain. Maximum strain values on HX side at the moment of yield were 0.6% and 0.7% for 316L-HX and HX-316L, respectively. Necking occurred when samples reached their ultimate strength. At this moment, the HX side experienced almost zero strain and necking continued in the 316L side until failure. However, the interface showed 7.8% and 6.6% strain at ultimate strength for 316L-HX and HX-316L, respectively. At failure, the strain values for the interface reached 23.1% and 25.8% for 316L-HX and HX-316L, respectively.

3.3.4. Flexural test

To further evaluate the bond integrity at the interface, 3-point flexural bending test was carried out. The force was exerted directly on the middle of each sample resulting in maximum shear stress and bending moment at the interface. Flexural stress-flexural strain curves are

depicted in **Fig. 23**. Similar to the tensile test, both HX-316L and 316L-HX samples performed similarly with flexural yield strength of 273 MPa and 275 MPa, and flexural strength of 543 MPa and 558 MPa, respectively (**Fig. 23. (c)**). Multi-material samples exhibit higher flexural yield and flexural strength compared to 316L. Samples yielded at the 316L side during testing, resulting in an asymmetrical deflection as shown in **Fig. 23. (b)**. Overall, there were no visible cracks at the interface after testing was terminated indicating a successful bonding between 316L and HX.

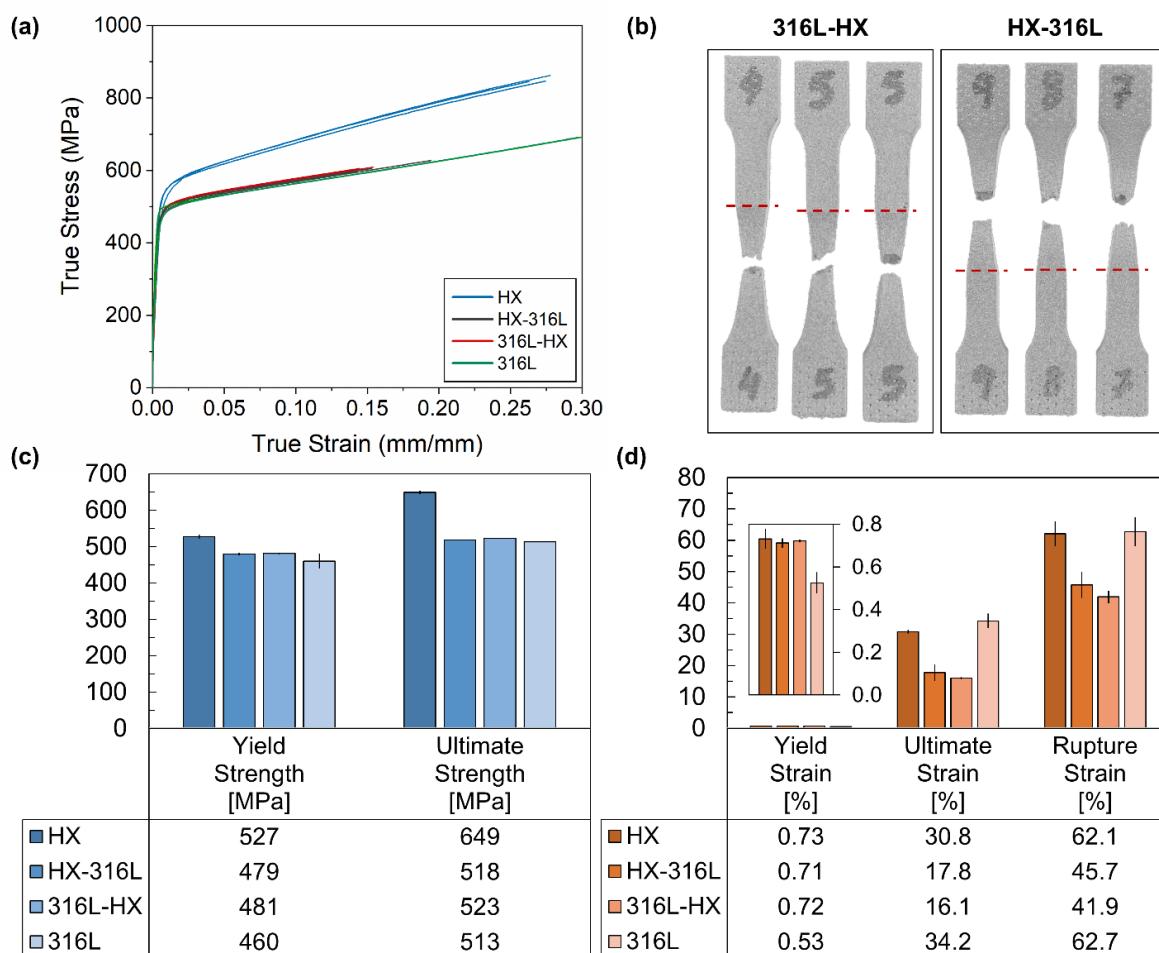


Fig. 21. Tensile test results of 316L, HX, and multi-material samples. (a) stress-strain curves, (b) failed samples. The red dashed lines indicate the interface, (c) comparison of yield and ultimate strengths, and (d) comparison of strains.

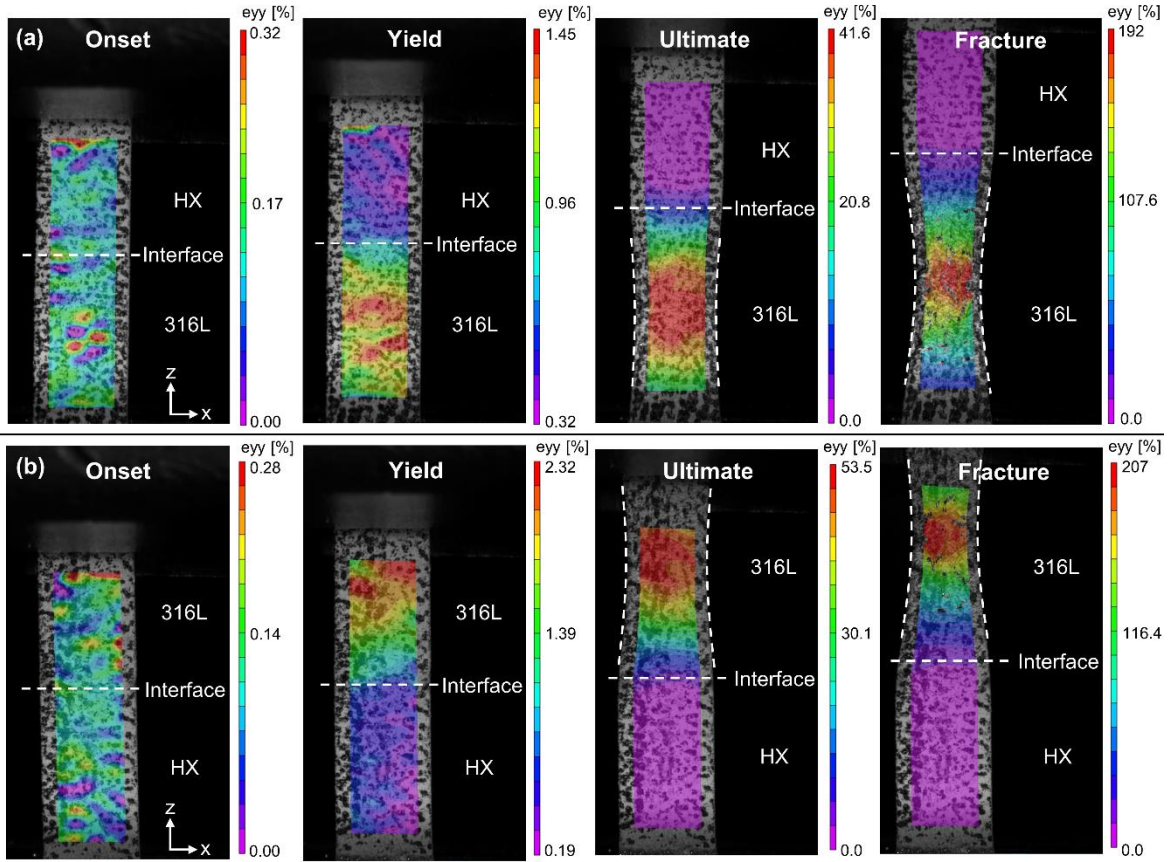


Fig. 22. Strain map at four critical moments of the tensile test: (a) 316L-HX sample, (b) HX-316L sample. The color scale shows the strain distribution across the sample at every moment during the test.

3.3.5. Post-fracture analysis

To study the effects of tensile testing on the interface, post-fracture EDS analysis was carried out (**Fig. 24**). Results showed the diffusion zones extended to approximately 300 μm for 316L-HX, and 400 μm for HX-316L as expected from the tensile test results. This translates to 25% and 66% elongation at the interface, indicating the ductile nature of the interface. The integrity of the interface was further verified by post-fracture SEM analysis (**Fig. 25**). The characteristic features of the diffusion zone, including melt pool vortices, remained unchanged after tensile testing. Results confirmed that the interface remained free of cracks or pores even after experiencing strain during tensile testing.

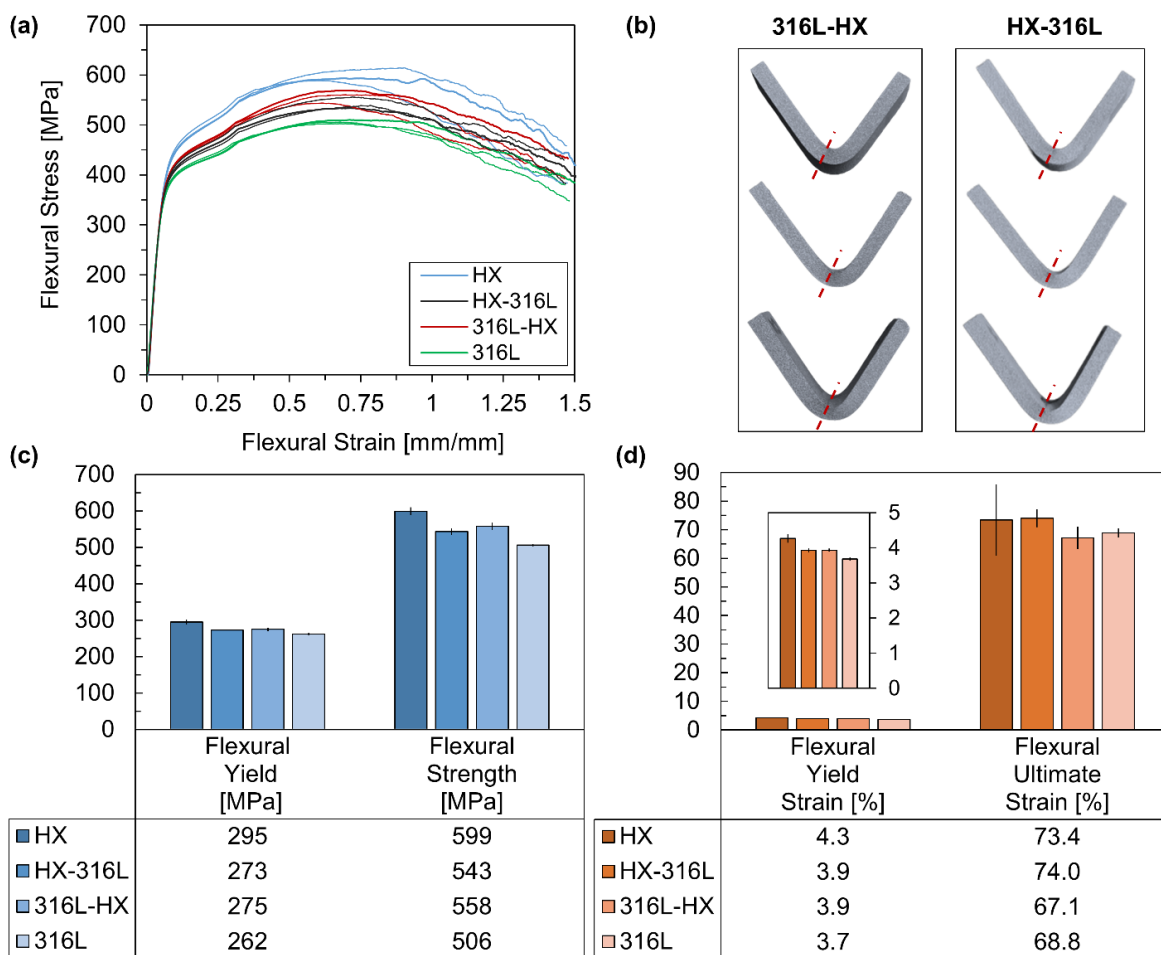


Fig. 23. Flexural test results of 316L, HX, and multi-material samples. (a) stress-strain curves, (b) failed samples. The red dashed lines indicate the interface, (c) comparison of flexural yield and flexural strengths, (d) comparison of strains.

Finally, the fracture surfaces of multi-material samples were observed using SEM (**Fig. 26**). As expected, fracture surfaces of both 316L-HX and HX-316L samples showed similar features which were typical of 316L manufactured via PBF [148–150]. Distribution of inhomogeneous dimples with sizes ranging from a few hundred nano meters to a few microns were observed which indicate that the primary mode of fracture was ductile. The white arrows in **Fig. 26. (c)**, and **Fig. 26. (f)** point to submicron inclusions that sit at the bottom of the dimples. These inclusions were likely formed as a result of remnant oxide layer on powder particles reacting with the alloying elements, triggering micro-crack nucleation and the eventual fracture [151]. It can be concluded that multi-material processing of 316L and HX did not affect the fracture mechanics of 316L.

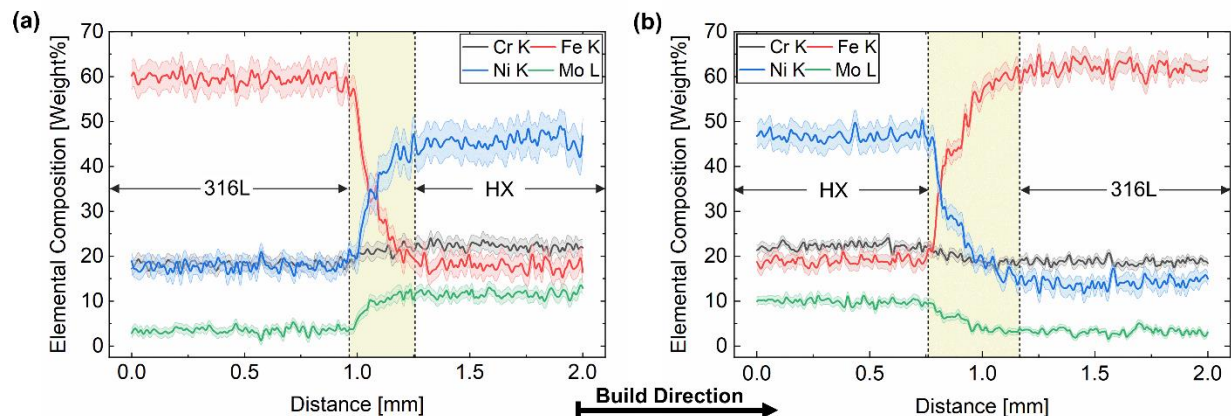


Fig. 24. Post-fracture EDS line scans of (a) 316L-HX, and (b) HX-316L. The highlighted area indicates the diffusion zone for each multi-material system.

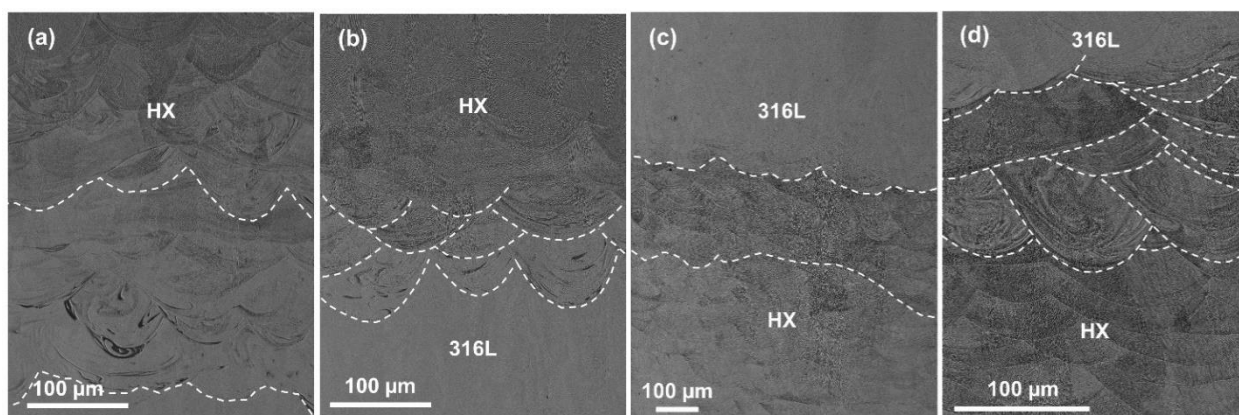


Fig. 25. Post-fracture SEM analysis of multi-material samples at different magnifications: (a,b) 316L-HX, and (c,d) HX-316L. White dashed lines indicate melt pool boundaries at the interface.

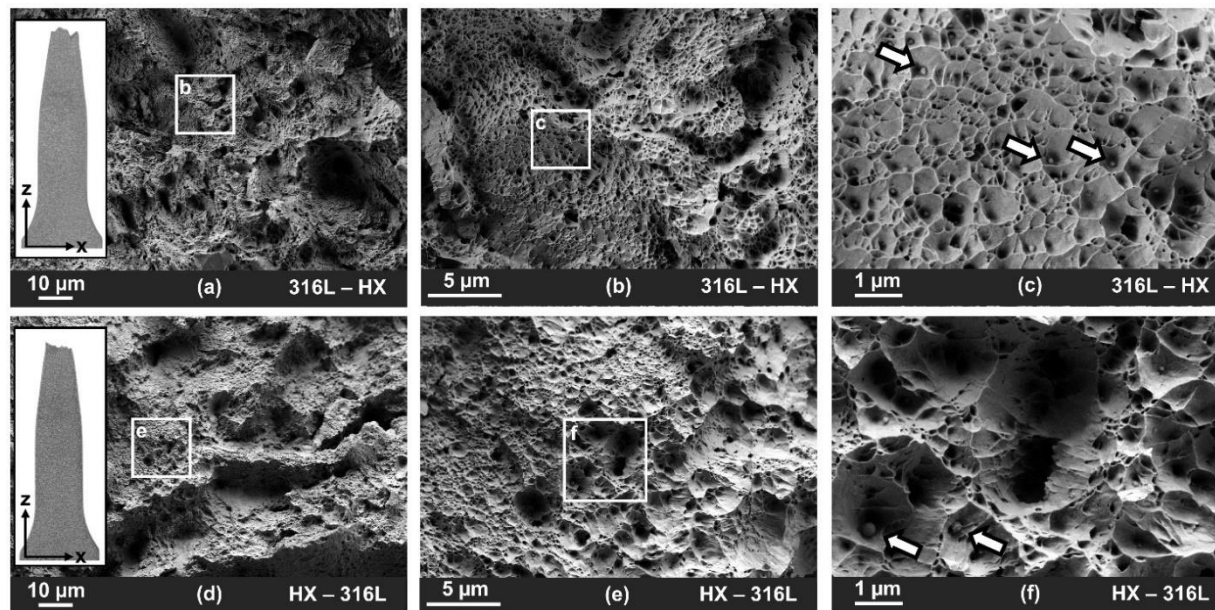


Fig. 26. SEM image of fracture surfaces from low to high magnification. (a-c) 316L-HX, and (d-f) HX-316L.

3.4. Discussion

3.4.1. The diffusion zone

Studies have shown that a gradual change in materials composition at the interface improves the bond in multi-material PBF, compared to sharp transitions [99]. For materials with dissimilar thermophysical properties, such as Invar 36 and Cu10Sn, the compositional gradient at the interface must be engineered if detrimental defects are to be avoided [104]. In 316L and HX case, the “naturally” formed interface created a compositional gradient which was defect free thanks to similar thermophysical properties and processing parameters of materials. These similarities will be discussed in this section.

Both 316L and HX share an austenitic FCC crystal structure. Additionally, the CTE for 316L and HX are 18.2 and 14.5 ($10^{-6} \cdot K^{-1}$), respectively (**Table 14**). The similar CTE values plays a role in reducing thermal stress concentration at the interface, thus preventing crack propagation and layer delamination during cooling [99]. Another factor in preventing embrittlement and cracking of the interface is satisfactory solubility levels of the main alloying elements, Fe, Ni, and Cr [152]. Proper diffusion of materials at the interface depends on melt pool depth, and speed and direction of melt flow. The melt pool depth determines the potential contribution of the primary material (already solidified material), the speed and direction of the flow determines proper intermixing of the elements driven by Marangoni force [114]. The melt pool depth of 316L was taken from a previous study to be $\sim 68 \mu m$ [146], while the melt pool depth of HX was measured to be $\sim 60 \mu m$. The contribution of each material to the interface during melting can also be measured using the volumetric energy density:

$$E_d = \frac{P}{vht} \quad (9)$$

E_d determines the amount of input energy per volume of material. E_d for 316L and HX based on process parameters listed in **Table 15** is 100 and 95 J/mm^3 , respectively. A universal form of the

input energy was introduced by authors in a previous work which accounts for the contribution of specific heat and thermal conductivity of materials [138]:

$$\Pi_2 = \frac{c_p}{k_s} E_d \tau \quad (10)$$

where $\tau = d/v$ is laser dwell time, and d is laser beam diameter. Π_2 values of 316L and HX for process parameters listed in **Table 15** are 301 and 348, respectively. This indicates that the ratio of heat storage to heat dissipation at a unit time for a given input energy is similar for both materials.

The direction of the melt pool flow is mostly determined by Marangoni force which drives the flow from high to low temperature region of the melt pool for materials with a negative temperature coefficient of surface tension [143]. Effects of buoyance and gravity in PBF melt pool dynamics are often negligible owing to the small dimensions of the melt pool [78]. Effects of Marangoni force on the melt pool can be quantified by the Marangoni number:

$$Ma = -\frac{d\gamma}{dT} \frac{L\Delta T}{\mu\alpha} \quad (11)$$

where L is the characteristic melt pool length, and ΔT is the difference between maximum temperature of the melt pool and solidus temperature. Larger Marangoni number translates to stronger convective flow at the head of the melt pool which can trigger fluid vortex formation [143]. Melt pool vortices can help with materials mixing during multi-material melting [99]. Therefore, at least one material with a high Marangoni number may be required to achieve proper intermixing within the diffusion zone. To provide an estimate for the Marangoni number for 316L and HX, L is considered to be the melt pool width, estimated at $\sim 120 \mu\text{m}$ for 316L according to [146], and $\sim 100 \mu\text{m}$ for HX according to **Fig. A1**. The maximum temperature in the melt pool is assumed to be the material's liquidus temperature. With these assumptions, and the properties listed in **Table 14**, the Marangoni number for 316L and HX can be estimated at 60 and 175. Larger Marangoni number promotes more convective flow, and therefore more intermixing. The higher Marangoni number of HX can explain why 316L-HX experienced better intermixing in the diffusion zone.

A summary of influential thermophysical properties and quantitative tools that can aid in pairing of alloys for multi-material processing via PBF is presented in **Table 16**. Although the proposed list is not comprehensive, it can provide insight into whether a “natural” or an “engineered” interface would be needed for a chosen multi-material pair.

Table 16. Summary of influential parameters and properties in multi-material processing of 316L and HX.

Symbol	Parameter	316L	HX
-	Crystal structure	Austenitic FCC	Austenitic FCC
CTE	Coefficient of thermal expansion ($10^{-6}.K^{-1}$)	18.2	14.5
E_d	Energy density (J/mm^3)	100	95
Π_2	Dimensionless number defined in [138]	301	348
Ma	Marangoni number	60	175

3.4.2. Mechanical properties

The ultimate and fracture strain of multi-material samples were significantly lower than 316L. This seems to be contradictory to the fact that for the same material, a sample with shorter gauge length always provides a higher fracture strain than a sample with a longer gauge length. This behavior can be explained by considering that ductile materials elongate only within the necking region after they reach their tensile strength, and the spatial dimensions of the necking region are almost identical regardless of the length of the test specimen [153]. Since the 316L side of multi-material samples are almost half the gauge length of 316L samples, the necking strain accounts for a disproportionately high fraction of the total strain. Therefore, the multi-material samples should have significantly higher fracture strains than 316L.

The apparent contradiction can be explained by considering how strain was calculated. Strain values reported in **Fig. 21** were averaged across the entire sample. However, in a 316L and HX multi-material case, this approach can be misleading because strain values on half of the sample (HX side) were close to zero and that significantly lowered the strain average across the entire sample. According to **Fig. 22**, the maximum strain at fracture for 316L-HX and HX-316L were 192% and 207%, respectively. Whereas the maximum strain at fracture for 316L was 147%,

significantly lower than multi-material samples. This agrees with the expected plastic behavior of samples with shorter gauge lengths. This observation can have important implications for mechanical design of multi-material components where elongation will no longer be uniformly distributed across the components.

It should be noted that the experiments designed in this work require remelting of the primary material for diffusion and formation of the interface. Future work should focus on multi-material processing of materials that are adjacent to one another, where both materials experience melting and solidification simultaneously.

3.5. Conclusions

This chapter studied the multi-material processing of 316L and HX via PBF and provided direct observations of multi-material interface, microstructure, and mechanical properties of 316L-HX and HX-316L systems. SEM and EDS analysis of the interface showed no evidence of cracking or porosity. Mechanical testing proved sound bonding with no evidence of embrittlement at the interface. The following conclusions can be drawn from the results presented in this work:

- A ~240 μm (10-12 layers), defect free, compositional gradient was formed at the interface of 316L and HX using process parameters suitable for each individual material. The interface was rich with the major alloying element of the secondary material. i.e. Ni for 316L-HX and Fe for HX-316L samples.
- Evidence of melt pool vortices due to Marangoni convection was observed for both 316L-HX and HX-316L samples indicating mixing of alloying elements within the melt pool.
- Formation of the interface increased the surface roughness. Multi-material samples showed higher levels of S_v at their interface compared to 316L or HX surfaces.
- During tensile testing, multi-material samples failed at 316L section some 7 mm away from the interface. Both multi-material samples performed similarly, indicating that solidification order did not affect the bond.

- At failure, the strain values for the interface reached 23.1% and 25.8% for 316L-HX and HX-316L, respectively, while HX experienced almost no strain. No evidence of cracking or voids were found within the interface region after tensile testing.
- No evidence of defect was found at the interface after flexural test indicating the ductile nature of the interface.
- The sound bonding, and mechanical performance of 316L and HX multi-material samples was attributed to similar thermophysical properties, and crystal structure of alloys. Use of a few quantitative tools were suggested to aid in choosing proper pairing alloys for multi-material PBF.
- The following quantitative parameters (coefficient of thermal expansion, energy density, dimensionless number Π_2 , and Marangoni number) were proposed to provide insight into whether a “natural” or an “engineered” interface would be needed for a chosen multi-material pair.

Chapter 4: Compositional Grading of 316L-Cu Using Machine Learning

4.1. Introduction

The popularity of metal AM continues to grow as both a research topic and an industry solution [68]. Among the main metal AM techniques, SLM remains the most studied technique [68]. An extensive Delphi study on economic and societal implications of AM predicted that by 2030 a significant amount of AM-produced products will consist of multiple materials and/or contain electronics, enabling a broad range of applications [67]. This prediction is supported by the growing number of publications on AM with multiple materials and functionally graded materials (FGMs) in recent years [154–156], and emerging industry trends [157]. In this work, the focus is on metal AM, and any mention of multi-material hereafter excludes polymers and ceramics. In the context of this work, multi-material AM is defined as an AM process capable of creating complex geometries from multiple metals or metal alloys where the positioning of each material (compositional grading) within the part is designed and controlled to serve a specific function or enhance a specific property. It should be noted that the requirement for complex geometries implies that DED techniques are not suitable for the category of applications envisioned for this definition. A multi-material AM process that fits this definition can have transformative impact on industry. For example, light-weighting using multi-material generative design [19,158] has shown to result in higher compliance per weight fraction than single-material generative design. Graded structures in FGMs reduce the interfacial residual stress levels, thereby enhancing thermophysical and mechanical properties [155]. Wear and corrosion resistance, as well as part-level heat and electrical conductivity management can be designed and incorporated in multi-material parts with compositional grading [159]. Moreover, the benefits can extend beyond individual parts and impact the AM value chain. For example, compositional grading in AM can replace other manufacturing processes such as coating technologies. Part

consolidation can be done across materials, thereby reducing the need for assemblies and failure prone permanent and nonpermanent joints. As a result, manufacturing costs, footprint, and lead time can be significantly reduced.

Before the potential of multi-material AM can be realized, several technical challenges must be addressed. Early efforts have been made in the 1990s to incorporate multi-material capability in the SLM process at laboratory scale with a focus on developing novel powder delivery systems capable of handling multiple materials [160–166]. However, a successful integration of a multi-material powder delivery system and the SLM process was not reported until 2018 by Wei et al. [167] where 316L-Cu10Sn and 316L-In718 components were successfully manufactured. In another work Wei et al. [168] demonstrated the fabrication of 316L-Cu10Sn components with varying compositional gradient within and across layers. Similar work has been done on other hybrid materials such as glass-Cu using vibration assisted micro dosing of metal powder and *in situ* mixing [169]. It should be noted that these studies demonstrate a compositional gradation at the interface of two materials in 3D, an approach that fits the definition of multi-material AM within the context of this work. Other studies investigated the one dimensional interfacial bond between two dissimilar materials fabricated via SLM with a focus on characterization [105,170–172]. For example, Liu et al. [103] manufactured bi-metallic laminates of steel/Cu using SLM. They reported successful metallurgical bonding with highly refined microstructure due to rapid solidification. In another study, Sing et al. [108] carried out multi-metal processing of C18400 copper alloy and AlSi10Mg using SLM. They reported the formation of intermetallic compound Al_2Cu during the process at the bonding interface between the two materials. These studies highlight the possibility of achieving multi-material parts with compositional gradients from the standpoint of hardware and material design. Currently, to the best of the authors' knowledge, there is no systematic approach for determination of suitable process parameters for additive manufacture across compositional gradients in multi-material parts.

To develop a framework for determining suitable process parameters for multi-material parts, a better understanding of the SLM process is required. But researchers are faced with two major challenges: the complex physics of the process and more than 100 adjustable, material-dependent process parameters. Many strides have been made to study the SLM process by developing multi-scale and multi-physics models [134,147,173–175]. These models have played a fundamental role in expanding our understanding of the SLM process, but their computational cost remain prohibitive. Effects of process parameters on part quality, microstructure, and mechanical properties have also been experimentally investigated [71,72,176–178]. Depending on the chosen metric, full factorial design of experiments can be costly and time consuming. Therefore, this approach, although proven useful, is not yet practical for creating overarching process-property relationship maps, not to mention the added complexity of multi-material AM process.

High throughput experiments have shown to be an effective substitute for full factorial design in various research on characterization [146] and process-property relationship mapping [179]. Introduced to material sciences in 1990s [180–182], combinatorial and high throughput experiments are characterized by synthesis of a “library” sample that contains the materials variation of interest (e.g., composition, density, tensile strength), and rapid measurement schemes that result in large data sets at unprecedented speed and cost [183]. Although high throughput experimental methods have traditionally been used for materials discovery [184], today’s challenges in advanced manufacturing and materials science have brought upon new applications for this methodology. High throughput experimentation has been presented as an ideal experimental complement that can help bring the vision of the materials genome initiative [185] to fruition [186–188]. Moreover, it has proven to be an effective method to generate training data sets for various machine learning methods used in materials design and AM [189–191] to combat the high cost and long development times of large training data sets.

Machine learning, complemented by high throughput experiments, is an approach that can simplify the process of finding suitable SLM parameters and avoid high costs associated with experiments and testing. Machine learning algorithms are juxtaposed with physical models. These algorithms bypass the computational burden associated with running multi-physics and multi-scale simulations and offer the ability to gain insightful knowledge and identify relationships in large AM data sets [192]. Models built with machine learning can be used for design, quality/process optimization [193], predicting part's thermal history [194], *in situ* monitoring and defect detection [195], and security and cyberattack detection [196,197]. A wide range of machine learning techniques have been applied to predict process-property relationships for various mechanical and physical properties of single-material AM such as density, melt pool geometry, toughness, and wear strength [76,198–202]. Among these techniques, the Gaussian process has shown to be an attractive regression-based machine learning method for predicting process-property relationships. Gaussian process surrogate modeling has been successfully used to predict porosity and melt pool depth levels with respect to laser power and speed for 316L and 17-4 PH stainless steel [74,75,203]. Supervised learning problems in machine learning, which can be thought of as learning a function from examples, can be directly integrated into the Gaussian process framework. By doing so, one can take advantage of the relative simplification of computations required for inference and learning in Gaussian processes compared to artificial neural networks [204]. Currently, there are no implementations of machine learning in multi-material AM.

In this work, a machine learning algorithm is developed based on a multivariate Gaussian process to predict the suitable process parameters necessary for manufacturing the compositional gradient zone of a 316L-Cu multi-material part using SLM as demonstrated in [168]. The developed multivariate Gaussian process approach provides a framework that facilitates transfer of knowledge from 316L and Cu to 316L-Cu compositions in predicting its material properties under study. The training data is density and surface roughness, which is

experimentally mined from manufactured samples of 316L, Cu and compositions thereof. Density and surface roughness are chosen as metrics for part porosity and fit for service, respectively. In addition, these two figures of merit can be measured in a high throughput fashion. It is well documented that the main SLM process parameters, i.e., laser power (P), speed (v), layer thickness (t), and hatch spacing (h) are material-dependent and are directly correlated to porosity and surface characteristics in a part [71,72,146,205,206]. However, how these parameters should change as a function of a material's composition is still unknown. This work provides first-hand knowledge of process-property relationship in a compositional gradient zone of 316L-Cu multi-material part by leveraging a unique machine learning approach.

This chapter is organized in four main sections plus conclusions and two appendices: Section 4.2 focuses on the high-throughput experimental procedures used in collecting the training data with complementary details added in Appendix B. Section 4.3 provides a first look at the collected data and discusses the effects of process parameters on part density and surface roughness. Development and validation of the multivariate Gaussian process model is the focus of Section 4.4. The structure and formulation of the algorithm is discussed followed by cross-validation results. The details of the mathematical derivations are presented in the Appendix C. Section 4.5 presents the predictions for density, surface roughness, and the corresponding process parameters in form of process maps followed by statistical analysis to provide more insight into the differences observed in the maps. The process maps are then used to predict the suitable process parameters for grading a 316L-Cu multi-material part. Finally, concluding remarks and future research opportunities are presented in Section 4.6.

4.2. Materials and Methods

4.2.1. Overview

The chosen approach to predict the process parameters of 316L-Cu compositions is inspired by the experimental work done by Wei et al. [168] on multi-metal AM of 316L-Cu10Sn

where the multi-material interface is compositionally graded to achieve sound metallurgical bonding during the SLM process. In [18], pre-mixed 316L-Cu10Sn powder at three different compositions are deposited to create a compositional gradient from 316L to Cu10Sn. In this work, 316L and Cu are used and the continuous gradient zone that would form at their interface is discretized into three regions with prescribed compositions, similar to [18]. These compositions are determined by mass fractions as:

$$m_{f_{Cu}} = \frac{m_{Cu}}{m_{Cu} + m_{316L}} \quad (12)$$

Where m_{Cu} and m_{316L} are mass of Cu and 316L powders, respectively. Samples are then made from 316L, Cu, and their compositions at pre-mixed $m_{f_{Cu}} = 0.25$, $m_{f_{Cu}} = 0.50$, and $m_{f_{Cu}} = 0.75$. Part density (ρ) and average surface roughness (Sa) of the top surface are measured and used as training data. **Fig. 27** depicts the schematic of the proposed work. The details of the data mining process are discussed in the following sections.

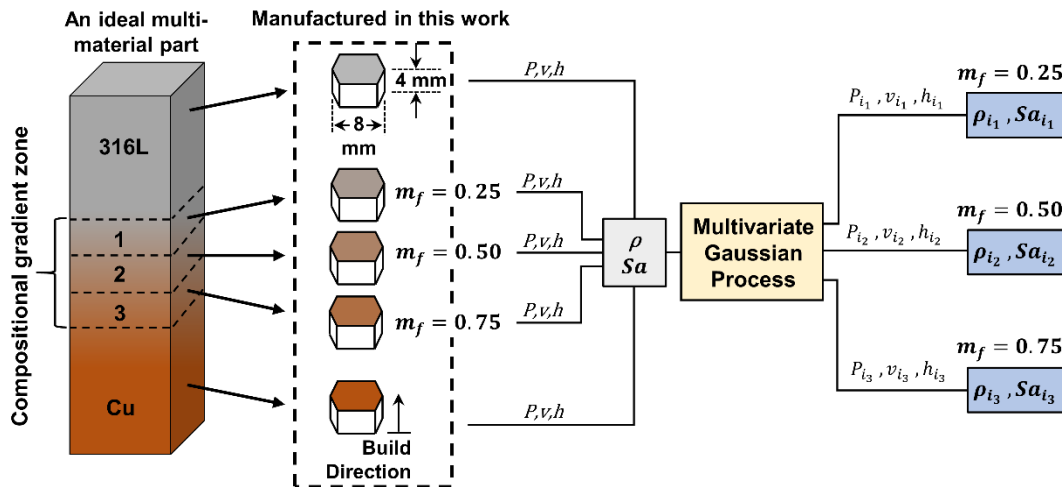


Fig. 27. An overview of the proposed method. The hexagonal samples were manufactured using pre-mixed compositions to represent an ideal continuous gradient zone.

4.2.2. Powder characteristics and mixing

Gas atomized 316L powder used in this study were provided by EOS GmbH, Germany and the Cu powder was supplied by Carpenter Technology, USA. Powder granulometry was performed according to ASTM F1877 [207] where the equivalent circle diameter (ECD) was used as the measure of particle size. A Keyence VHX-5000 digital microscope was utilized to collect the geometrical data needed to calculate ECD. **Fig. 28.(a)** shows the particle size distribution of 316L and Cu powders accompanied by a SEM image of the powders. It is evident from **Fig. 28.(a)** that both powders exhibit a normal distribution of particle size, however, Cu powder distribution is positively skewed indicating the existence of more fine powders with average ECD of 14 μm compared to 28 μm for 316L.

Before samples can be processed, powders should be mixed at their prescribed mass fractions. Mixing of solids is not trivial, if powder granulometry, morphology, and homogeneity after mixing is of importance [208]. A detailed discussion of the mixing process can be found in Appendix B. Powder granulometry of the homogeneous mixtures is presented in **Fig. 28 .(b)**. Average ECD of mixtures are 23, 23, and 18 μm for mass fractions of 0.25, 0.50, and 0.75, respectively.

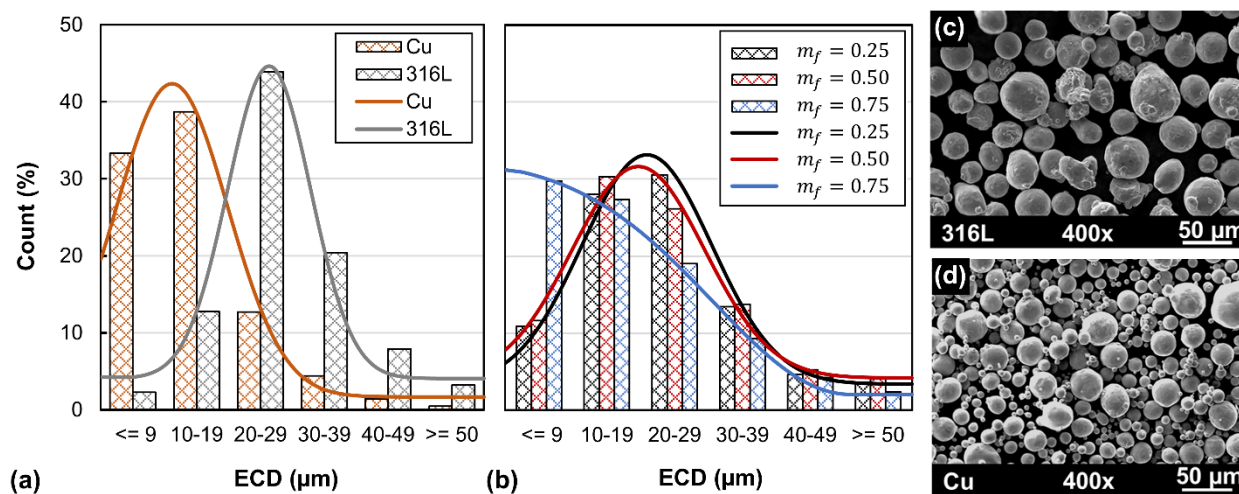


Fig. 28. (a) Particle size distribution of 316L and Cu powders. (b) Particle size distribution of 316L-Cu mixtures. (c) SEM image of 316L powder. (d) SEM image of Cu powder.

4.2.3. Additive manufacturing

Samples were manufactured using an EOS M290. The machine is equipped with a 400 W Ytterbium fiber laser and constant beam diameter of 100 μm . To rapidly manufacture and easily remove the samples from the build plate, hexagonal shaped samples with circumscribed circle diameter of 8 mm and height of 4 mm were chosen (**Fig. 27**). Samples were made on 2 mm support structures to prevent cross contamination with the 316L build plate. Three process parameters were chosen as variables in this study: laser power (P), laser speed (v), and laser hatch spacing (h). The combined effect of these variables can be captured in one term known as volumetric energy density (VED), which can be used to describe the amount of input energy per unit volume of the powder bed.

$$VED = \frac{P}{vht} \quad (13)$$

Where t is the nominal layer thickness that was kept constant at 20 μm . Samples were made using infill parameters only, meaning that other scanning strategies that are typically used for a part's top and bottom surfaces or contours were not applied to these samples. Stripe scanning strategy with 5 mm width was used at a rotation angle of 67°, and the build plate temperature was kept constant at 80° C. A high throughput design of experiment was used per mass fraction. Three levels were chosen for each process parameter at low, medium, and high based on the manufacturability of the samples which is dictated by EOS M290 machine limits. **Table 17** lists the process parameters and their levels for each mass fraction. It can be observed that the levels which were chosen for $m_{f_{Cu}} = 0.75$ result in lower VED values than those chosen for $m_{f_{Cu}} = 0.50$. This was done to simulate a scenario where a machine user would randomly assign the parameters without considering what parameter set might yield better results for a given composition. As long as the samples are manufacturable, the proposed methodology should provide accurate predictions regardless of the initial guess by the user.

The high throughput approach allowed for manufacturing of 27 samples per mass fraction in less than 5 hours. Certain combinations of levels can result in very large VED values that correspond to large melt pools. This has been associated with elevated edges that can cause failure due to recoater-part collision [209,210]. Samples with very high VEDs that caused collisions with the recoater were removed from the data set. The parameter sets of removed samples for $m_{f_{Cu}} = 0.25$ are [195 (W), 1300 (mm/s), 0.07 (mm)], and [280 (W), 1083 (mm/s), 0.09 (mm)]. For $m_{f_{Cu}} = 0.50$ the combinations of [370 (W), 800 (mm/s)], and [370 (W), 940 (mm/s)] for every hatch spacing were removed. Finally, for $m_{f_{Cu}} = 0.75$ the sample with the following parameter set was removed: [300 (W), 800 (mm/s), 0.07 (mm)].

Table 17. EOS M290 process parameters for 316L, copper, and compositions thereof used in high throughput design of experiment.

Material	Power (W)	Velocity (mm/s)	Hatch (mm)
316L	120	600	0.07
	195	1083	0.09
	280	1700	0.11
Cu	200	400	0.07
	300	800	0.09
	370	1200	0.11
316L-Cu ($m_{f_{Cu}} = 0.25$)	120	800	0.07
	195	1083	0.09
	280	1300	0.11
316L-Cu ($m_{f_{Cu}} = 0.50$)	195	400	0.07
	280	800	0.09
	370	1200	0.11
316L-Cu ($m_{f_{Cu}} = 0.75$)	195	800	0.07
	250	1083	0.09
	300	1200	0.11

4.2.4. Density measurements

Archimedes method was used to measure the density of the samples because it is shown to exhibit the highest accuracy ($\pm 0.08\%$ for high densities) and repeatability ($< \pm 0.1\%$) on all density levels compared to other means of density measurement [90]. After samples were removed from the build plate and before density measurement, they were ground to eliminate any remaining support structure from the bottom surface. Residual support structure can easily entrap air bubbles during submergence into a fluid and cause measurement errors. Samples were weighed while dry, and then weighed while suspended in Fluorinert™ FC-40 ($\rho = 1855 \text{ kg/m}^3$) to collect the data required for calculating density. Measurement uncertainty levels remained below 0.3% on average at 95% confidence interval for the entire data set.

4.2.5. Surface roughness

A focus variation optical microscope (Alicona, InfiniteFocus G4, Austria) was used to measure the areal surface roughness (S_a) and waviness (SW_a) of the as-built samples. The top surface of each sample was used for measurement as indicated by color in **Fig. 27**. Using a 10x objective, the acquisitions were carried out at 0.5 μm vertical and 5 μm lateral resolutions. The scanned area for 316L and Cu samples were $6 \times 1.2 \text{ mm}^2$ and $7 \times 1.5 \text{ mm}^2$, respectively. Although scanned areas are not equal, the number of data points collected per scan to carry out the calculations are well above the statistical requirements in both cases. Areal roughness and waviness profiles were separated using a Gaussian filter with a cut-off wavelength of 250 μm prior to calculations in accordance with ISO 25178 guidelines [140]. S_a is defined as the arithmetical mean height of the surface and SW_a is arithmetic mean waviness for the waviness profile.

4.3. Experimental Data Set

4.3.1. Density measurements

Effects of process parameters on part density of 316L and Cu are shown in **Fig. 29** as a function of VED. For 316L, density increased with an increase in VED to a maximum value of

7895 kg/m³, indicating a transition from lack of fusion region to fully dense region. It then slowly decreased as VED further increased to 333 J/mm³, indicating a transition into keyhole region. This observation is in agreement with previous experimental data in [23,146].

In the case of Cu, results followed three curves separated by the three levels of laser power with 200 W corresponding to the lowest set of data and 370 W to the highest. This indicates that laser power has a strong effect on density of Cu samples. This effect becomes less pronounced as higher VED values corresponding to higher laser powers are used and hatch spacing and layer thickness become more influential on part density [211,212]. High conductivity and reflectivity of pure copper makes it a challenging material for SLM process at low laser powers. It should be noted that high VED values do not have the same effect on density as moderate VED values with high laser powers [213]. These observations merit further study of the effects of individual process parameters on solidification and microstructure of pure copper processed via SLM. In this study, maximum relative density achieved for Cu samples was 97% at VED of 661 J/mm³ with corresponding laser power of 370 W.

Density results for three compositions of 316L-Cu are shown in **Fig. 29.(c)**. As expected, values were between 7000 and 8600 kg/m³, which is the range of values for the compositions' constituents. As mass fraction increased, overall density values also increased. Indicating that there is a significant difference in suitable process parameters required for the compositions compared to their constituents, i.e., 316L and Cu. However, since the chosen process variables did not cover a wide range of VED, patterns were more difficult to detect with an exception of $m_{f_{Cu}} = 0.50$ where density values remained relatively constant with an increase in VED. This observation highlights the need for a predictive tool, such as the machine learning algorithm proposed in this work, to estimate suitable process parameters without carrying out numerous experiments.

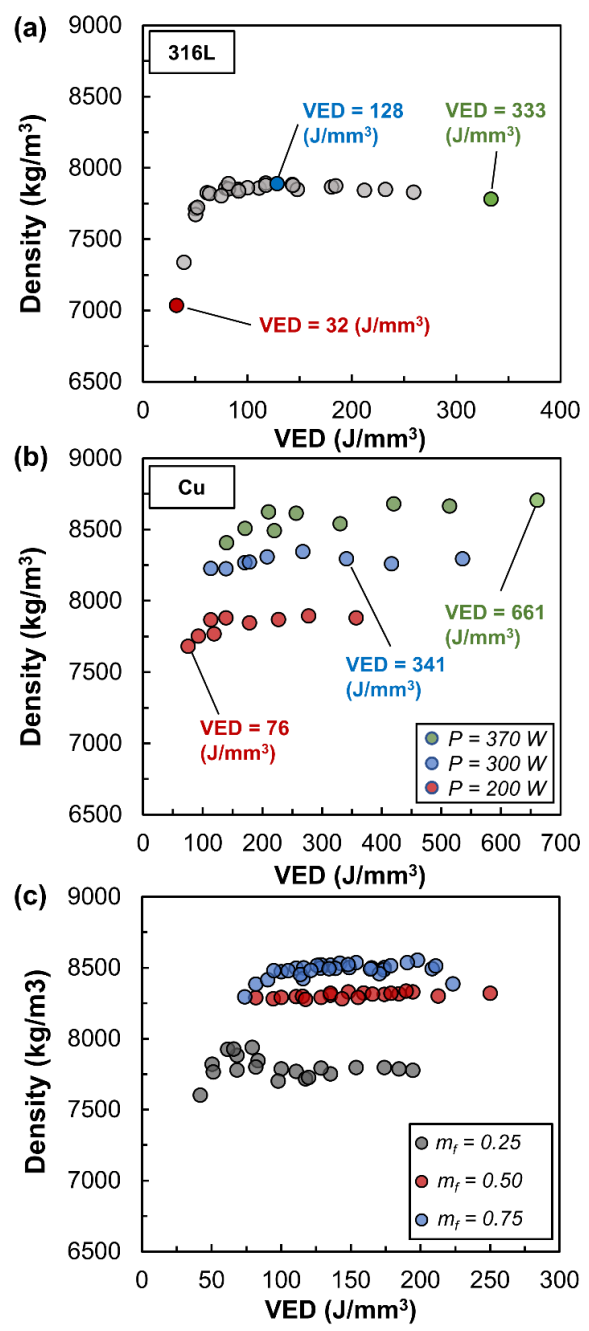


Fig. 29. Density as a function of volumetric energy density for (a) 316L, (b) Cu, and (c) 316L-Cu compositions.

4.3.2. Surface roughness

Effects of process parameters on surface roughness of samples are shown in **Fig. 30**. An interesting observation can be made by contrasting Sa against SWa. For both 316L and Cu, as VED increased, Sa decreased. In other words, surfaces became smoother with an increase in

input energy. This phenomenon is clearly depicted in supplementary figures **Fig. A3** and **Fig. A4** for 316L and Cu, respectively. This can be explained by formation of larger melt pools at higher VEDs that can redistribute the molten material across the surface due to surface tension which usually leads to a reduction in surface roughness [210,214]. However, as surfaces became smoother, their waviness increased. This phenomenon is more pronounced for 316L than Cu, mostly because melt pool size did not grow in Cu samples as much as 316L due to high thermal diffusivity and reflectivity of copper combined with insufficient laser power [215]. Larger melt pools can propagate waves across the surface. Rapid solidification, an inherent trait of SLM, causes these waves to solidify before they attenuate, resulting in an increase in surface waviness. The most severe case is observed for 316L at $VED = 333 \text{ J/mm}^3$, where the lowest roughness ($1.8 \text{ }\mu\text{m}$) resulted in the highest waviness ($172 \text{ }\mu\text{m}$). Edge effect is an additional contributing factor for this extreme case. As the large melt pool traveled close to the part's edge, surface tension forces created a feature with a large radius as shown in **Fig. A3**. Large waviness not only reduces geometrical accuracy, it can also result in failure due to recoater-part collision.

Similar behavior was observed for 316L-Cu compositions (**Fig. 31**). The same trend of decreasing S_a with increasing VED was observed for all compositions, with an accompanying increase in scatter of data. On the other hand, 316L appears to have influenced the waviness results more than Cu since a general increase in waviness with an increase in VED was observed. This implies that roughness as a metric of geometrical tolerance or printability should not be considered without waviness values. A tradeoff must be made when considering surface quality of AM parts. These initial observations warrant an in-depth investigation into the effects of process parameters on roughness and waviness of these samples which falls outside the scope of this work.

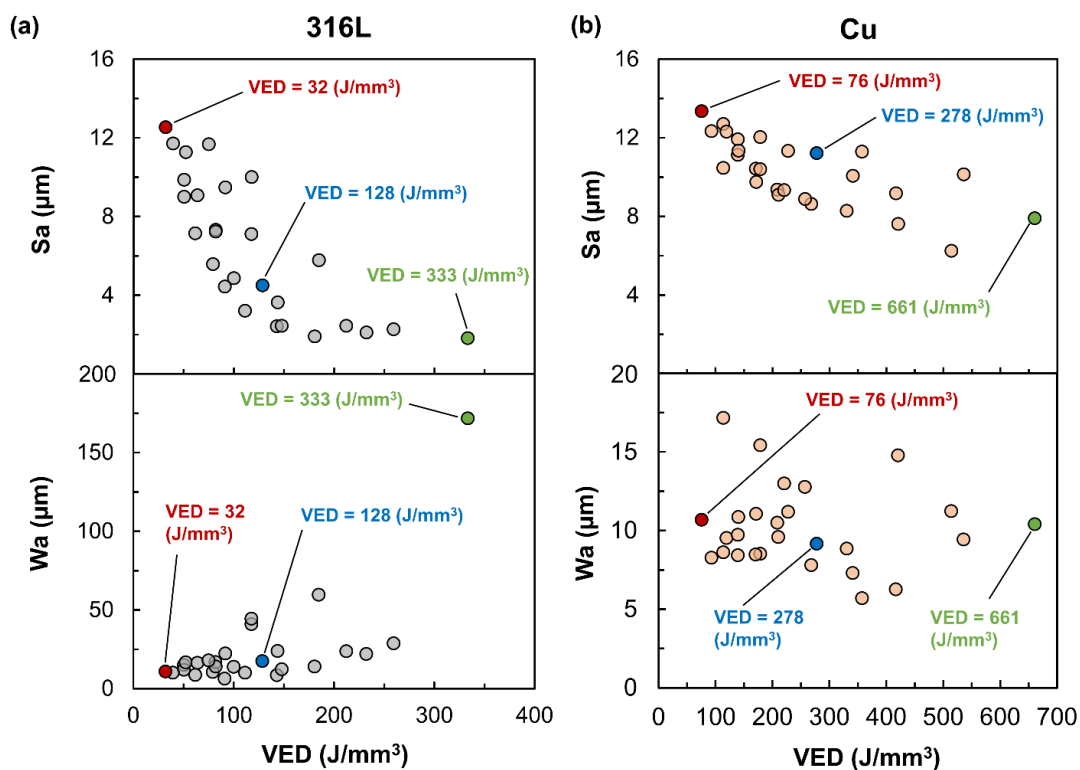


Fig. 30. Surface roughness and waviness as a function of VED for (a) 316L, and (b) Cu.

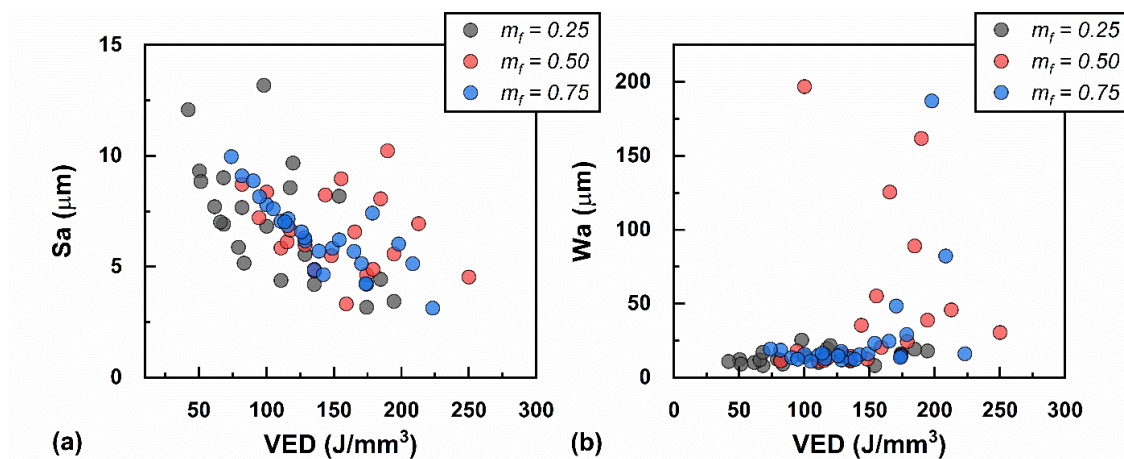


Fig. 31. (a) Surface roughness, and (b) waviness as a function of VED for 316L-Cu compositions.

4.4. Multi-variate Gaussian Process Framework

This section focuses on developing a statistical framework for modeling the properties of 316L, Cu, and their compositions, which facilitates transfer of knowledge among them. It should be noted that, hereafter, output means either of the material properties (i.e., surface roughness

and density) which is a function of process parameters (i.e., P , v , h). Modeling multiple outputs is a challenge since it requires computing cross-covariance among them. In this study, a convolution process is employed to build covariance functions between outputs. The premise is to build multiple Gaussian processes where all outputs $f_i(\mathbf{s})$ depend on some common latent process $X(\mathbf{s})$. The proposed framework can provide each output with both shared and unique features and allow commonalities between different outputs to be automatically inferred.

4.4.1. Modeling framework

In this study, it is assumed that measurements of either density or surface roughness as a function of process parameters for 316L, Cu, and 316L-Cu compositions are available *a priori*. Let $I = \{316L, Cu, 316L - Cu\}$. For each of the i th materials ($i \in I$), suppose the observed property values are denoted as $\mathbf{y}_i = \{y_i(\mathbf{s}_{i1}), \dots, y_i(\mathbf{s}_{ip_i})\}^T$ where p_i represents the number of observations for material i and $\{\mathbf{s}_{iq}, q = 1, \dots, p_i\} \in D \subset \mathcal{R}^\alpha$ represents a tuple of process parameters inputs for material i in a specific domain of interest D . The properties of each material in the defined a - D (a is the dimension of space) is modeled using the following decomposition:

$$y_i(\mathbf{s}) = f_i(\mathbf{s}) + \epsilon_i(\mathbf{s}), \quad i \in I \quad (14)$$

where, $f_i(\mathbf{s})$ represents a mean zero Gaussian process, and $\epsilon_i(\mathbf{s})$ represents measurement noise with zero mean and σ_ϵ^2 variance. Here $\mathbf{s} \in D \subset \mathcal{R}^\alpha$ represents a location over a bounded region D in a multi-dimensional parameter space. It should be noted that while the model development here is general, the case study is conducted considering $\alpha = 3$ corresponding to P , v , and h . The proposed method can incorporate multiple process parameters beyond the ones studied in this work.

The key principle of this model is to borrow information from the available, quick to sample data of 316L and Cu in order to make accurate predictions for their compositions. The aim is to combine process parameter observations from the 316L-Cu compositions with the data collected

from 316L and Cu separately. To achieve this transfer of knowledge from 316L and Cu data to their compositions, a shared representation of all material properties is defined as:

$$\mathbf{y}(\mathbf{s}) = \begin{pmatrix} y_{316L}(\mathbf{s}) \\ y_{Cu}(\mathbf{s}) \\ y_{316L-Cu}(\mathbf{s}) \end{pmatrix} = \begin{pmatrix} f_{316L}(\mathbf{s}) \\ f_{Cu}(\mathbf{s}) \\ f_{316L-Cu}(\mathbf{s}) \end{pmatrix} + \begin{pmatrix} \epsilon_{316L}(\mathbf{s}) \\ \epsilon_{Cu}(\mathbf{s}) \\ \epsilon_{316L-Cu}(\mathbf{s}) \end{pmatrix} = \mathbf{f}(\mathbf{s}) + \boldsymbol{\epsilon}(\mathbf{s}) \quad (15)$$

where the stochastic term $\mathbf{f}(\mathbf{s})$ is a mean zero multivariate Gaussian process with covariance $\text{cov}_{ij}^f(\mathbf{s}, \mathbf{s}') = \text{cov}_{ij}^f(f_i(\mathbf{s}), f_j(\mathbf{s}'))$ that characterizes the inherent variability and stochastic deviations in properties, both within and across different materials. The key feature provided by the expression in **Eq. (15)** is that the model uses every observation from training input (316L and Cu) and limited observations from 316L-Cu compositions to make predictions for the entire span of 316L-Cu properties. Based on **Eq. (15)**, prediction for the 316L-Cu compositions at any new input point (\mathbf{s}^*) is a weighted combination of all training data observations and the limited 316L-Cu composition property observations. This weighted combination is characterized by a flexible covariance function $\text{cov}_{ij}^f(f_i(\mathbf{s}), f_j(\mathbf{s}'))$ and an additive noise term $\epsilon(\mathbf{s})$.

As mentioned before, we resort to the convolution process to construct the covariance function. We consider 3 independent latent processes $\{X_m(\mathbf{s}): m \in I\}$, one for each material, and 5 different smoothing kernels $\{k_{m,i}(\mathbf{s}): m \in I, i \in I\}$ to share information between the target material (316L-Cu) properties and the materials in the training set, i.e., 316L and Cu. **Fig. 32** illustrates the proposed model structure where *stars* define kernel convolutions.

As shown in **Fig. 32**, the model structure is quite flexible. The structure allows $f_{316L-Cu}$ to possess unique properties encoded in $X_{316L-Cu}$ and $k_{316L-Cu,316L-Cu}$ and shared features with training materials are encoded in X_i and $k_{i,316L-Cu}, i = 316L, Cu$. In addition, it allows the information from the same latent function to be shared through different smoothing kernels ($k_{i,316L-Cu}$ vs. $k_{i,i}$). Thus, the target material function ($f_{316L-Cu}$) will have the ability to use practical knowledge from training observations through the different covariance parameters, resulting in an

output that can intrinsically possess both shared and independent features. Readers are referred to **Appendix C** for a more detailed explanation and mathematical derivation of the proposed covariance function.

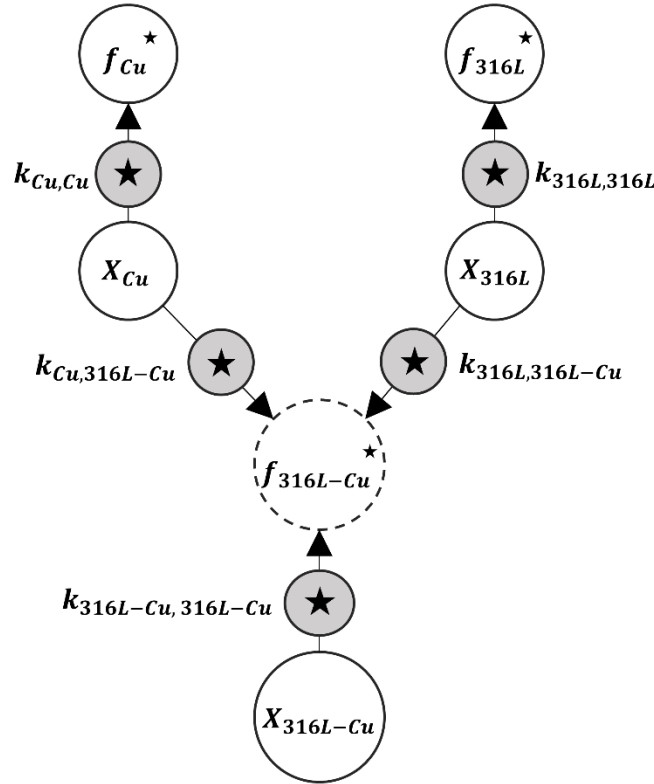


Fig. 32. Structure of the proposed multivariate Gaussian process algorithm.

Following the derivation in **Appendix C**, and based on the multivariate normal theory, the predictive distribution of $y_{316L-Cu}(\mathbf{s}^*)$ is expressed as:

$$y_{316L-Cu}(\mathbf{s}^*)|\mathbf{y} \sim N\left(\boldsymbol{\eta}^T \hat{\boldsymbol{\Omega}}_{p \times p}^{-1} \mathbf{y}, \text{cov}(\mathbf{s}^*, \mathbf{s}^*) + \hat{\sigma}_\varepsilon^2 - \hat{\boldsymbol{\eta}}^T_{316L-Cu}(\mathbf{s}^*) \hat{\boldsymbol{\Omega}}_{p \times p}^{-1} \hat{\boldsymbol{\eta}}_{316L-Cu}(\mathbf{s}^*)\right) \quad (16)$$

The predictive distribution as shown in **Eq. (16)** is based on the observations from all outputs. Thus, we can borrow strength from the previous observations of all outputs to make prediction for the material properties of 316L-Cu compositions. In other words, the model can interpolate across different outputs by weighting the effect of 316L and Cu on their compositions.

4.4.2. Cross validation

To validate the predictive capability of the model and to avoid overfitting, a common issue in supervised learning, a leave-one-out cross validation (LOO-CV) method was used [204]. Cross validation plots for density and surface roughness are depicted in **Fig. 33** and **Fig. 34**. These plots represent a comparison between the experimental density and roughness values at specific P , v , h combinations and their predicted values for the same P , v , h combinations. The closer the values are to the diagonal line, the more accurate the model predictions. However, a perfect fit would indicate overfitting of the training data [197]. To quantitatively assess the model's performance, mean absolute prediction error (MAPE) was calculated as the deviation from the diagonal line:

$$MAPE = \frac{1}{n} \sum_{i=1}^n |y_{i,o} - y_{i,p}| \quad (17)$$

where n is the number of data points used for cross validation, $y_{i,o}$ is the observed value for the data point i , and $y_{i,p}$ is the predicted value for the data point i . MAPE values are listed in **Table 18**. According to the results, the MAPE for density values were 1% on average for all three mass fractions. On the other hand, the MAPE for surface roughness values were 48% on average for all three mass fractions. This discrepancy can be explained by considering the training data for density and surface roughness shown in **Fig. 29**, **Fig. 30**, and **Fig. 31**. For density, there is a strong correlation with VED with minimal scatter in the data. In other words, the data set is ideal for training the algorithm. However, the scatter in surface roughness data, especially for Cu samples, is adversely affecting the algorithm's predictive capability. It should be noted that although the standard error of each prediction for surface roughness is large with respect to the measurement scale (14 μm), the averaged predictions are within acceptable distance from the diagonal line.

To further reduce the MAPE values, more training data from the 316L-Cu data set can be provided to the algorithm. Cross validation plots and corresponding MAPE values indicated that

the predicted values are in good agreement with the experiments.

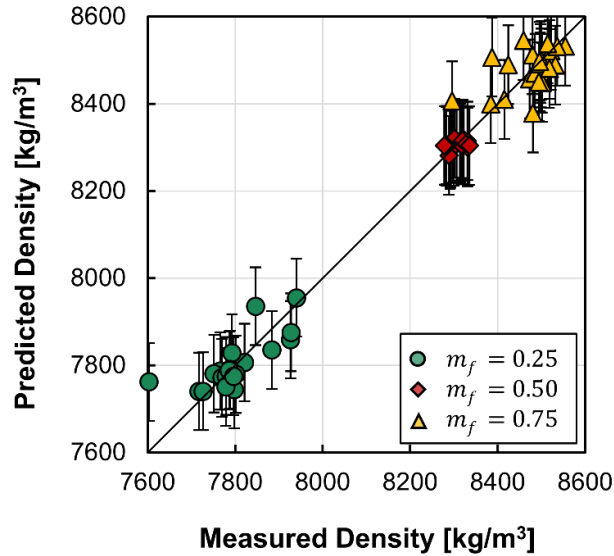


Fig. 33. Cross validation plot based on density data set for the proposed multivariate Gaussian process algorithm.

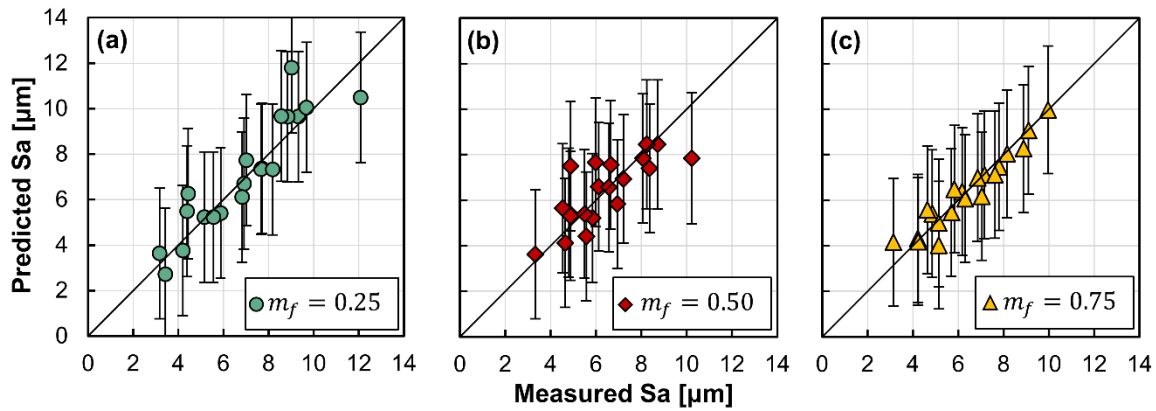


Fig. 34. Cross validation plot based on average surface roughness data set for the proposed multivariate Gaussian process algorithm.

Table 18. Mean absolute prediction error of density and surface roughness for all 316L-Cu compositions.

Mass fraction	Mean Absolute Prediction Error			
	Density (kg/m ³)	(%)	Surface roughness (μm)	(%)
0.25	89.2	1.1	2.9	47.2
0.50	90.0	1.0	2.8	47.8
0.75	90.4	1.1	2.8	47.7

4.5. Predictions

4.5.1. Process maps and analysis

After validity of the model was established, predictions for a wide range of process parameters were carried out. Test data was generated by equally dividing the entire range of P and v ($120 \leq P \leq 370$ W and $400 \leq v \leq 1700$ mm/s) used in the training data set by 100, and changing h by 0.01 mm increments from 0.07 to 0.11 mm. Overall, 3000 predictions for density and surface roughness were generated by the model. Predictions are shown in **Fig. 35**, **Fig. 36**, and **Fig. 37** in the form of process parameter maps for all three mass fractions. Since these process maps were generated using linear interpolation of triangulated data points, a large number of predictions were necessary to maintain the accuracy of the maps within the entire range of data sets without the need for performing any smoothing operations on contour lines.

A general look at different hatch spacings in the maps appeared to suggest no significant effect on predicted values of density and surface roughness within each mass fraction. However, **Fig. 38** shows a slight decrease in density means for $m_{f_{Cu}} = 0.25$, whereas $m_{f_{Cu}} = 0.50$ and $m_{f_{Cu}} = 0.75$ remained relatively constant. This indicates that effects of hatch spacing on density weakens as copper content within the part increases, whereas laser power and velocity remain the dominant process parameter in the overall VED. A comparison of means supports this argument. Tukey Honest Significant Difference (HSD) test results shown in **Fig. 39** revealed that changes in hatch spacing had significant effects on density and roughness levels of most samples at $m_{f_{Cu}} = 0.25$. There was no significant difference in means of Sa at $m_{f_{Cu}} = 0.50$ and density at $m_{f_{Cu}} = 0.75$. Significant differences for density mean at $m_{f_{Cu}} = 0.50$ and Sa means at $m_{f_{Cu}} = 0.75$ appeared only for 0.07-0.11 and 0.07-0.11, 0.08-0.11 pairs, respectively. In other words, results were insensitive to small changes in hatch spacing. *Post mortem* melt pool geometry data is required to determine critical values of hatch spacing with regard to density as reported in [71,146].

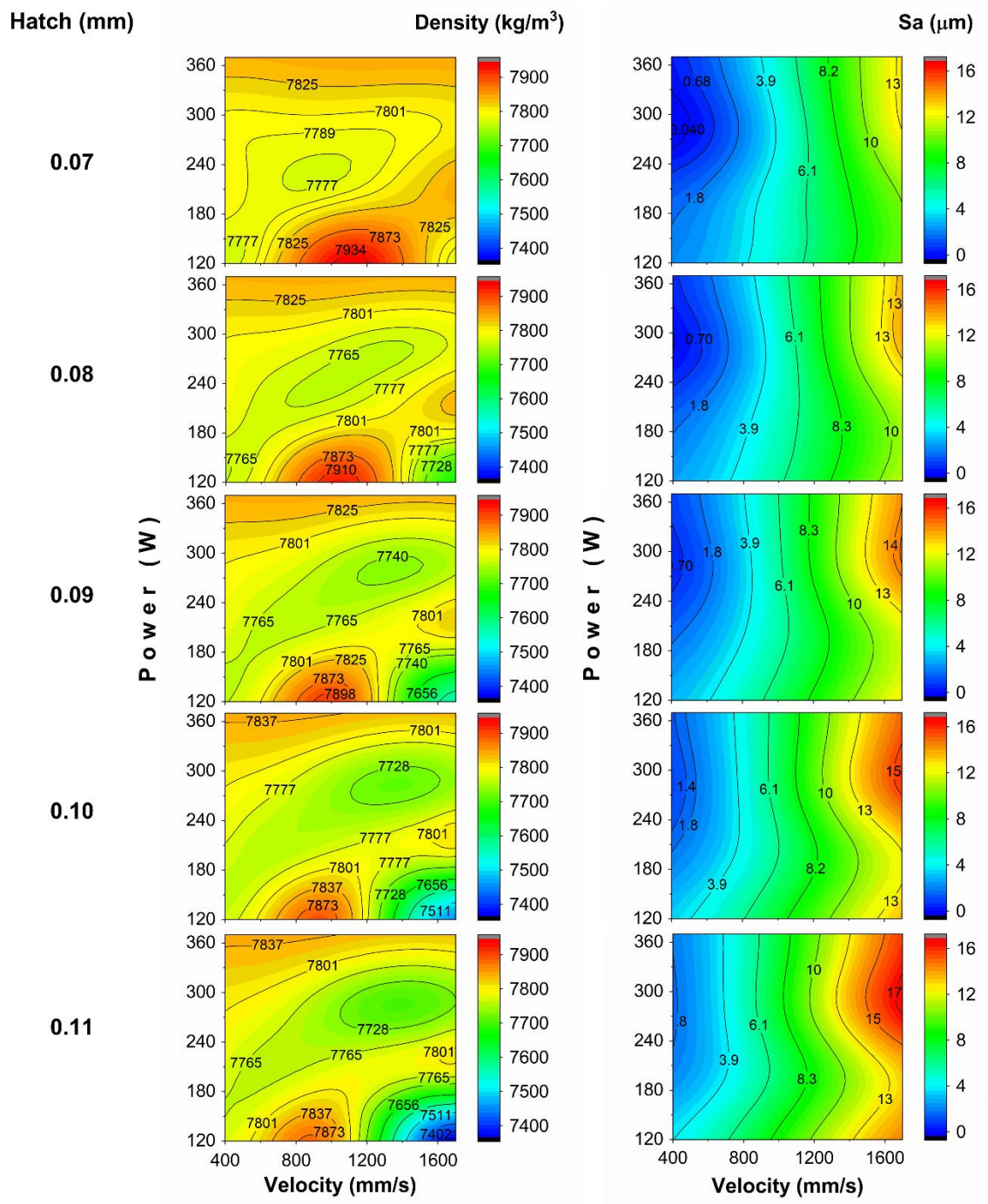


Fig. 35. Predicted process parameter maps for $m_{fCu} = 0.25$.

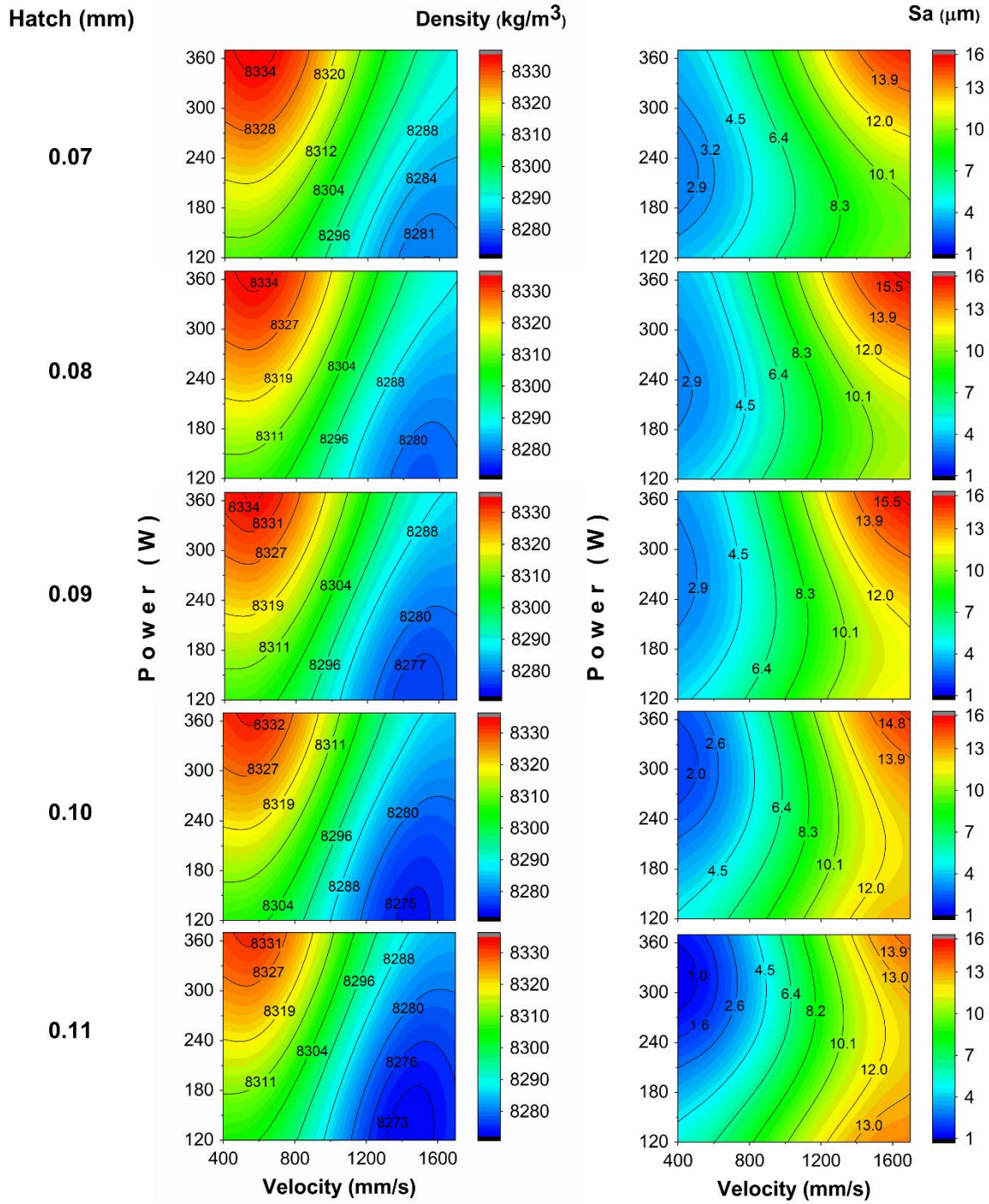


Fig. 36. Predicted process parameter maps for $m_{f_{cu}} = 0.50$.

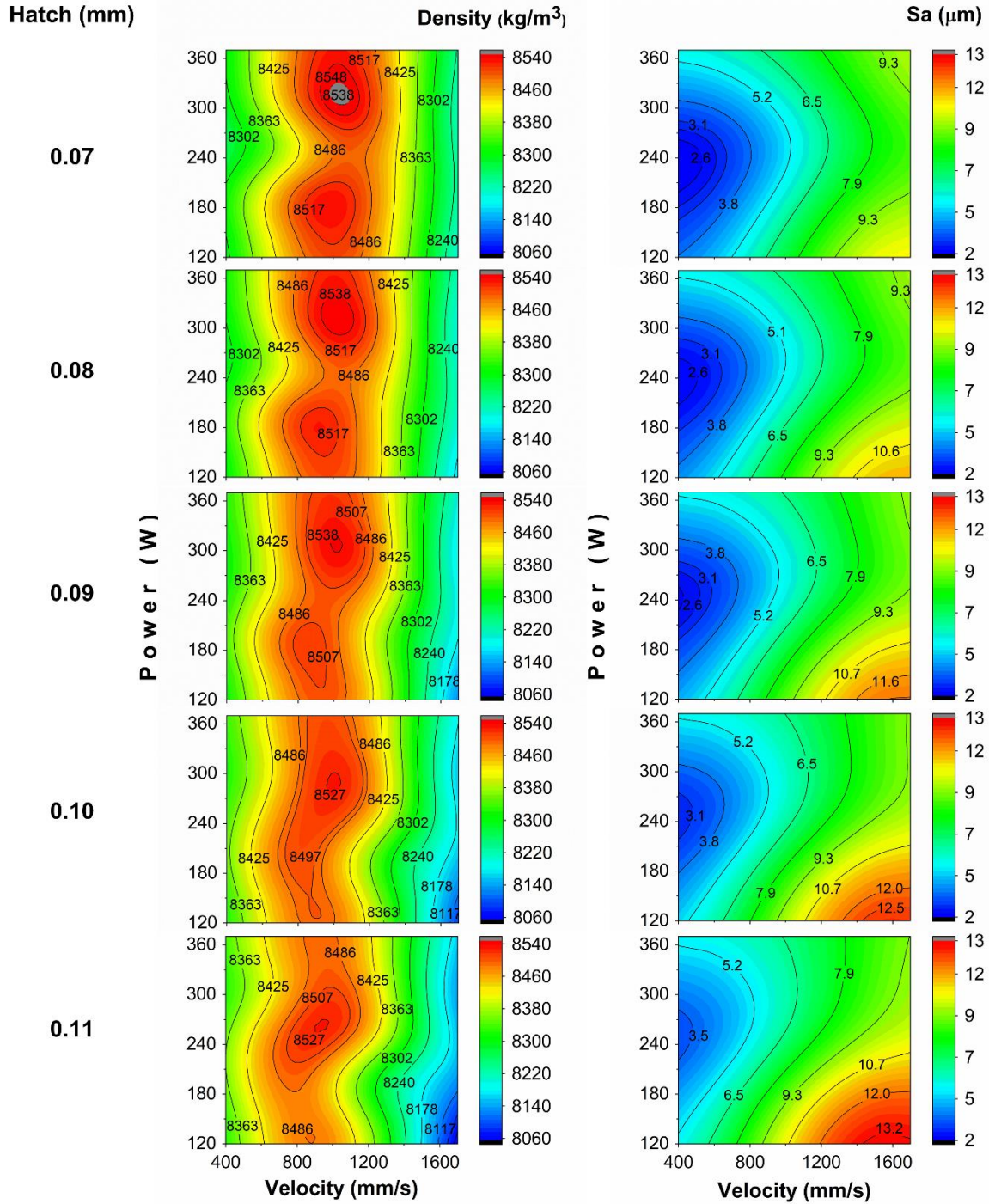


Fig. 37. Predicted process parameter maps for $m_{f_{cu}} = 0.75$.

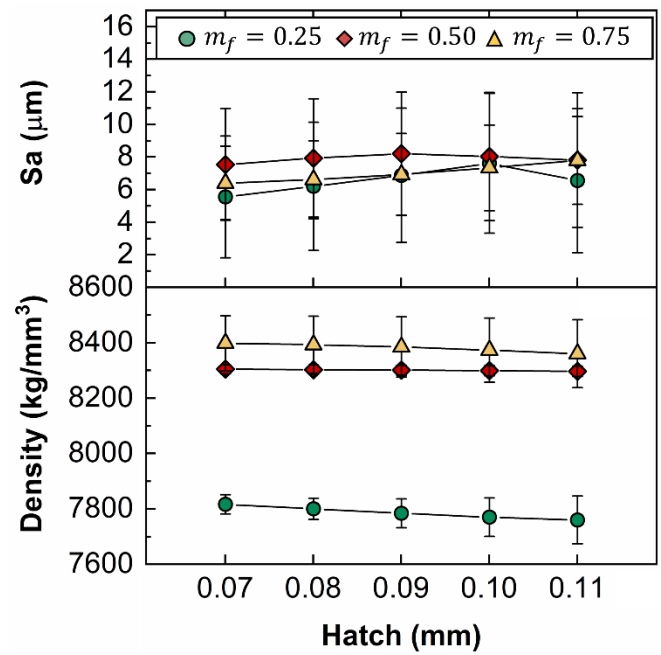


Fig. 38. Means of predicted values for density and surface roughness per hatch spacing.

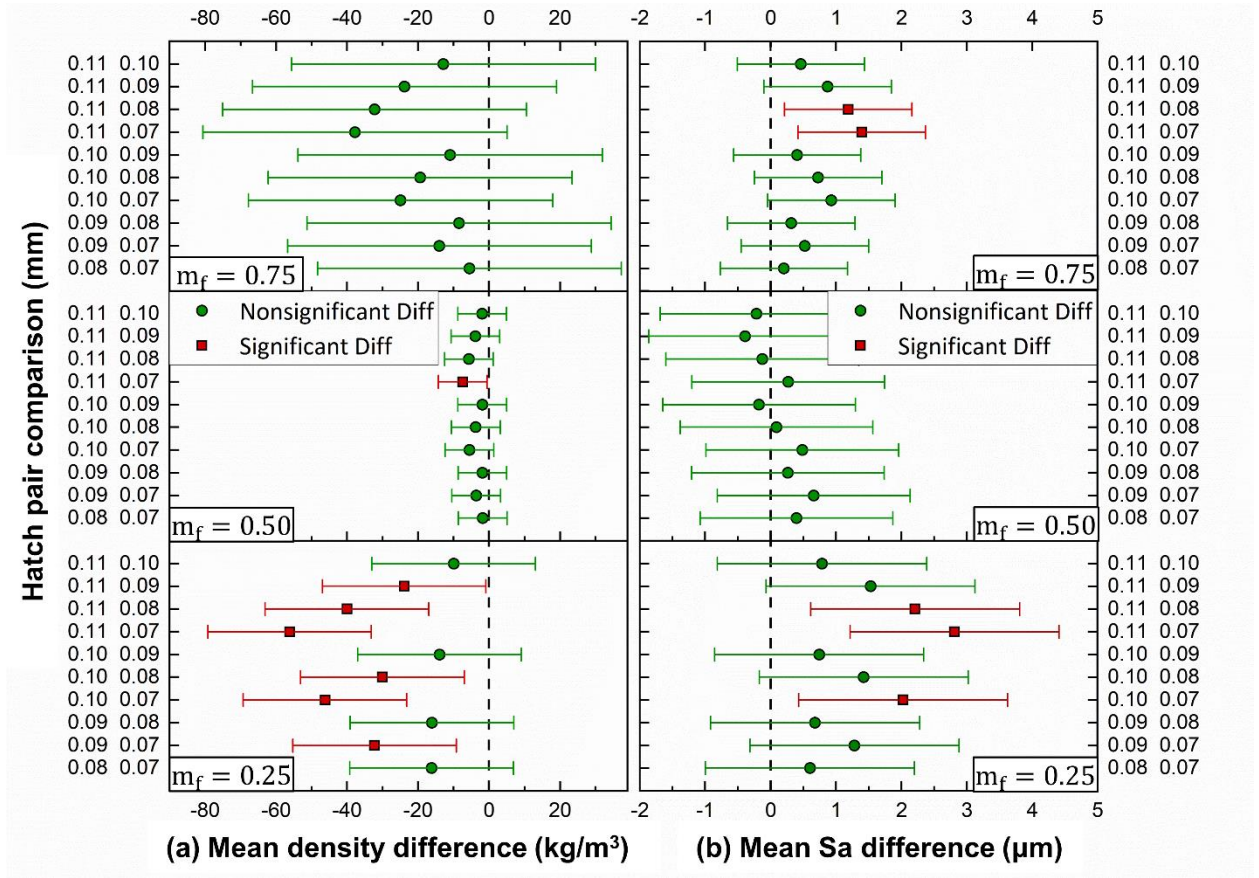


Fig. 39. Tukey HSD results for comparison of means of (a) density and (b) surface roughness.

After consideration of hatch spacing effects, a detailed look at the effects of power and velocity on surface roughness and density can be discussed for each mass fraction. Surface roughness results for $m_{f_{Cu}} = 0.25$ showed little sensitivity to changes in laser power. This sensitivity increased for $m_{f_{Cu}} = 0.50$ and $m_{f_{Cu}} = 0.75$. An increase in mass fraction means an increase in copper content within the part which corresponds to an increase of laser power influence on the properties including surface roughness. Laser velocity appeared to be the most influential parameter in surface roughness variations across mass fractions. High velocities correspond to high surface roughness levels at moderate and high laser powers for $m_{f_{Cu}} = 0.25$ and $m_{f_{Cu}} = 0.50$. This is due to elongated melt pools produced by high velocities. Elongated melt pools break up under Rayleigh instability to reduce surface tension during which balling occurs along the laser scan paths [216,217]. For $m_{f_{Cu}} = 0.75$, high velocity at low laser power corresponds to high surface roughness. This can also be attributed to balling effect. Low power and high velocity result in low VED which can be insufficient to form stable and large enough melt pools. This area also corresponds to low density regions, which further supports this argument. As a result, partially melted powder remains on the surface causing an increased surface roughness [216,217]. Balling is a major contributor to surface roughness in SLM [206]. Process maps also showed that the maximum surface roughness decreased from 16.9 μm to 13.4 μm as the copper content increased to $m_{f_{Cu}} = 0.75$. In addition to surface tension and viscosity differences that can change melt pool dynamics and the resulting surface roughness, this decrease can be attributed to the differences between average particle size of 316L and Cu. As shown in **Fig. 28**, and **Fig. B2**, ECD of mixture with $m_{f_{Cu}} = 0.25$ is 23 μm while ECD of mixture with $m_{f_{Cu}} = 0.75$ is 18 μm . Based on reported studies, SLM processing of powders with finer particle size results in smoother surfaces due to higher packing density which in turn can generate a stable and continuous melt pool and ultimately produce smoother surfaces [205,206]. This

highlights the significance of powder granulometry in process-parameter relationship of multi-material AM.

A closer look at results for $m_{f_{Cu}} = 0.50$ showed that high density regions correspond to low surface roughness regions. This correlation became stronger with an increase in hatch spacing. At first glance, one might be tempted to choose the process parameters corresponding to the highest density regions since they also yield acceptable surface roughness values. However, as discussed in section 3.2, a tradeoff must be made for roughness versus waviness. For $m_{f_{Cu}} = 0.50$, the process parameters that yield the highest density and lowest surface roughness levels can also lead to high waviness levels.

An observation can be made for density levels at $m_{f_{Cu}} = 0.75$ where two islands with high levels of density were formed, one at low laser power levels and the other at high laser power levels. The island at lower laser power levels started to disappear as hatch spacing increased to 0.11 mm. Moreover, these islands appeared at similar velocity values for each mass fraction, indicating that this phenomenon can be attributed to changes in laser power levels only. It should be noted that the high-density region at low laser powers is the same region where maximum density was achieved for $m_{f_{Cu}} = 0.25$, where the part is mostly made of 316L. Furthermore, it was shown in **Fig. 29** that part density of copper is mainly correlated to laser power levels and high laser powers correspond to higher part density. Since at $m_{f_{Cu}} = 0.75$ the part is mostly made of copper, it can be hypothesized that the high-density region at low laser powers is caused by the presence of un-melted copper powder particles within an otherwise fully dense 316L. The disappearance of the second island can be explained by considering the fact that with an increase in hatch spacing, the overall VED decreased to a level where 316L particles would partially melt and create lack of fusion porosity resulting in a decrease in overall density levels [71,218]. This behavior can be used in the future to manufacture metal composites with secondary material

inclusions for property enhancement of SLM parts. Future studies will look at the nature of the bonding at these conditions to verify these hypotheses.

4.5.2. Predicting multi-material process parameters

After discussing the predicted process maps at length, a set of suitable process parameters for grading 316L-Cu multi-material parts can be predicted. The predicted VED as a function of 316L-Cu composition is shown in **Fig. 40** followed by the corresponding power, velocity, and hatch values as well as estimated density and surface roughness values in **Table 19**. Process parameters for 316L were chosen according to the machine manufacturer's recommended settings, whereas the process parameters for Cu were chosen based on experimental data reported in section 3. The criterion for choosing the suitable process parameters for all three mass fractions were highest achievable density at average surface roughness values. According to **Fig. 39**, changes in hatch spacing resulted in significant changes in density for $m_{f_{Cu}} = 0.25$. Therefore, $h=0.07$ mm was chosen to achieve maximum density. However, at $m_{f_{Cu}} = 0.50$, the only significant change was observed between hatch spacing of 0.07 and 0.11 mm. In the SLM process, larger hatch spacing values for a given power and velocity results in faster manufacturing time. Therefore, for $m_{f_{Cu}} = 0.50$, predicted process parameters were chosen from the $h= 0.09$ mm map for a faster processing time. Finally, at $m_{f_{Cu}} = 0.75$, predicted values were chosen from $h=0.07$ mm for maximum density. The resulting VED graph shown in **Fig. 40** indicates that neither value of VED for 316L or Cu are suitable for grading a 316L-Cu multi-material part. Moreover, the relationship between VED and 316L-Cu compositions is nonlinear and nontrivial. This highlights the need for a predictive tool, such as the one presented in this work, for determination of suitable process parameters in multi-material AM using SLM.

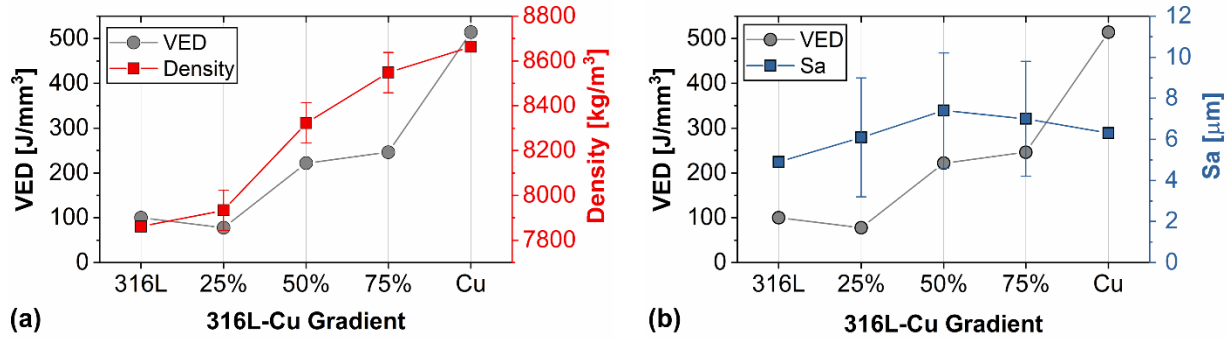


Fig. 40. Predicted VED values for 316L-Cu multi-material based on the best (a) density, and (b) surface roughness values. $m_{f_{Cu}}$ values are presented in percentages.

Table 19. Predicted parameters and their corresponding density and surface roughness for 316L-Cu multi-material part.

Composition	VED [J/mm³]	P [W]	v [mm/s]	h [mm]	Density [kg/m³]	Sa [μm]
316L	100	195	1083	0.09	7861	4.9
$m_{f_{Cu}} = 0.25$	78	120	1100	0.07	7934	6.1
$m_{f_{Cu}} = 0.50$	222	360	900	0.09	8323	7.4
$m_{f_{Cu}} = 0.75$	246	345	1000	0.07	8548	7.0
Cu	514	370	400	0.09	8664	6.3

As discussed in this section, it is evident that there are no unique solutions to choosing the suitable process parameters as a function of compositional gradient. There are multiple viable process parameter sets based on the importance to the user. Here, only density and surface roughness were chosen as criteria. Other properties such as yield strength or hardness can be added to the list of criteria depending on the application of the multi-material part. Moreover, the proposed model can include other process parameters like layer thickness and beam diameter in predictions making it increasingly more complicated to choose a single set of process parameters. Numerical techniques such as Pareto optimality solution can be used to automate the decision-making process and eliminate guesswork from the determination of suitable process parameters.

It should be noted that discretizing a continuous gradient into three separated zones neglects the melt pool interactions of each compositional gradients with the other. This assumption underlines the limitation of the proposed methodology. Commercial multi-material

SLM solutions will soon become available. Once a system is available that is capable of depositing variations of compositional gradients and apply different laser parameters as a function of the deposited gradient, the proposed methodology can be applied to many more mass fractions to represent the continuous gradient zone more accurately. This work is the first step in that direction.

4.6. Conclusions

For the first time, suitable process parameters for compositional grading of 316L-Cu multi-material were determined using machine learning and high throughput experimentation. Specifically, a multivariate Gaussian process model was developed to predict density and surface roughness of 316L-Cu parts along with the corresponding laser power, velocity and hatch spacing at different compositions. Process parameter maps for three different compositions were generated to provide firsthand knowledge of process-property relationship in a 316L-Cu multi-material part. The major findings of this study are as follows:

- The proposed multivariate Gaussian process model can accurately predict the process parameters of 316L-Cu parts with different compositions by transferring and sharing the information among the training data from 316L, Cu and 316L-Cu compositions. The averaged mean absolute prediction error for density and surface roughness are 1% and 47.6% respectively. Large scatter in surface roughness training data is the cause of larger prediction errors.
- Results revealed that process parameters within a gradient zone of a 316L-Cu multi-material part are a function of gradient composition. This relationship is nonlinear and nontrivial. Furthermore, results indicate that neither process parameter sets for 316L or Cu are suitable for grading a 316L-Cu multi-material part.
- Power and velocity are the most influential process parameters on part density and surface roughness of 316L-Cu compositions, both within and across mass fractions.

Hatch spacing effects were minimal, with $m_{f_{Cu}} = 0.25$ showing the most sensitivity towards its variation.

Other numerical methods such as pareto optimality solution can be applied to narrow down the number of viable process parameter sets and take the guess work out of the process. Further mechanical and metallurgical characterization work is also required to validate the recommended process parameters and support the formulated hypotheses resulted from this work. The underlying mechanisms behind the nonlinear relationship between process parameters and material composition, and the special case of $m_{f_{Cu}} = 0.25$, merits an in-depth study that will be the subject of future work. The overarching process parameter maps that were enabled by use of machine learning provided valuable insights into process-property relationship of 316L-Cu multi-material system for the first time. The discussions and results presented in this work will open new avenues of research in multi-material AM as this new manufacturing solution matures over the coming years.

References

- [1] I. Wohlers Associates, Wohlers report 2017 : 3D printing and additive manufacturing state of the industry : annual worldwide progress report., n.d. <https://wohlersassociates.com/2017report.htm> (accessed November 4, 2018).
- [2] C.L. Benson, G. Triulzi, C.L. Magee, Is There a Moore's Law for 3D Printing?, *3D Print. Addit. Manuf.* 5 (2018) 53–62. doi:10.1089/3dp.2017.0041.
- [3] T.T. Wohlers, I. (Specialist in three dimensional printing) Campbell, O. Diegel, J. Kowen, Wohlers report 2018 : 3D printing and additive manufacturing state of the industry : annual worldwide progress report., n.d.
- [4] J. Liu, A.T. Gaynor, S. Chen, Z. Kang, K. Suresh, A. Takezawa, L. Li, J. Kato, J. Tang, C.C.L. Wang, L. Cheng, X. Liang, A.C. To, Current and future trends in topology optimization for additive manufacturing, *Struct. Multidiscip. Optim.* 57 (2018) 2457–2483. doi:10.1007/s00158-018-1994-3.
- [5] A.T. Gaynor, J.K. Guest, Topology optimization considering overhang constraints: Eliminating sacrificial support material in additive manufacturing through design, *Struct. Multidiscip. Optim.* 54 (2016) 1157–1172. doi:10.1007/s00158-016-1551-x.
- [6] A.M. Mirzendehtdel, K. Suresh, Support structure constrained topology optimization for additive manufacturing, *Comput. Des.* 81 (2016) 1–13. doi:10.1016/J.CAD.2016.08.006.
- [7] X. Wang, S. Xu, S. Zhou, W. Xu, M. Leary, P. Choong, M. Qian, M. Brandt, Y.M. Xie, Topological design and additive manufacturing of porous metals for bone scaffolds and orthopaedic implants: A review, *Biomaterials.* 83 (2016) 127–141. doi:10.1016/J.BIOMATERIALS.2016.01.012.
- [8] A.M. Mirzendehtdel, B. Rankouhi, K. Suresh, Strength-based topology optimization for anisotropic parts, *Addit. Manuf.* 19 (2018) 104–113. doi:10.1016/j.addma.2017.11.007.
- [9] P. Zhang, J. Liu, A.C. To, Role of anisotropic properties on topology optimization of additive manufactured load bearing structures, *Scr. Mater.* 135 (2017) 148–152. doi:10.1016/J.SCRIPTAMAT.2016.10.021.
- [10] M. Seabra, J. Azevedo, A. Araújo, L. Reis, E. Pinto, N. Alves, R. Santos, J. Pedro Mortágua, Selective laser melting (SLM) and topology optimization for lighter aerospace componentes, *Procedia Struct. Integr.* 1 (2016) 289–296. doi:10.1016/J.PROSTR.2016.02.039.
- [11] S. Yoder, S. Morgan, C. Kinzy, E. Barnes, M. Kirka, V. Paquit, P. Nandwana, A. Plotkowski, R.R. Dehoff, S.S. Babu, Characterization of Topology Optimized Ti-6Al-4V Components using Electron Beam Powder Bed Fusion, *Addit. Manuf.* 19 (2017) 184–196. doi:10.1016/j.addma.2017.12.001.
- [12] M.E. Lynch, M. Mordasky, L. Cheng, A. To, Design, testing, and mechanical behavior of additively manufactured casing with optimized lattice structure, *Addit. Manuf.* 22 (2018) 462–471. doi:10.1016/J.ADDMA.2018.05.021.
- [13] B.H. Jared, M.A. Aguilo, L.L. Beghini, B.L. Boyce, B.W. Clark, A. Cook, B.J. Kaehr, J. Robbins, Additive manufacturing: Toward holistic design, *Scr. Mater.* 135 (2017) 141–147. doi:10.1016/J.SCRIPTAMAT.2017.02.029.
- [14] I. Gibson, D. Rosen, B. Stucker, *Additive Manufacturing Technologies*, Springer New York, New York, NY, 2015. doi:10.1007/978-1-4939-2113-3.
- [15] B.E. Carroll, R.A. Otis, J.P. Borgonia, J. Suh, R.P. Dillon, A.A. Shapiro, D.C. Hofmann, Z.-K. Liu, A.M. Beese, Functionally graded material of 304L stainless steel and inconel 625 fabricated by directed energy deposition: Characterization and thermodynamic modeling, *Acta Mater.* 108 (2016) 46–54. doi:10.1016/J.ACTAMAT.2016.02.019.
- [16] R.M. Mahamood, E.T. Akinlabi, Laser metal deposition of functionally graded Ti6Al4V/TiC, *Mater. Des.* 84 (2015) 402–410. doi:10.1016/J.MATDES.2015.06.135.

- [17] K. Shah, I. ul Haq, A. Khan, S.A. Shah, M. Khan, A.J. Pinkerton, Parametric study of development of Inconel-steel functionally graded materials by laser direct metal deposition, *Mater. Des.* 54 (2014) 531–538. doi:10.1016/J.MATDES.2013.08.079.
- [18] W. Li, S. Karnati, C. Kriewall, F. Liou, J. Newkirk, K.M. Brown Taminger, W.J. Seufzer, K.M.B. Taminger, W.J. Seufzer, K.M. Brown Taminger, W.J. Seufzer, Fabrication and Characterization of a Functionally Graded Material from Ti-6Al-4 V to SS316 by Laser Metal Deposition, *Addit. Manuf.* 14 (2017) 95–104. doi:10.1016/j.addma.2016.12.006.
- [19] A.M. Mirzendehtel, K. Suresh, A Pareto-Optimal Approach to Multimaterial Topology Optimization, *J. Mech. Des.* 137 (2015) 101701. doi:10.1115/1.4031088.
- [20] J.A. Cherry, H.M. Davies, S. Mehmood, N.P. Lavery, S.G.R.R. Brown, J. Sienz, Investigation into the effect of process parameters on microstructural and physical properties of 316L stainless steel parts by selective laser melting, 76 (n.d.) 869–879. doi:10.1007/s00170-014-6297-2.
- [21] A. Ahmadi, R. Mirzaeifar, N.S. Moghaddam, A.S. Turabi, H.E. Karaca, M. Elahinia, Effect of manufacturing parameters on mechanical properties of 316L stainless steel parts fabricated by selective laser melting: A computational framework, *Mater. Des.* 112 (2016) 328–338. doi:10.1016/J.MATDES.2016.09.043.
- [22] T. Kurzynowski, K. Gruber, W. Stopyra, B. Kuźnicka, E. Chlebus, Correlation between process parameters, microstructure and properties of 316 L stainless steel processed by selective laser melting, *Mater. Sci. Eng. A.* 718 (2018) 64–73. doi:10.1016/J.MSEA.2018.01.103.
- [23] E. Liverani, S. Toschi, L. Ceschini, A. Fortunato, Effect of selective laser melting (SLM) process parameters on microstructure and mechanical properties of 316L austenitic stainless steel, *J. Mater. Process. Technol.* 249 (2017) 255–263. <https://www.sciencedirect.com/science/article/pii/S0924013617302169> (accessed November 9, 2018).
- [24] Z. Sun, X. Tan, S. Tor, C.C.-N.A. Materials, undefined 2018, Simultaneously enhanced strength and ductility for 3D-printed stainless steel 316L by selective laser melting, *Nature.Com.* (n.d.). <https://www.nature.com/articles/s41427-018-0018-5> (accessed November 9, 2018).
- [25] J.J. Lewandowski, M. Seifi, Metal Additive Manufacturing: A Review of Mechanical Properties, *Annu. Rev. Mater. Res.* 46 (2016) 151–186. doi:10.1146/annurev-matsci-070115-032024.
- [26] M.F. Zaeh, G. Branner, Investigations on residual stresses and deformations in selective laser melting, *Prod. Eng.* 4 (2010) 35–45. doi:10.1007/s11740-009-0192-y.
- [27] P. Mercelis, J. Kruth, Residual stresses in selective laser sintering and selective laser melting, *Rapid Prototyp. J.* 12 (2006) 254–265. doi:10.1108/13552540610707013.
- [28] P. Guo, B. Zou, C. Huang, H. Gao, Journal of Materials Processing Technology Study on microstructure , mechanical properties and machinability of efficiently additive manufactured AISI 316L stainless steel by high-power direct laser deposition, Elsevier. 240 (2017) 12–22. doi:10.1016/J.JMATPROTEC.2016.09.005.
- [29] K. Zhang, S. Wang, W. Liu, X. Shang, Characterization of stainless steel parts by Laser Metal Deposition Shaping, *Mater. Des.* 55 (2014) 104–119. doi:10.1016/j.matdes.2013.09.006.
- [30] K. Ohnishi, T. Ohnishi, The Biological Effects of Space Radiation during Long Stays in Space, *Biol. Sci. Sp.* 18 (2004) 201–205. doi:10.2187/bss.18.201.
- [31] N. Shamsaei, A. Yadollahi, L. Bian, S.M. Thompson, An overview of Direct Laser Deposition for additive manufacturing; Part II: Mechanical behavior, process parameter optimization and control, *Addit. Manuf.* 8 (2015) 12–35. doi:10.1016/J.ADDMA.2015.07.002.
- [32] T. DebRoy, H.L. Wei, J.S. Zuback, T. Mukherjee, J.W. Elmer, J.O. Milewski, A.M. Beese,

- A. Wilson-Heid, A. De, W. Zhang, Additive manufacturing of metallic components – Process, structure and properties, *Prog. Mater. Sci.* 92 (2018) 112–224. doi:10.1016/J.PMATSCI.2017.10.001.
- [33] Y.M. Wang, T. Voisin, J.T. McKeown, J. Ye, N.P. Calta, Z. Li, Z. Zeng, Y. Zhang, W. Chen, T.T. Roehling, R.T. Ott, M.K. Santala, P.J.J. Depond, M.J. Matthews, A. V. Hamza, T. Zhu, Additively manufactured hierarchical stainless steels with high strength and ductility, *Nat. Mater.* 17 (2018) 63–70. doi:10.1038/NMAT5021.
- [34] M. Mukherjee, Effect of build geometry and orientation on microstructure and properties of additively manufactured 316L stainless steel by laser metal deposition, *Materialia*. 7 (2019) 100359. doi:10.1016/J.MTLA.2019.100359.
- [35] C.A. Bronkhorst, J.R. Mayeur, V. Livescu, R. Pokharel, D.W. Brown, G.T. Gray, Structural representation of additively manufactured 316L austenitic stainless steel, *Int. J. Plast.* 118 (2019) 70–86. doi:10.1016/J.IJPLAS.2019.01.012.
- [36] L. Liu, Q. Ding, Y. Zhong, J. Zou, J. Wu, Y.-L. Chiu, J. Li, Z. Zhang, Q. Yu, Z. Shen, Dislocation network in additive manufactured steel breaks strength–ductility trade-off, *Mater. Today*. 21 (2018) 354–361. doi:10.1016/J.MATTOD.2017.11.004.
- [37] T.R. Smith, J.D. Sugar, C. San Marchi, J.M. Schoenung, Strengthening mechanisms in directed energy deposited austenitic stainless steel, *Acta Mater.* 164 (2019) 728–740. doi:10.1016/J.ACTAMAT.2018.11.021.
- [38] M. Shamsujjoha, S.R. Agnew, J.M. Fitz-Gerald, W.R. Moore, T.A. Newman, High Strength and Ductility of Additively Manufactured 316L Stainless Steel Explained, *Metall. Mater. Trans. A*. 49 (2018) 3011–3027. doi:10.1007/s11661-018-4607-2.
- [39] M. Ma, Z. Wang, X. Zeng, A comparison on metallurgical behaviors of 316L stainless steel by selective laser melting and laser cladding deposition, *Mater. Sci. Eng. A*. 685 (2017) 265–273. doi:10.1016/J.MSEA.2016.12.112.
- [40] M. Ziętała, T. Durejko, M. Polański, I. Kunce, T. Płociński, W. Zieliński, M. Łazińska, W. Stępniewski, T. Czujko, K.J. Kurzydłowski, Z. Bojar, The microstructure, mechanical properties and corrosion resistance of 316 L stainless steel fabricated using laser engineered net shaping, *Mater. Sci. Eng. A*. 677 (2016) 1–10. doi:10.1016/J.MSEA.2016.09.028.
- [41] A. Yadollahi, N. Shamsaei, S.M. Thompson, D.W. Seely, Effects of process time interval and heat treatment on the mechanical and microstructural properties of direct laser deposited 316L stainless steel, *Mater. Sci. Eng. A*. 644 (2015) 171–183. doi:10.1016/J.MSEA.2015.07.056.
- [42] ASTM A276: Standard Specification for Stainless Steel Bars and Shapes, 2016. doi:10.1520/A0276.
- [43] K. Suresh, Efficient generation of large-scale pareto-optimal topologies, *Struct. Multidiscip. Optim.* 47 (2013) 49–61. doi:10.1007/s00158-012-0807-3.
- [44] A. Mirzendehtel, S. Krishnan, [manufacturer not identified], A hands-on introduction to topology optimization, n.d. <https://olin.tind.io/record/1588291> (accessed August 26, 2019).
- [45] EOS GmbH - Electro Optical Systems, Material data sheet - EOS StainlessSteel 316L, 2014. www.eos.info (accessed November 8, 2018).
- [46] J.D. Fritz, Heat Treating of Austenitic and Duplex Stainless Steels, *Heat Treat. Irons Steels*. 4D (2014) 0. doi:10.31399/asm.hb.v04d.a0005990.
- [47] Y. Liu, Y. Yang, D. Wang, A study on the residual stress during selective laser melting (SLM) of metallic powder, *Int. J. Adv. Manuf. Technol.* 87 (2016) 647–656. doi:10.1007/s00170-016-8466-y.
- [48] A. Koguchi, N. Kikuchi, A surface reconstruction algorithm for topology optimization, *Eng. Comput.* 22 (2006) 1–10. doi:10.1007/s00366-006-0023-0.
- [49] S. Liu, Q. Li, J. Liu, W. Chen, Y. Zhang, A Realization Method for Transforming a Topology Optimization Design into Additive Manufacturing Structures, *Engineering*. 4 (2018) 277–

285. doi:10.1016/J.ENG.2017.09.002.
- [50] A. Nana, J.-C. Cuillière, V. Francois, Automatic reconstruction of beam structures from 3D topology optimization results, *Comput. Struct.* 189 (2017) 62–82. doi:10.1016/J.COMPSTRUC.2017.04.018.
- [51] D. Brackett, I. Ashcroft, R. Hague, Topology optimization for additive manufacturing, *Sffsymposium.Engr.Utexas.Edu.* (n.d.). <https://sffsymposium.engr.utexas.edu/Manuscripts/2011/2011-27-Brackett.pdf> (accessed June 18, 2019).
- [52] K. Saeidi, L. Kevetkova, F. Lofaj, Z. Shen, Novel ferritic stainless steel formed by laser melting from duplex stainless steel powder with advanced mechanical properties and high ductility, *Mater. Sci. Eng. A.* 665 (2016) 59–65. doi:10.1016/J.MSEA.2016.04.027.
- [53] T.R. Smith, J.D. Sugar, J.M. Schoenung, C. San Marchi, Anomalous Annealing Response of Directed Energy Deposited Type 304L Austenitic Stainless Steel, *JOM.* 70 (2018) 358–363. doi:10.1007/s11837-017-2711-1.
- [54] D. Zhang, W. Niu, X. Cao, Z. Liu, Effect of standard heat treatment on the microstructure and mechanical properties of selective laser melting manufactured Inconel 718 superalloy, *Mater. Sci. Eng. A.* 644 (2015) 32–40. doi:10.1016/J.MSEA.2015.06.021.
- [55] M.P. Chae, W.M. Rozen, P.G. McMenamin, M.W. Findlay, R.T. Spychal, D.J. Hunter-Smith, Emerging Applications of Bedside 3D Printing in Plastic Surgery, *Front. Surg.* 2 (2015) 25. doi:10.3389/fsurg.2015.00025.
- [56] K. Saeidi, F. Akhtar, Subgrain-controlled grain growth in the laser-melted 316 L promoting strength at high temperatures, *R. Soc. Open Sci.* 5 (2018) 172394. doi:10.1098/rsos.172394.
- [57] D. Kong, C. Dong, X. Ni, L. Zhang, J. Yao, C. Man, X. Cheng, K. Xiao, X. Li, Mechanical properties and corrosion behavior of selective laser melted 316L stainless steel after different heat treatment processes, *J. Mater. Sci. Technol.* 35 (2019) 1499–1507. doi:10.1016/J.JMST.2019.03.003.
- [58] G. Meric de Bellefon, K.M.M. Bertsch, M.R.R. Chancey, Y.Q.Q. Wang, D.J.J. Thoma, Influence of solidification structures on radiation-induced swelling in an additively-manufactured austenitic stainless steel, *J. Nucl. Mater.* 523 (2019) 291–298. <https://www.sciencedirect.com/science/article/pii/S0022311519305343> (accessed July 8, 2019).
- [59] D.W. Brown, D.P. Adams, L. Balogh, J.S. Carpenter, B. Clausen, G. King, B. Reedlunn, T.A. Palmer, M.C. Maguire, S.C. Vogel, In Situ Neutron Diffraction Study of the Influence of Microstructure on the Mechanical Response of Additively Manufactured 304L Stainless Steel, *Metall. Mater. Trans. A.* 48 (2017) 6055–6069. doi:10.1007/s11661-017-4330-4.
- [60] R. Pokharel, L. Balogh, D.W. Brown, B. Clausen, G.T. Gray, V. Livescu, S.C. Vogel, S. Takajo, Signatures of the unique microstructure of additively manufactured steel observed via diffraction, *Scr. Mater.* 155 (2018) 16–20. doi:10.1016/J.SCRIPTAMAT.2018.06.008.
- [61] A. Röttger, K. Geenen, M. Windmann, F. Binner, W. Theisen, Comparison of microstructure and mechanical properties of 316 L austenitic steel processed by selective laser melting with hot-isostatic pressed and cast material, *Mater. Sci. Eng. A.* 678 (2016) 365–376. doi:10.1016/J.MSEA.2016.10.012.
- [62] T. Niendorf, S. Leuders, A. Riemer, H.A. Richard, T. Tröster, D. Schwarze, Highly Anisotropic Steel Processed by Selective Laser Melting, *Metall. Mater. Trans. B.* 44 (2013) 794–796. doi:10.1007/s11663-013-9875-z.
- [63] F. Yan, W. Xiong, E. Faierson, F. Yan, W. Xiong, E.J. Faierson, Grain Structure Control of Additively Manufactured Metallic Materials, *Materials (Basel).* 10 (2017) 1260. doi:10.3390/ma10111260.
- [64] G. Dieter, D. Bacon, Mechanical metallurgy, 1986. <http://www.academia.edu/download/30977829/3393.pdf> (accessed June 24, 2019).

- [65] N. Hansen, Hall–Petch relation and boundary strengthening, *Scr. Mater.* 51 (2004) 801–806. doi:10.1016/J.SCRIPTAMAT.2004.06.002.
- [66] J. Zowe, M. Kočvara, M.P. Bendsøe, Free material optimization via mathematical programming, *Math. Program.* 79 (1997) 445–466. doi:10.1007/BF02614328.
- [67] R. Jiang, R. Kleer, F.T. Piller, Predicting the future of additive manufacturing: A Delphi study on economic and societal implications of 3D printing for 2030, *Technol. Forecast. Soc. Change.* 117 (2017) 84–97. doi:10.1016/j.techfore.2017.01.006.
- [68] T.T. Wohlers, Wohlers report 2019: 3D printing and additive manufacturing state of the industry, Wohlers Associates, 2019.
- [69] H.D. Carlton, A. Haboub, G.F. Gallegos, D.Y. Parkinson, A.A. MacDowell, Damage evolution and failure mechanisms in additively manufactured stainless steel, *Mater. Sci. Eng. A.* 651 (2016) 406–414. doi:10.1016/j.msea.2015.10.073.
- [70] T. DebRoy, T. Mukherjee, J.O. Milewski, J.W. Elmer, B. Ribic, J.J. Blecher, W. Zhang, Scientific, technological and economic issues in metal printing and their solutions, n.d. doi:10.1038/s41563-019-0408-2.
- [71] M. Tang, P.C. Pistorius, J.L. Beuth, Prediction of lack-of-fusion porosity for powder bed fusion, *Addit. Manuf.* 14 (2017) 39–48. doi:10.1016/j.addma.2016.12.001.
- [72] R. Cunningham, C. Zhao, N. Parab, C. Kantzos, J. Pauza, K. Fezzaa, T. Sun, A.D. Rollett, Keyhole threshold and morphology in laser melting revealed by ultrahigh-speed x-ray imaging, *Science (80-.)*. 363 (2019) 849–852. doi:10.1126/science.aav4687.
- [73] N.D. Parab, C. Zhao, R. Cunningham, L.I. Escano, K. Fezzaa, W. Everhart, A.D. Rollett, L. Chen, T. Sun, Ultrafast X-ray imaging of laser–metal additive manufacturing processes, *J. Synchrotron Radiat.* 25 (2018) 1467–1477. doi:10.1107/S1600577518009554.
- [74] G. Tapia, S. Khairallah, M. Matthews, W.E. King, A. Elwany, Gaussian process-based surrogate modeling framework for process planning in laser powder-bed fusion additive manufacturing of 316L stainless steel, *Int. J. Adv. Manuf. Technol.* 94 (2018) 3591–3603. doi:10.1007/s00170-017-1045-z.
- [75] G. Tapia, A.H. Elwany, H. Sang, Prediction of porosity in metal-based additive manufacturing using spatial Gaussian process models, *Addit. Manuf.* 12 (2016) 282–290. doi:10.1016/j.addma.2016.05.009.
- [76] K. Aoyagi, H. Wang, H. Sudo, A. Chiba, Simple method to construct process maps for additive manufacturing using a support vector machine, *Addit. Manuf.* 27 (2019) 353–362. doi:10.1016/j.addma.2019.03.013.
- [77] M. Zlokarnik, *Dimensional analysis and scale-up in chemical engineering*. 1991, Springer-Verlag, Heidelb. (n.d.).
- [78] M. Van Elsen, F. Al-Bender, J.P. Kruth, Application of dimensional analysis to selective laser melting, *Rapid Prototyp. J.* 14 (2008) 15–22. doi:10.1108/13552540810841526.
- [79] Z. Wang, M. Liu, Dimensionless analysis on selective laser melting to predict porosity and track morphology, *J. Mater. Process. Technol.* 273 (2019) 116238. doi:10.1016/j.jmatprotec.2019.05.019.
- [80] T. Mukherjee, V. Manvatkar, A. De, T. DebRoy, Dimensionless numbers in additive manufacturing, *J. Appl. Phys.* 121 (2017) 064904. doi:10.1063/1.4976006.
- [81] A. Raghavan, H.L. Wei, T.A. Palmer, T. DebRoy, Heat transfer and fluid flow in additive manufacturing, *J. Laser Appl.* 25 (2013) 052006. doi:10.2351/1.4817788.
- [82] T. Mukherjee, T. DebRoy, Mitigation of lack of fusion defects in powder bed fusion additive manufacturing, *J. Manuf. Process.* 36 (2018) 442–449. doi:10.1016/j.jmapro.2018.10.028.
- [83] A.M. Rubenchik, W.E. King, S.S. Wu, Scaling laws for the additive manufacturing, *J. Mater. Process. Technol.* 257 (2018) 234–243. doi:10.1016/j.jmatprotec.2018.02.034.
- [84] E. Buckingham, On physically similar systems; Illustrations of the use of dimensional equations, *Phys. Rev.* 4 (1914) 345–376. doi:10.1103/PhysRev.4.345.
- [85] J. Pawlowski, *Die Ähnlichkeitstheorie in der physikalisch-technischen Forschung*:

- Grundlagen und Anwendung, 2013. https://books.google.com/books?hl=en&lr=&id=M6iBgAAQBAJ&oi=fnd&pg=PA1&dq=Pawlowski,+J.:+Die+Ahnlichkeitstheorie+in+der+physikalischtechnischen+Forschung+-+Grundlagen+und+Anwendungen+Springer-Verlag+Berlin-Heidelberg-New+York+1971&ots=5B3ntcmYjf&sig=mwhi9hv2HhFBECdGT_zrFnTnFN0 (accessed May 18, 2020).
- [86] J.J. Valencia, P.N. Quested, Thermophysical Properties, ASM Handb. Cast. 15 (2008) 468–481. doi:10.31399/asm.hb.v15.a0005240.
- [87] Aluminium for industrial 3D printing | EOS GmbH, (n.d.). <https://www.eos.info/en/additive-manufacturing/3d-printing-metal/dmls-metal-materials/aluminium-al> (accessed May 23, 2020).
- [88] J.G. Hust, D.H. Weitzel, R.L. Powell, Thermal Conductivity, Electrical Resistivity, and Thermopower of Aerospace Alloys from 4 to 300 K, JOURNAL Res. Natl. Bur. Stand. - A. Phys. Chem. 75 (1971) 269–277. https://nvlpubs.nist.gov/nistpubs/jres/75A/jresv75An4p269_A1b.pdf (accessed May 23, 2020).
- [89] E.O. Ezugwu, Z.M. Wang, Titanium alloys and their machinability - a review, J. Mater. Process. Technol. 68 (1997) 262–274. <https://www.sciencedirect.com/science/article/pii/S0924013696000301> (accessed May 23, 2020).
- [90] A.B. Spierings, M. Schneider, R. Eggenberger, Comparison of density measurement techniques for additive manufactured metallic parts, Rapid Prototyp. J. 17 (2011) 380–386. doi:10.1108/13552541111156504.
- [91] S.M.H. Hojjatzadeh, N.D. Parab, Q. Guo, M. Qu, L. Xiong, C. Zhao, L.I. Escano, K. Fezzaa, W. Everhart, T. Sun, L. Chen, Direct observation of pore formation mechanisms during LPBF additive manufacturing process and high energy density laser welding, Int. J. Mach. Tools Manuf. 153 (2020) 103555. doi:10.1016/j.ijmachtools.2020.103555.
- [92] C. Zhao, K. Fezzaa, R.W. Cunningham, H. Wen, F. De Carlo, L. Chen, A.D. Rollett, T. Sun, Real-time monitoring of laser powder bed fusion process using high-speed X-ray imaging and diffraction, Sci. Rep. 7 (2017) 1–11. doi:10.1038/s41598-017-03761-2.
- [93] S. Pal, G. Lojen, V. Kokol, I. Drstvensek, Evolution of metallurgical properties of Ti-6Al-4V alloy fabricated in different energy densities in the Selective Laser Melting technique, J. Manuf. Process. 35 (2018) 538–546. doi:10.1016/j.jmapro.2018.09.012.
- [94] N. Read, W. Wang, K. Essa, M.M. Attallah, Selective laser melting of AlSi10Mg alloy: Process optimisation and mechanical properties development, Mater. Des. 65 (2015) 417–424. doi:10.1016/j.matdes.2014.09.044.
- [95] V. Livescu, C.M. Knapp, G.T. Gray, R.M. Martinez, B.M. Morrow, B.G. Ndefru, Additively manufactured tantalum microstructures, Materialia. 1 (2018) 15–24. doi:10.1016/j.mtla.2018.06.007.
- [96] S. Wen, C. Wang, Y. Zhou, L. Duan, Q. Wei, S. Yang, Y. Shi, High-density tungsten fabricated by selective laser melting: Densification, microstructure, mechanical and thermal performance, Opt. Laser Technol. 116 (2019) 128–138. doi:10.1016/j.optlastec.2019.03.018.
- [97] J. Ye, S.A. Khairallah, A.M. Rubenchik, M.F. Crumb, G. Guss, J. Belak, M.J. Matthews, Energy Coupling Mechanisms and Scaling Behavior Associated with Laser Powder Bed Fusion Additive Manufacturing, Adv. Eng. Mater. 21 (2019) 1900185. doi:10.1002/adem.201900185.
- [98] S.L. Sing, S. Huang, G.D. Goh, G.L. Goh, C.F. Tey, J. H. K. Tan, W.Y. Yeong, Emerging Metallic Systems for Additive Manufacturing: In-situ Alloying and Multi-metal Processing in Laser Powder Bed Fusion, Prog. Mater. Sci. (2021) 100795. doi:10.1016/j.pmatsci.2021.100795.

- [99] C. Wei, L. Li, Recent progress and scientific challenges in multi-material additive manufacturing via laser-based powder bed fusion, *Virtual Phys. Prototyp.* (2021). doi:10.1080/17452759.2021.1928520.
- [100] D.R. Feenstra, R. Banerjee, H.L. Fraser, A. Huang, A. Molotnikov, N. Birbilis, Critical review of the state of the art in multi-material fabrication via directed energy deposition, *Curr. Opin. Solid State Mater. Sci.* 25 (2021) 100924. doi:10.1016/j.cossms.2021.100924.
- [101] B. Neirinck, X. Li, M. Hick, Powder Deposition Systems Used in Powder Bed-Based Multimetal Additive Manufacturing, *Accounts Mater. Res.* 2 (2021) 387–393. doi:10.1021/accountsmr.1c00030.
- [102] B. Rankouhi, S. Jahani, F.E. Pfefferkorn, D.J. Thoma, Compositional grading of a 316L-Cu multi-material part using machine learning for the determination of selective laser melting process parameters, *Addit. Manuf.* 38 (2021) 101836. doi:10.1016/j.addma.2021.101836.
- [103] Z.H. Liu, D.Q. Zhang, S.L. Sing, C.K. Chua, L.E. Loh, Interfacial characterization of SLM parts in multi-material processing: Metallurgical diffusion between 316L stainless steel and C18400 copper alloy, *Mater. Charact.* 94 (2014) 116–125. doi:10.1016/j.matchar.2014.05.001.
- [104] C. Wei, H. Gu, Q. Li, Z. Sun, Y. hui Chueh, Z. Liu, L. Li, Understanding of process and material behaviours in additive manufacturing of Invar36/Cu10Sn multiple material components via laser-based powder bed fusion, *Addit. Manuf.* 37 (2021) 101683. doi:10.1016/j.addma.2020.101683.
- [105] C. Tan, K. Zhou, W. Ma, L. Min, Interfacial characteristic and mechanical performance of maraging steel-copper functional bimetal produced by selective laser melting based hybrid manufacture, *Mater. Des.* 155 (2018) 77–85. doi:10.1016/j.matdes.2018.05.064.
- [106] J. Chen, Y. Yang, C. Song, M. Zhang, S. Wu, D. Wang, Interfacial microstructure and mechanical properties of 316L /CuSn10 multi-material bimetallic structure fabricated by selective laser melting, *Mater. Sci. Eng. A.* 752 (2019) 75–85. doi:10.1016/j.msea.2019.02.097.
- [107] C. Chen, D. Gu, D. Dai, L. Du, R. Wang, C. Ma, M. Xia, Laser additive manufacturing of layered TiB2/Ti6Al4V multi-material parts: Understanding thermal behavior evolution, *Opt. Laser Technol.* 119 (2019) 105666. doi:10.1016/j.optlastec.2019.105666.
- [108] S.L. Sing, L.P. Lam, D.Q. Zhang, Z.H. Liu, C.K. Chua, Interfacial characterization of SLM parts in multi-material processing: Intermetallic phase formation between AlSi10Mg and C18400 copper alloy, *Mater. Charact.* 107 (2015) 220–227. doi:10.1016/j.matchar.2015.07.007.
- [109] S. Shakerin, M. Sanjari, B.S. Amirkhiz, M. Mohammadi, Interface engineering of additively manufactured maraging steel-H13 bimetallic structures, *Mater. Charact.* 170 (2020) 110728. doi:10.1016/j.matchar.2020.110728.
- [110] S. Shakerin, A. Hadadzadeh, B.S. Amirkhiz, S. Shamsdini, J. Li, M. Mohammadi, Additive manufacturing of maraging steel-H13 bimetals using laser powder bed fusion technique, *Addit. Manuf.* 29 (2019) 100797. doi:10.1016/j.addma.2019.100797.
- [111] A. Hinojos, J. Mireles, A. Reichardt, P. Frigola, P. Hosemann, L.E. Murr, R.B. Wicker, Joining of Inconel 718 and 316 Stainless Steel using electron beam melting additive manufacturing technology, *Mater. Des.* 94 (2016) 17–27. doi:10.1016/j.matdes.2016.01.041.
- [112] D. Kotoban, A. Aramov, T. Tarasova, Possibility of multi-material laser cladding fabrication of nickel alloy and stainless steel, in: *Phys. Procedia*, Elsevier B.V., 2016: pp. 634–646. doi:10.1016/j.phpro.2016.08.066.
- [113] X. Mei, X. Wang, Y. Peng, H. Gu, G. Zhong, S. Yang, Interfacial characterization and mechanical properties of 316L stainless steel/inconel 718 manufactured by selective laser melting, *Mater. Sci. Eng. A.* 758 (2019) 185–191. doi:10.1016/j.msea.2019.05.011.
- [114] W.Y. Chen, X. Zhang, M. Li, R. Xu, C. Zhao, T. Sun, Laser powder bed fusion of Inconel

- 718 on 316 stainless steel, *Addit. Manuf.* 36 (2020) 101500. doi:10.1016/j.addma.2020.101500.
- [115] S. Mohd Yusuf, X. Zhao, S. Yang, N. Gao, Interfacial characterisation of multi-material 316L stainless steel/Inconel 718 fabricated by laser powder bed fusion, *Mater. Lett.* 284 (2021) 128928. doi:10.1016/j.matlet.2020.128928.
- [116] D. Kong, X. Ni, C. Dong, L. Zhang, J. Yao, C. Man, L. Wang, K. Xiao, X. Li, Anisotropic response in mechanical and corrosion properties of hastelloy X fabricated by selective laser melting, *Constr. Build. Mater.* 221 (2019) 720–729. doi:10.1016/j.conbuildmat.2019.06.132.
- [117] L.C. Olson, J.W. Ambrosek, K. Sridharan, M.H. Anderson, T.R. Allen, Materials corrosion in molten LiF-NaF-KF salt, *J. Fluor. Chem.* 130 (2009) 67–73. doi:10.1016/j.jfluchem.2008.05.008.
- [118] W.G. Kim, S.N. Yin, W.S. Ryu, J.H. Chang, S.J. Kim, Tension and creep design stresses of the “Hastelloy-X” alloy for high-temperature gas cooled reactors, *Mater. Sci. Eng. A.* 483–484 (2008) 495–497. doi:10.1016/j.msea.2006.12.184.
- [119] M.L. Montero-Sistiaga, Z. Liu, L. Bautmans, S. Nardone, G. Ji, J.P. Kruth, J. Van Humbeeck, K. Vanmeensel, Effect of temperature on the microstructure and tensile properties of micro-crack free hastelloy X produced by selective laser melting, *Addit. Manuf.* 31 (2020) 100995. doi:10.1016/j.addma.2019.100995.
- [120] N.J. Harrison, I. Todd, K. Mumtaz, Reduction of micro-cracking in nickel superalloys processed by Selective Laser Melting: A fundamental alloy design approach, *Acta Mater.* 94 (2015) 59–68. doi:10.1016/j.actamat.2015.04.035.
- [121] F. Wang, X.H. Wu, D. Clark, On direct laser deposited Hastelloy X: Dimension, surface finish, microstructure and mechanical properties, *Mater. Sci. Technol.* 27 (2011) 344–356. doi:10.1179/026708309X12578491814591.
- [122] F. Wang, Mechanical property study on rapid additive layer manufacture Hastelloy® X alloy by selective laser melting technology, *Int. J. Adv. Manuf. Technol.* 58 (2012) 545–551. doi:10.1007/s00170-011-3423-2.
- [123] D. Tomus, T. Jarvis, X. Wu, J. Mei, P. Rometsch, E. Hery, J.F. Rideau, S. Vaillant, Controlling the microstructure of Hastelloy-X components manufactured by Selective Laser Melting, in: *Phys. Procedia*, Elsevier B.V., 2013: pp. 823–827. doi:10.1016/j.phpro.2013.03.154.
- [124] H. Wang, L. Chen, B. Dovygytė, W. Xu, A. Sha, X. Li, H. Tang, Y. Liu, H. Wu, M.S. Pham, Micro-cracking, microstructure and mechanical properties of Hastelloy-X alloy printed by laser powder bed fusion: As-built, annealed and hot-isostatic pressed, *Addit. Manuf.* 39 (2021) 101853. doi:10.1016/j.addma.2021.101853.
- [125] M.L. Montero-Sistiaga, S. Pourbabak, J. Van Humbeeck, D. Schryvers, K. Vanmeensel, Microstructure and mechanical properties of Hastelloy X produced by HP-SLM (high power selective laser melting), *Mater. Des.* 165 (2019) 107598. doi:10.1016/j.matdes.2019.107598.
- [126] B. Rankouhi, K.M.M. Bertsch, G. Meric de Bellefon, M. Thevamaran, D.J.J. Thoma, K. Suresh, Experimental validation and microstructure characterization of topology optimized, additively manufactured SS316L components, *Mater. Sci. Eng. A.* 776 (2020) 139050. doi:10.1016/j.msea.2020.139050.
- [127] M. Mukherjee, Effect of build geometry and orientation on microstructure and properties of additively manufactured 316L stainless steel by laser metal deposition, *Materialia.* 7 (2019) 100359. doi:10.1016/j.mta.2019.100359.
- [128] B. Zhang, L. Dembinski, C. Coddet, The study of the laser parameters and environment variables effect on mechanical properties of high compact parts elaborated by selective laser melting 316L powder, *Mater. Sci. Eng. A.* 584 (2013) 21–31. doi:10.1016/j.msea.2013.06.055.

- [129] C.A. Bronkhorst, J.R. Mayeur, V. Livescu, R. Pokharel, D.W. Brown, G.T. Gray, Structural representation of additively manufactured 316L austenitic stainless steel, *Int. J. Plast.* 118 (2019) 70–86. doi:10.1016/j.ijplas.2019.01.012.
- [130] E. Liverani, S. Toschi, L. Ceschini, A. Fortunato, Effect of selective laser melting (SLM) process parameters on microstructure and mechanical properties of 316L austenitic stainless steel, *J. Mater. Process. Technol.* 249 (2017) 255–263. doi:10.1016/j.jmatprotec.2017.05.042.
- [131] K. Solberg, S. Guan, S.M.J. Razavi, T. Welo, K.C. Chan, F. Berto, Fatigue of additively manufactured 316L stainless steel: The influence of porosity and surface roughness, *Fatigue Fract. Eng. Mater. Struct.* 42 (2019) 2043–2052. doi:10.1111/ffe.13077.
- [132] J. Gockel, L. Sheridan, B. Koerper, B. Whip, The influence of additive manufacturing processing parameters on surface roughness and fatigue life, *Int. J. Fatigue.* 124 (2019) 380–388. doi:10.1016/j.ijfatigue.2019.03.025.
- [133] A. Yadollahi, M.J. Mahtabi, A. Khalili, H.R. Doude, J.C. Newman, Fatigue life prediction of additively manufactured material: Effects of surface roughness, defect size, and shape, *Fatigue Fract. Eng. Mater. Struct.* 41 (2018) 1602–1614. doi:10.1111/ffe.12799.
- [134] S.A. Khairallah, A.T. Anderson, A. Rubenchik, W.E. King, Laser powder-bed fusion additive manufacturing: Physics of complex melt flow and formation mechanisms of pores, spatter, and denudation zones, *Acta Mater.* 108 (2016) 36–45. doi:10.1016/j.actamat.2016.02.014.
- [135] K.C. Mills, R.F. Brooks, Measurements of thermophysical properties in high temperature melts, *Mater. Sci. Eng. A.* 178 (1994) 77–81. doi:10.1016/0921-5093(94)90522-3.
- [136] N.J. Harrison, I. Todd, K. Mumtaz, Thermal expansion coefficients in Invar processed by selective laser melting, *J. Mater. Sci.* 52 (2017) 10517–10525. doi:10.1007/s10853-017-1169-4.
- [137] K.C. Mills, Y.M. Youssef, Z. Li, Y. Su, Calculation of Thermophysical Properties of Ni-based Superalloys, *ISIJ Int.* 46 (2006) 623–632. doi:10.2355/ISIJINTERNATIONAL.46.623.
- [138] B. Rankouhi, A.K. Agrawal, F.E. Pfefferkorn, D.J. Thoma, A dimensionless number for predicting universal processing parameter boundaries in metal powder bed additive manufacturing, *Manuf. Lett.* 27 (2021) 13–17. doi:10.1016/j.mfglet.2020.12.002.
- [139] International Organization for Standardization, ISO 4287:1997. Geometrical product specifications (GPS). Surface texture: profile method. Terms, definitions and surface texture parameters, Geneva. (1997). <https://www.iso.org/obp/ui/#iso:std:iso:4287:ed-1:v1:en,fr> (accessed July 5, 2021).
- [140] ISO 25178-2:2012(en), Geometrical product specifications (GPS) — Surface texture: Areal — Part 2: Terms, definitions and surface texture parameters, 2012. <https://www.iso.org/obp/ui/#iso:std:iso:25178:-2:ed-1:v1:en> (accessed April 10, 2020).
- [141] S.T. Methods, Standard Test Methods for Bend Testing of Material for Ductility 1, *Current.* 03 (1998) 1–7.
- [142] A. Townsend, N. Senin, L. Blunt, R.K. Leach, J.S. Taylor, Surface texture metrology for metal additive manufacturing: a review, *Precis. Eng.* 46 (2016) 34–47. doi:10.1016/j.precisioneng.2016.06.001.
- [143] Q. Guo, C. Zhao, M. Qu, L. Xiong, S.M.H. Hojjatzadeh, L.I. Escano, N.D. Parab, K. Fezzaa, T. Sun, L. Chen, In-situ full-field mapping of melt flow dynamics in laser metal additive manufacturing, *Addit. Manuf.* 31 (2020) 100939. doi:10.1016/J.ADDMA.2019.100939.
- [144] G. Marchese, G. Basile, E. Bassini, A. Aversa, M. Lombardi, D. Ugues, P. Fino, S. Biamino, Study of the Microstructure and Cracking Mechanisms of Hastelloy X Produced by Laser Powder Bed Fusion, *Mater.* 2018, Vol. 11, Page 106. 11 (2018) 106. doi:10.3390/MA11010106.
- [145] O. Sanchez-Mata, X. Wang, J.A. Muñoz-Lerma, M.A. Shandiz, R. Gauvin, M. Brochu, Fabrication of Crack-Free Nickel-Based Superalloy Considered Non-Weldable during Laser Powder Bed Fusion, *Mater.* 2018, Vol. 11, Page 1288. 11 (2018) 1288.

- doi:10.3390/MA11081288.
- [146] A.K. Agrawal, G. Meric de Bellefon, D. Thoma, High-throughput experimentation for microstructural design in additively manufactured 316L stainless steel, *Mater. Sci. Eng. A.* 793 (2020) 139841. doi:10.1016/j.msea.2020.139841.
- [147] W.E. King, A.T. Anderson, R.M. Ferencz, N.E. Hodge, C. Kamath, S.A. Khairallah, A.M. Rubenchik, Laser powder bed fusion additive manufacturing of metals; physics, computational, and materials challenges, *Appl. Phys. Rev.* 2 (2015) 041304. doi:10.1063/1.4937809.
- [148] D. Wang, C. Song, Y. Yang, Y. Bai, Investigation of crystal growth mechanism during selective laser melting and mechanical property characterization of 316L stainless steel parts, *Mater. Des.* 100 (2016) 291–299. doi:10.1016/J.MATDES.2016.03.111.
- [149] J. Suryawanshi, K.G. Prashanth, U. Ramamurty, Mechanical behavior of selective laser melted 316L stainless steel, *Mater. Sci. Eng. A.* 696 (2017) 113–121. doi:10.1016/J.MSEA.2017.04.058.
- [150] L. Chen, B. Richter, X. Zhang, K.B. Bertsch, D.J. Thoma, F.E. Pfefferkorn, Effect of laser polishing on the microstructure and mechanical properties of stainless steel 316L fabricated by laser powder bed fusion, *Mater. Sci. Eng. A.* 802 (2021) 140579. doi:10.1016/j.msea.2020.140579.
- [151] M. Zhang, C.N. Sun, X. Zhang, J. Wei, D. Hardacre, H. Li, High cycle fatigue and ratcheting interaction of laser powder bed fusion stainless steel 316L: Fracture behaviour and stress-based modelling, *Int. J. Fatigue.* 121 (2019) 252–264. doi:10.1016/J.IJFATIGUE.2018.12.016.
- [152] J.E. Croll, G.R. Wallwork, The design of iron-chromium-nickel alloys for use at high temperatures, *Oxid. Met.* 1969 11. 1 (1969) 55–71. doi:10.1007/BF00609924.
- [153] F.P. Beer, E.R. Johnston, J.T. DeWolf, D.F. Mazurek, *Mechanics of materials*, 5th ed., McGraw Hill, 2009.
- [154] A. Bandyopadhyay, B. Heer, Additive manufacturing of multi-material structures, *Mater. Sci. Eng. R Reports.* 129 (2018) 1–16. doi:10.1016/j.mser.2018.04.001.
- [155] C. Zhang, F. Chen, Z. Huang, M. Jia, G. Chen, Y. Ye, Y. Lin, W. Liu, B. Chen, Q. Shen, L. Zhang, E.J. Lavernia, Additive manufacturing of functionally graded materials: A review, *Mater. Sci. Eng. A.* 764 (2019) 138209. doi:10.1016/j.msea.2019.138209.
- [156] G.H. Loh, E. Pei, D. Harrison, M.D. Monzón, An overview of functionally graded additive manufacturing, *Addit. Manuf.* 23 (2018) 34–44. doi:10.1016/j.addma.2018.06.023.
- [157] Aerosint Achieves Multi-Metal Powder Bed Fusion - 3DPrint.com | The Voice of 3D Printing / Additive Manufacturing, (n.d.). <https://3dprint.com/264346/aerosint-achieves-multi-metal-powder-bed-fusion/> (accessed August 24, 2020).
- [158] D. Li, I.Y. Kim, Multi-material topology optimization for practical lightweight design, *Struct. Multidiscip. Optim.* 58 (2018) 1081–1094. doi:10.1007/s00158-018-1953-z.
- [159] A. Reichardt, A.A. Shapiro, R. Otis, R.P. Dillon, J.P. Borgonia, B.W. McEnerney, P. Hosemann, A.M. Beese, Advances in additive manufacturing of metal-based functionally graded materials, *Int. Mater. Rev.* (2020). doi:10.1080/09506608.2019.1709354.
- [160] S. Matsusaka, M. Urakawa, H. Masuda, Micro-feeding of fine powders using a capillary tube with ultrasonic vibration, *Adv. Powder Technol.* 6 (1995) 283–293. doi:10.1016/S0921-8831(08)60518-X.
- [161] J. Pegna, S. Pattofatto, R. Berge, C. Bangalan, H. Herring, M. Lesaux, J. Engler, THE SAND-PAINTER: Two-dimensional powder deposition, in: *Solid Free. Fabr. Symp.*, 1999: pp. 695–709. <http://utw10945.utweb.utexas.edu/Manuscripts/1999/1999-081-Pegna.pdf> (accessed August 25, 2020).
- [162] T. Stichel, T. Laumer, T. Baumüller, P. Amend, S. Roth, Powder layer preparation using vibration-controlled capillary steel nozzles for additive manufacturing, in: *Phys. Procedia*, Elsevier B.V., 2014: pp. 157–166. doi:10.1016/j.phpro.2014.08.158.

- [163] S. Chianrabutra, B.G. Mellor, S. Yang, A Dry Powder Material Delivery Device for Multiple Material Additive Manufacturing, in: *Solid Free. Fabr. Symp.*, 2014. <http://utw10945.utweb.utexas.edu/sites/default/files/2014-005-Chianrabutra.pdf> (accessed August 25, 2020).
- [164] H. Wu, D. Pritchett, S. Wolff, J. Cao, K. Ehmann, P. Zou, A VIBRATION-ASSISTED POWDER DELIVERY SYSTEM FOR ADDITIVE MANUFACTURING - An experimental investigation -, *Addit. Manuf.* 34 (2020) 101170. doi:10.1016/j.addma.2020.101170.
- [165] M. Ott, M.F. Zaeh, Multi-Material Processing in Additive Manufacturing, in: *Utw10945.Utweb.Utexas.Edu*, 2010: pp. 195–203. <http://utw10945.utweb.utexas.edu/Manuscripts/2010/2010-18-Ott.pdf> (accessed August 25, 2020).
- [166] Y. Chivel, New approach to multi-material processing in selective laser melting, in: *Phys. Procedia*, Elsevier B.V., 2016: pp. 891–898. doi:10.1016/j.phpro.2016.08.093.
- [167] C. Wei, L. Li, X. Zhang, Y.H. Chueh, 3D printing of multiple metallic materials via modified selective laser melting, *CIRP Ann.* 67 (2018) 245–248. doi:10.1016/j.cirp.2018.04.096.
- [168] C. Wei, Z. Sun, Q. Chen, Z. Liu, L. Li, Additive Manufacturing of Horizontal and 3D Functionally Graded 316L/Cu10Sn Components via Multiple Material Selective Laser Melting, *J. Manuf. Sci. Eng. Trans. ASME.* 141 (2019). doi:10.1115/1.4043983.
- [169] X. Zhang, Y. hui Chueh, C. Wei, Z. Sun, J. Yan, L. Li, Additive manufacturing of three-dimensional metal-glass functionally gradient material components by laser powder bed fusion with in situ powder mixing, *Addit. Manuf.* 33 (2020) 101113. doi:10.1016/j.addma.2020.101113.
- [170] M.G. Scaramuccia, A.G. Demir, L. Caprio, O. Tassa, B. Previtali, Development of processing strategies for multigraded selective laser melting of Ti6Al4V and IN718, *Powder Technol.* 367 (2020) 376–389. doi:10.1016/j.powtec.2020.04.010.
- [171] J. Chen, Y. Yang, C. Song, D. Wang, S. Wu, M. Zhang, Influence mechanism of process parameters on the interfacial characterization of selective laser melting 316L/CuSn10, *Mater. Sci. Eng. A.* 792 (2020) 139316. doi:10.1016/j.msea.2020.139316.
- [172] Y. Bai, J. Zhang, C. Zhao, C. Li, H. Wang, Dual interfacial characterization and property in multi-material selective laser melting of 316L stainless steel and C52400 copper alloy, *Mater. Charact.* 167 (2020) 110489. doi:10.1016/j.matchar.2020.110489.
- [173] W. King, A.T. Anderson, R.M. Ferencz, N.E. Hodge, C. Kamath, S.A. Khairallah, Overview of modelling and simulation of metal powder bed fusion process at Lawrence Livermore National Laboratory, Taylor & Francis, 2015. doi:10.1179/1743284714Y.0000000728.
- [174] H.L. Wei, T. Mukherjee, W. Zhang, J.S. Zuback, G.L. Knapp, A. De, T. DebRoy, Mechanistic models for additive manufacturing of metallic components, *Prog. Mater. Sci.* (2020) 100703. doi:10.1016/j.pmatsci.2020.100703.
- [175] W. Yan, S. Lin, O.L. Kafka, Y. Lian, C. Yu, Z. Liu, J. Yan, S. Wolff, H. Wu, E. Ndip-Agbor, M. Mozaffar, K. Ehmann, J. Cao, G.J. Wagner, W.K. Liu, Data-driven multi-scale multi-physics models to derive process–structure–property relationships for additive manufacturing, *Comput. Mech.* 61 (2018) 521–541. doi:10.1007/s00466-018-1539-z.
- [176] D.R. Clymer, J. Cagan, J. Beuth, Power-velocity process design charts for powder bed additive manufacturing, *J. Mech. Des. Trans. ASME.* 139 (2017). doi:10.1115/1.4037302.
- [177] U. Scipioni Bertoli, A.J. Wolfer, M.J. Matthews, J.P.R. Delplanque, J.M. Schoenung, On the limitations of Volumetric Energy Density as a design parameter for Selective Laser Melting, *Mater. Des.* 113 (2017) 331–340. doi:10.1016/j.matdes.2016.10.037.
- [178] F. Imani, A. Gaikwad, M. Montazeri, P. Rao, H. Yang, E. Reutzel, Process mapping and in-process monitoring of porosity in laser powder bed fusion using layerwise optical imaging, *J. Manuf. Sci. Eng. Trans. ASME.* 140 (2018). doi:10.1115/1.4040615.
- [179] J.R. Hattrick-Simpers, J.M. Gregoire, A.G. Kusne, Perspective: Composition-structure-property mapping in high-throughput experiments: Turning data into knowledge, *APL*

- Mater. 4 (2016) 053211. doi:10.1063/1.4950995.
- [180] X.D. Xiang, X. Sun, G. Briceño, Y. Lou, K.A. Wang, H. Chang, W.G. Wallace-Freedman, S.W. Chen, P.G. Schultz, A combinatorial approach to materials discovery, *Science* (80-.). 268 (1995) 1738–1740. doi:10.1126/science.268.5218.1738.
- [181] W.H. Jandeleit, Jandeleit, Schaefer, Dieter J., Powers, Timothy S., Turner, Howard W., Weinberg, *Combinatorial materials science and catalysis*, *Angew. Chemie Int. Ed.* 38 (1999) 2494–2532. doi:https://doi.org/10.1002/(SICI)1521-3773(19990903)38:17<2494::AID-ANIE2494>3.0.CO;2-%23.
- [182] W.F. Maier, K. Stowe, S. Sieg, *Combinatorial and high-throughput materials science*, *Angew. Chemie - Int. Ed.* 46 (2007) 6016–6067. doi:10.1002/anie.200603675.
- [183] M.L. Green, I. Takeuchi, J.R. Hattrick-Simpers, *Applications of high throughput (combinatorial) methodologies to electronic, magnetic, optical, and energy-related materials*, *J. Appl. Phys.* 113 (2013) 231101. doi:10.1063/1.4803530.
- [184] J.N. Cawse, *Experimental Design for Combinatorial and High Throughput Materials Development*, GE Global Research, 2002. <https://analyticalscience.wiley.com/do/10.1002/sepspec.9780471203438> (accessed September 12, 2020).
- [185] *About the Materials Genome Initiative | The White House*, (n.d.). <https://obamawhitehouse.archives.gov/mgi> (accessed September 12, 2020).
- [186] M.L. Green, C.L. Choi, J.R. Hattrick-Simpers, A.M. Joshi, I. Takeuchi, S.C. Barron, E. Campo, T. Chiang, S. Empedocles, J.M. Gregoire, A.G. Kusne, J. Martin, A. Mehta, K. Persson, Z. Trautt, J. Van Duren, A. Zakutayev, *Fulfilling the promise of the materials genome initiative with high-throughput experimental methodologies*, *Appl. Phys. Rev.* 4 (2017) 011105. doi:10.1063/1.4977487.
- [187] J.C. Zhao, *High-throughput experimental tools for the materials genome initiative*, *Chinese Sci. Bull.* 59 (2014) 1652–1661. doi:10.1007/s11434-014-0120-1.
- [188] A. Jain, S.P. Ong, G. Hautier, W. Chen, W.D. Richards, S. Dacek, S. Cholia, D. Gunter, D. Skinner, G. Ceder, K.A. Persson, *Commentary: The materials project: A materials genome approach to accelerating materials innovation*, *APL Mater.* 1 (2013) 011002. doi:10.1063/1.4812323.
- [189] R. Liu, A. Kumar, Z. Chen, A. Agrawal, V. Sundararaghavan, A. Choudhary, *A predictive machine learning approach for microstructure optimization and materials design*, *Sci. Rep.* 5 (2015) 1–12. doi:10.1038/srep11551.
- [190] F. Ren, L. Ward, T. Williams, K.J. Laws, C. Wolverton, J. Hattrick-Simpers, A. Mehta, *Accelerated discovery of metallic glasses through iteration of machine learning and high-throughput experiments*, *Sci. Adv.* 4 (2018) eaaq1566. doi:10.1126/sciadv.aaq1566.
- [191] R. Ramprasad, R. Batra, G. Pilania, A. Mannodi-Kanakkithodi, C. Kim, *Machine learning in materials informatics: Recent applications and prospects*, *Npj Comput. Mater.* 3 (2017) 54. doi:10.1038/s41524-017-0056-5.
- [192] S.S. Razvi, S. Feng, A. Narayanan, Y.T.T. Lee, P. Witherell, *A review of machine learning applications in additive manufacturing*, in: *Proc. ASME Des. Eng. Tech. Conf.*, American Society of Mechanical Engineers (ASME), 2019. doi:10.1115/DETC2019-98415.
- [193] C. Silbernagel, A. Aremu, I. Ashcroft, *Using machine learning to aid in the parameter optimisation process for metal-based additive manufacturing*, *Rapid Prototyp. J.* 26 (2019) 625–637. doi:10.1108/RPJ-08-2019-0213.
- [194] M. Mozaffar, A. Paul, R. Al-Bahrani, S. Wolff, A. Choudhary, A. Agrawal, K. Ehmann, J. Cao, *Data-driven prediction of the high-dimensional thermal history in directed energy deposition processes via recurrent neural networks*, *Manuf. Lett.* 18 (2018) 35–39. doi:10.1016/j.mfglet.2018.10.002.
- [195] L. Scime, D. Siddel, S. Baird, V. Paquit, *Layer-wise anomaly detection and classification for powder bed additive manufacturing processes: A machine-agnostic algorithm for real-*

- time pixel-wise semantic segmentation, *Addit. Manuf.* 36 (2020) 101453. doi:10.1016/j.addma.2020.101453.
- [196] G.D. Goh, S.L. Sing, W.Y. Yeong, A review on machine learning in 3D printing: applications, potential, and challenges, *Artif. Intell. Rev.* (2020) 1–32. doi:10.1007/s10462-020-09876-9.
- [197] L. Meng, B. McWilliams, W. Jarosinski, H.Y. Park, Y.G. Jung, J. Lee, J. Zhang, Machine Learning in Additive Manufacturing: A Review, *JOM.* 72 (2020) 2363–2377. doi:10.1007/s11837-020-04155-y.
- [198] A. Fathi, A. Mozaffari, A. Fathi, A. Mozaffari, Vector optimization of laser solid freeform fabrication system using a hierarchical mutable smart bee-fuzzy inference system and hybrid NSGA-II/self-organizing map, *J Intell Manuf.* 25 (2014) 775–795. doi:10.1007/s10845-012-0718-6.
- [199] Z. Yang, D. Eddy, S. Krishnamurty, I. Grosse, P. Denno, P.W. Witherell, F. Lopez, Dynamic metamodeling for predictive analytics in advanced manufacturing, *Smart Sustain. Manuf. Syst.* 2 (2018) 18–39. doi:10.1520/SSMS20170013.
- [200] B. Kappes, S. Moorthy, D. Drake, H. Geerlings, A. Stebner, Machine learning to optimize additive manufacturing parameters for laser powder bed fusion of Inconel 718, in: *Miner. Met. Mater. Ser.*, Springer International Publishing, 2018: pp. 595–627. doi:10.1007/978-3-319-89480-5_39.
- [201] A. Garg, K. Tai, An ensemble approach of machine learning in evaluation of mechanical property of the rapid prototyping fabricated prototype, in: *Appl. Mech. Mater.*, 2014: pp. 493–496. doi:10.4028/www.scientific.net/AMM.575.493.
- [202] Z. Yang, D. Eddy, S. Krishnamurty, I. Grosse, Y. Lu, A Super-Metamodeling Framework to Optimize System Predictability, in: *ASME International*, 2018. doi:10.1115/detc2018-86055.
- [203] L. Meng, J. Zhang, Process Design of Laser Powder Bed Fusion of Stainless Steel Using a Gaussian Process-Based Machine Learning Model, *JOM.* 72 (2020) 420–428. doi:10.1007/s11837-019-03792-2.
- [204] C.E. Rasmussen, Gaussian Processes in machine learning, *Lect. Notes Comput. Sci.* (Including Subser. Lect. Notes Artif. Intell. Lect. Notes Bioinformatics). 3176 (2004) 63–71. doi:10.1007/978-3-540-28650-9_4.
- [205] A.B. Spierings, N. Herres, G. Levy, Influence of the particle size distribution on surface quality and mechanical properties in AM steel parts, *Rapid Prototyp. J.* 17 (2011) 195–202. doi:10.1108/13552541111124770.
- [206] J.H. Tan, W.L.E. Wong, K.W. Dalgarno, An overview of powder granulometry on feedstock and part performance in the selective laser melting process, *Addit. Manuf.* 18 (2017) 228–255. doi:10.1016/j.addma.2017.10.011.
- [207] ASTM F1877-16, Standard Practice for Characterization of Particles, West Conshohocken, PA, 2016. doi:10.1520/F1877-16.
- [208] R. Weinekötter, H. Gericke, *Mixing of solids*, Kluwer Academic Publishers, 2000.
- [209] E. Yasa, J. Deckers, T. Craeghs, M. Badrossamay, Investigation on occurrence of elevated edges in selective laser melting, in: *Solid Free. Fabr. Symp.*, Austin, TX, 2009: pp. 180–192.
<https://pdfs.semanticscholar.org/396c/c2ff5b27151a3db4d257fe9daea3275d5e63.pdf>
 (accessed September 14, 2020).
- [210] I. Yadroitsev, I. Smurov, Surface morphology in selective laser melting of metal powders, in: *Phys. Procedia*, Elsevier, 2011: pp. 264–270. doi:10.1016/j.phpro.2011.03.034.
- [211] S.D. Jadhav, S. Dadbakhsh, L. Goossens, J.P. Kruth, J. Van Humbeeck, K. Vanmeensel, Influence of selective laser melting process parameters on texture evolution in pure copper, *J. Mater. Process. Technol.* 270 (2019) 47–58. doi:10.1016/j.jmatprotec.2019.02.022.
- [212] M. Colopi, L. Caprio, A.G. Demir, B. Previtali, Selective laser melting of pure Cu with a 1

- kW single mode fiber laser, in: *Procedia CIRP*, Elsevier B.V., 2018: pp. 59–63. doi:10.1016/j.procir.2018.08.030.
- [213] T.Q. Tran, A. Chinnappan, J.K.Y. Lee, N.H. Loc, L.T. Tran, G. Wang, V.V. Kumar, W.A.D.M. Jayathilaka, D. Ji, M. Doddamani, S. Ramakrishna, 3D Printing of Highly Pure Copper, *Metals (Basel)*. 9 (2019) 756. doi:10.3390/met9070756.
- [214] G. Strano, L. Hao, R.M. Everson, K.E. Evans, Surface roughness analysis, modelling and prediction in selective laser melting, *J. Mater. Process. Technol.* 213 (2013) 589–597. doi:10.1016/j.jmatprotec.2012.11.011.
- [215] X. Yan, C. Chang, D. Dong, S. Gao, W. Ma, M. Liu, H. Liao, S. Yin, Microstructure and mechanical properties of pure copper manufactured by selective laser melting, *Mater. Sci. Eng. A*. 789 (2020) 139615. doi:10.1016/j.msea.2020.139615.
- [216] R. Li, J. Liu, Y. Shi, L. Wang, W. Jiang, Balling behavior of stainless steel and nickel powder during selective laser melting process, *Int. J. Adv. Manuf. Technol.* 59 (2012) 1025–1035. doi:10.1007/s00170-011-3566-1.
- [217] D. Gu, Y. Shen, Balling phenomena in direct laser sintering of stainless steel powder: Metallurgical mechanisms and control methods, *Mater. Des.* 30 (2009) 2903–2910. doi:10.1016/j.matdes.2009.01.013.
- [218] L. Scime, J. Beuth, Anomaly detection and classification in a laser powder bed additive manufacturing process using a trained computer vision algorithm, *Addit. Manuf.* 19 (2018) 114–126. doi:10.1016/j.addma.2017.11.009.
- [219] C.J. Paciorek, M.J. Schervish, Nonstationary Covariance Functions for Gaussian Process Regression, *Adv. Neural Inf. Process. Syst.* 16 (2004) 273–280. <http://papers.nips.cc/paper/2350-nonstationary-covariance-functions-for-gaussian-process-regression.pdf> (accessed August 31, 2020).
- [220] J.M. Ver Hoef, R.P. Barry, Constructing and fitting models for cokriging and multivariable spatial prediction, *J. Stat. Plan. Inference.* 69 (1998) 275–294. doi:10.1016/s0378-3758(97)00162-6.

NOTE

Material in this thesis has been derived from DOI:

10.1016/j.msea.2020.139050; 10.1016/j.mfglet.2020.12.002; 10.1016/j.addma.2021.101836

Appendices

Appendix A – Supplementary figures

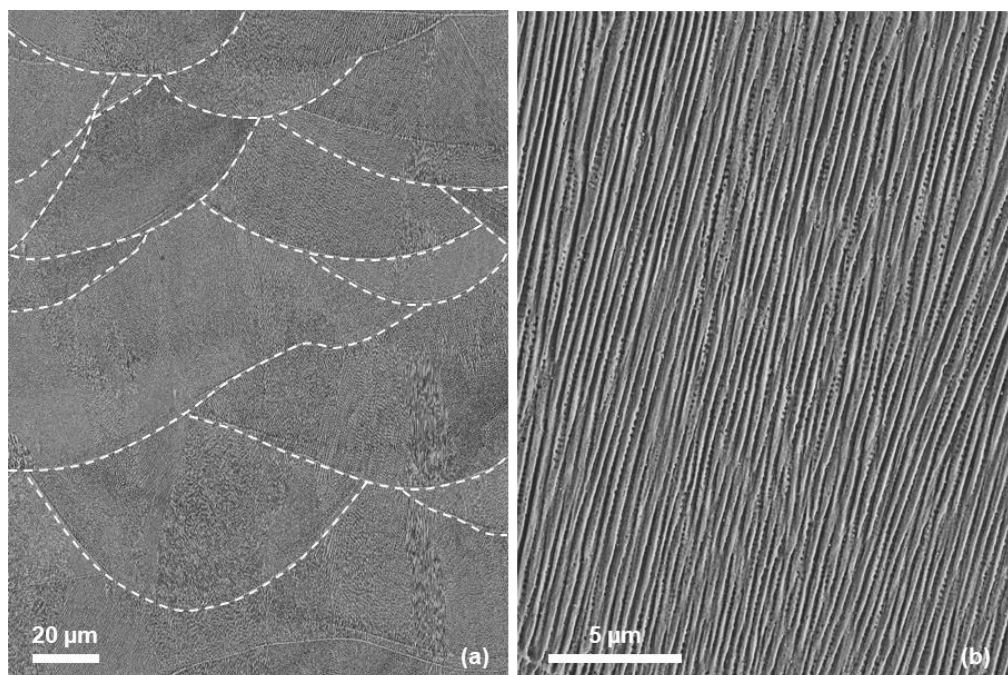


Fig. A1. An SEM image of HX microstructure. (a) Melt pool boundaries are shown in white dashed lines. According to this image the melt pool depth and width are estimated to be 60 μm and 100 μm , respectively. (b) Primary dendritic arm spacing is measured to be $0.4 \pm 0.03 \mu\text{m}$.

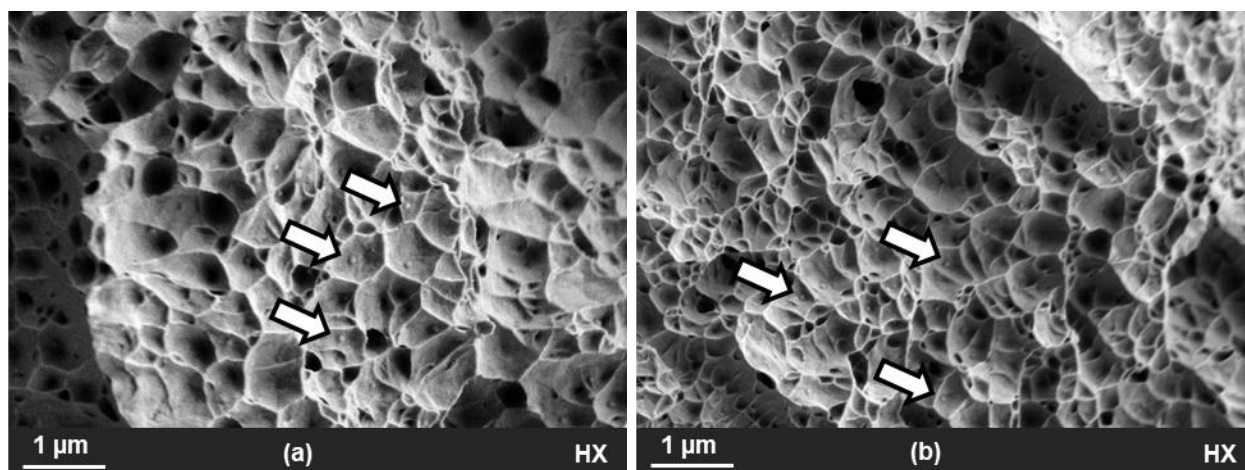


Fig. A2. SEM image of fracture surfaces obtained from HX samples (a,b). Submicron intermetallic inclusions are indicated by white arrows. It is hypothesized that defects found on grain boundaries are artifacts from the extraction of these intermetallic inclusions during sample preparation.

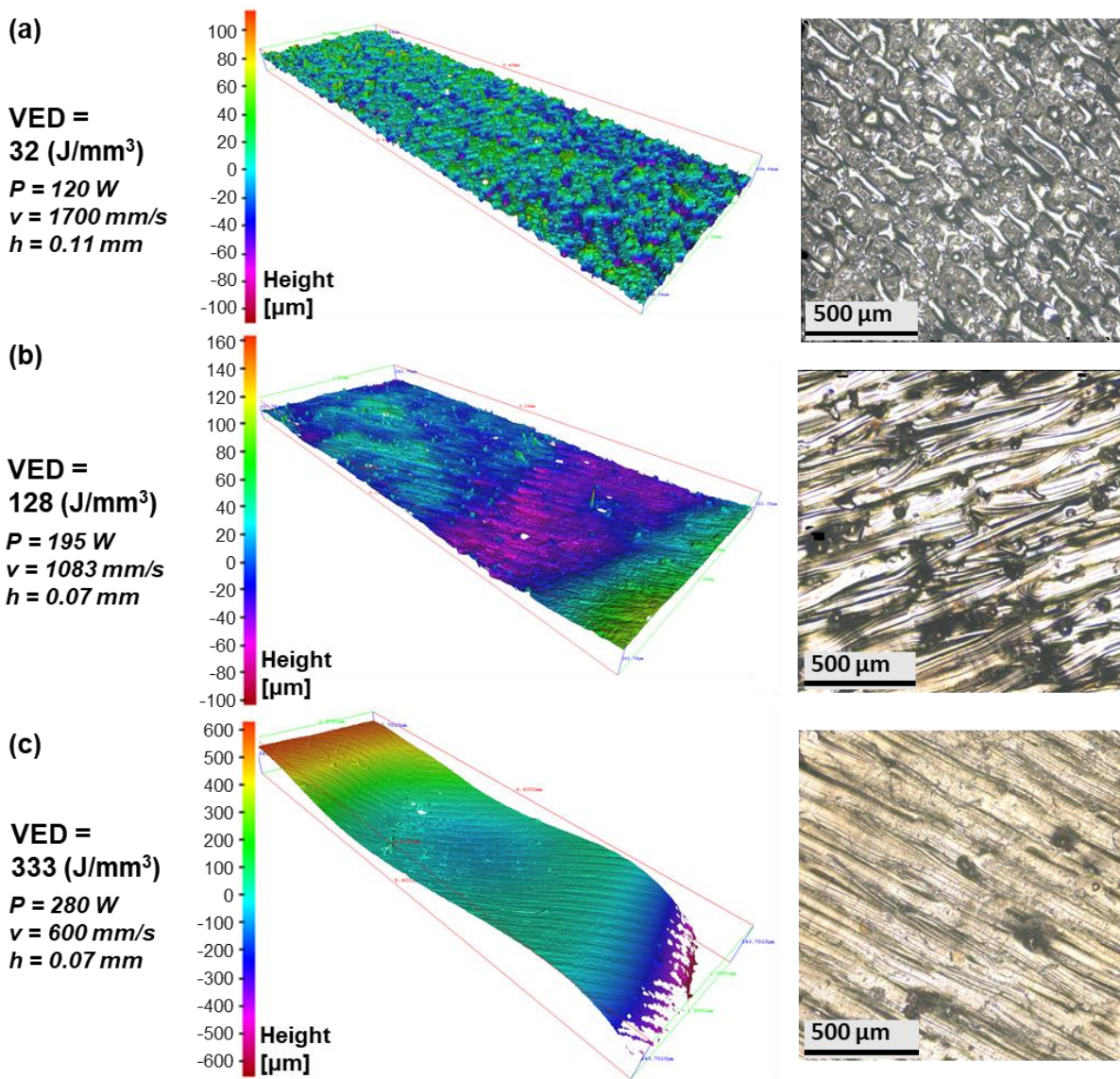


Fig. A3. Optical images and 3D surface profiles of 316L samples manufactured at (a) VED = 32 (J/mm³), (b) VED = 128 (J/mm³), and (c) VED = 333 (J/mm³).

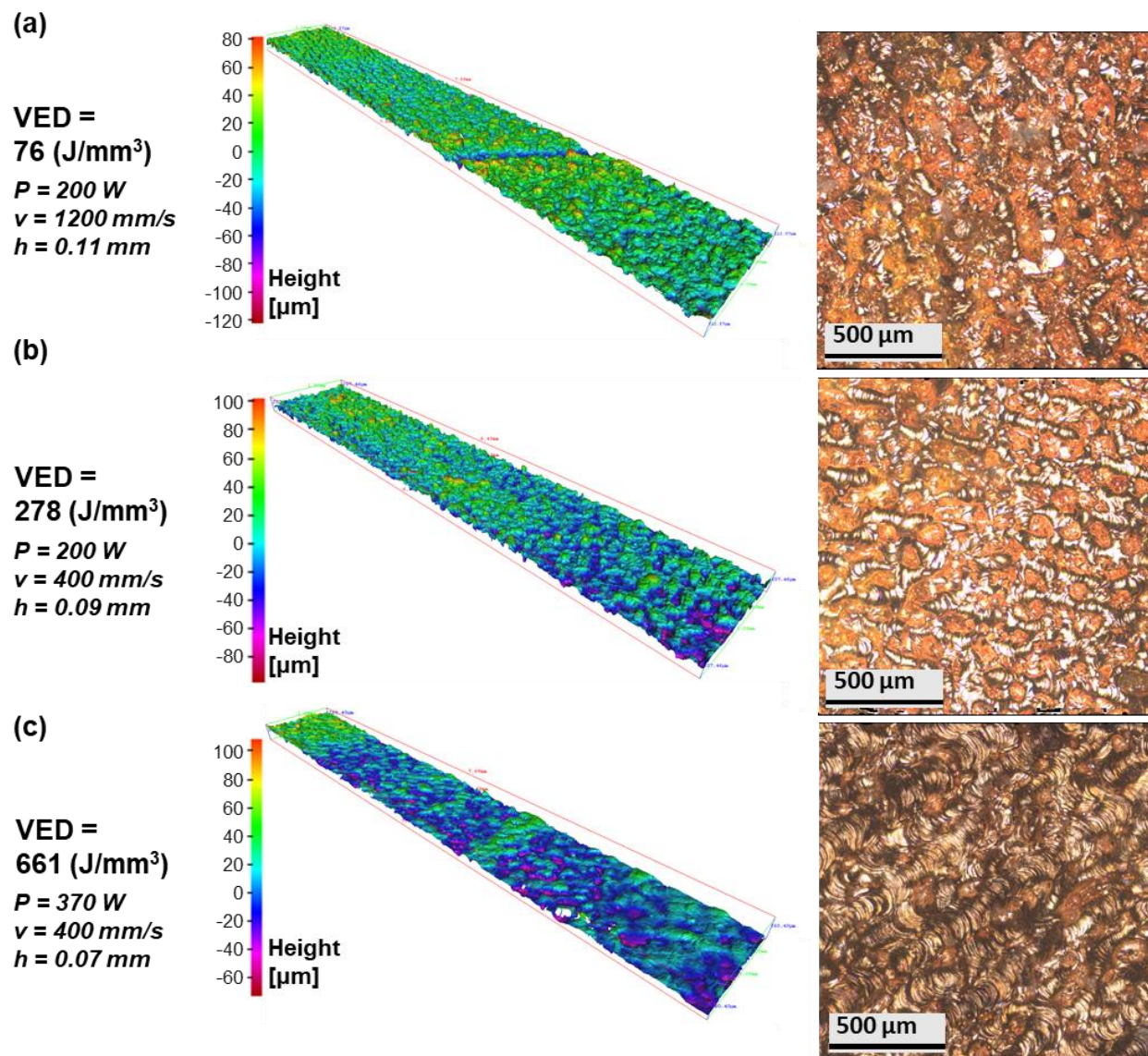


Fig. A4. Optical images and 3D surface profiles of Cu samples manufactured at (a) VED = 76 (J/mm³), (b) VED = 278 (J/mm³), and (c) VED = 661 (J/mm³).

Appendix B – Mixing

Powders were weighted according to the target mass fractions and transported to glass containers for mixing. Retsch PM400 planetary Ball Mill system was used as a tumbling mixer. To achieve a homogeneous mixture, several different mixing parameters were chosen. After each run, mixture was tested for homogeneity.

Table B1 shows the mixing parameters that resulted in a mixture with a satisfactory level of homogeneity. To test for homogeneity, three identically sized samples were taken from the mixture using powder thief method while the mixture was in motion. Samples were taken from top, middle and bottom of the mixture. For each sample, distribution of copper within 316L was qualitatively examined using Energy Dispersive X-Ray Spectroscopy (EDS). Iron and copper were chosen as representative elements for each powder. **Fig. B1** shows the EDS results. As evident by the color maps, particles are distributed uniformly within the field of view indicating a homogeneous mixture. It should be noted that in the strictest sense, mixtures always remain heterogeneous [208]. In addition to homogeneity, mixture had to be tested for particle agglomerates and morphology. Average ECD and aspect ratio of 316L, Cu and their mixtures are compared in **Fig. B2** to ensure particle morphology and size were not adversely affected during mixing. Overall, results suggest that the mixing process was able to produce homogeneous mixtures of 316L-Cu without altering the powder characteristics.

Table B1. Mixing parameters.

Speed (rpm)	Time (min)	Intervals	Rotation	Rest (sec)
200	6	5	Alternating	1

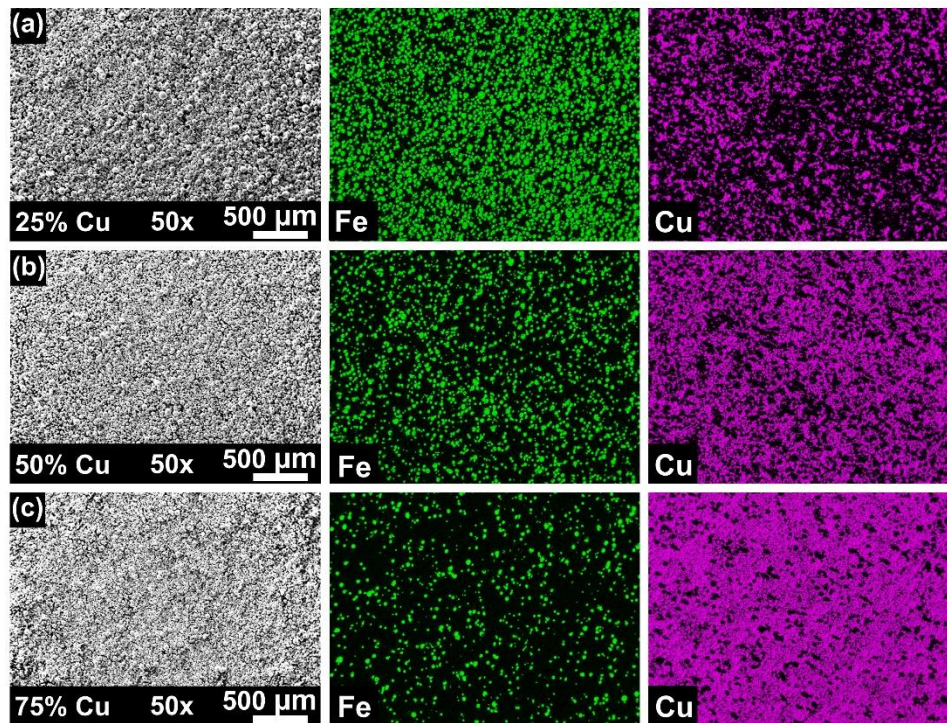


Fig. B1. Representative EDS scans of 316L-Cu mixtures at mass fraction of (a) 0.25, (b) 0.50, and (c) 0.75.

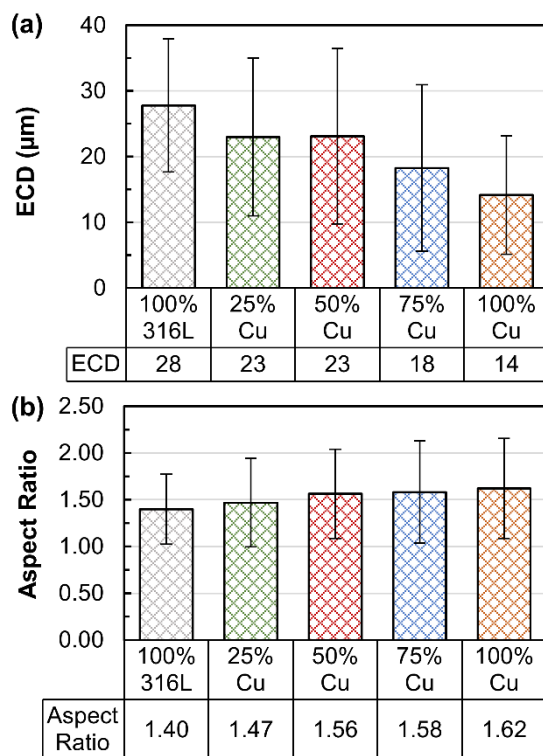


Fig. B2. (a) Comparison of average ECDs. (b) Comparison of average aspect ratios.

Appendix C – Construction of Covariance Function

We construct $f(s)$ using a convolution process to borrow information from the training observations and account for nontrivial commonalities in the data. This construction enables a highly flexible covariance structure that can handle heterogeneity in observed process parameters. More specifically, we propose sharing multiple independent Gaussian white noise processes $\{X_m(s): m \in I\}$ between the target material function $f_{316L-Cu}(s)$ and materials in the training database $\{f_i(s): i = 316L, Cu\}$. Since the latent functions are drawn from a Gaussian process, and if we share these latent functions across all material outputs, then all outputs can be expressed as a jointly distributed Gaussian process. More specifically, all outputs $\{y_i(s): i \in I\}$ are constructed as:

$$\begin{aligned} y_{316L-Cu}(s) &= f_{316L-Cu}(s) + \epsilon_{316L-Cu}(s) \\ &= \sum_{m \in I} k_{m,316L-Cu}(s) * X_m(s) + \epsilon_{316L-Cu}(s) \end{aligned} \quad (C1)$$

$$y_i(s) = f_i(s) + \epsilon_i(s) = k_{i,i}(s) * X_i(s) + \epsilon_i(s), i = 316L, Cu$$

Where $*$ defines a kernel convolution $k_{m,i}(s) * X_m(s) = \int_{-\infty}^{+\infty} k_{m,i}(s - \mathbf{u})X_m(\mathbf{u})d\mathbf{u}$, $k_{i,i}$'s are the kernels connecting latent function X_i to output y_i , and $k_{i,316L-Cu}$ s are the kernels connecting the latent function X_i to $y_{316L-Cu}$. In order to derive the covariance functions, we use Gaussian kernels [219] as follows:

$$k_{mi}(s) = \frac{\alpha_{mi}\sqrt{|\Lambda_{mi}|}}{\sqrt[4]{\pi^d}} \exp\left\{-\frac{1}{2}(s - \mu_{mi})^T \Lambda_{mi}(s - \mu_{mi})\right\} \quad (C2)$$

Finally, following the construction in [219,220] the covariance function can be derived as follows:

$$\text{cov}_{ij}^f(s, s') = \sum_m \frac{2^{\alpha/2} \alpha_{mi} \alpha_{mj}}{\sqrt{|\Psi|}} \exp\left\{-\frac{1}{2}(\mathbf{d} - (\mu_{mi} - \mu_{mj}))^T \Psi^{-1}(\mathbf{d} - (\mu_{mi} - \mu_{mj}))\right\} \quad (C3)$$

Where $\mathbf{d} = s_i - s_j$ is a spatial separation vector between two locations s_i and s_j , $\Psi^{-1} = (\Lambda_{mi}^{-1} + \Lambda_{mj}^{-1})^{-1} = \Lambda_{mi}(\Lambda_{mi} + \Lambda_{mj})^{-1}\Lambda_{mj}$, α_{mi} , α_{mj} , μ_{mi} and μ_{mj} are kernels parameters.

Given $\text{cov}_{ij}^f(s, s')$, and since $\text{cov}_{ij}^y(y_i(s), y_j(s')) = \text{cov}_{ij}^f(s, s') + \text{cov}_{ij}^{\epsilon}(s, s')\tau_{ij}$, the covariance between all datapoints of any two output i and j can be written as:

$$\mathbf{\Omega}_{p_i \times p_j}^{(ij)} = \begin{pmatrix} \text{cov}_{ij}^f(\mathbf{s}_{i1} - \mathbf{s}_{j1}) & \dots & \text{cov}_{ij}^f(\mathbf{s}_{i1} - \mathbf{s}_{jp_j}) \\ \vdots & \ddots & \vdots \\ \text{cov}_{ij}^f(\mathbf{s}_{ip_i} - \mathbf{s}_{j1}) & \dots & \text{cov}_{ij}^f(\mathbf{s}_{ip_i} - \mathbf{s}_{jp_j}) \end{pmatrix} + \mathbf{\Sigma}\boldsymbol{\tau}_{ij} \quad (\text{C4})$$

where $\mathbf{\Sigma}$ is a diagonal matrix with elements σ_ϵ^2 representing measurement noise. Let $P = \sum_{i \in I} p_i$ be the total number of observations from all outputs. The resulting covariance matrix established through a convolution process is written as:

$$\mathbf{\Omega}_{P \times P} = \begin{pmatrix} \mathbf{\Omega}_{p_{316L} \times p_{316L}}^{(316L,316L)} & \mathbf{0}_{p_{316L} \times p_{Cu}} & \mathbf{\Omega}_{p_{316L} \times p_{316L-Cu}}^{(316L,316L-Cu)} \\ \mathbf{0}_{p_{Cu} \times p_{316L}} & \mathbf{\Omega}_{p_{Cu} \times p_{Cu}}^{(Cu,Cu)} & \mathbf{\Omega}_{Cu \times p_{316L-Cu}}^{(Cu,316L-Cu)} \\ \mathbf{\Omega}_{p_{316L-Cu} \times p_{316L}}^{(316L-Cu,316L)} & \mathbf{\Omega}_{p_{316L-Cu} \times p_{Cu}}^{(316L-Cu,Cu)} & \mathbf{\Omega}_{p_{316L-Cu} \times p_{316L-Cu}}^{(316L-Cu,316L-Cu)} \end{pmatrix} \quad (\text{C5})$$

Our joint model now can be parametrized through the kernel parameters in the covariance function denoted as $\boldsymbol{\theta}$, and the measurement noise term σ_ϵ . We denote the observations from all outputs by $\mathbf{y} = [y_{316L}^T, y_{Cu}^T, y_{316L-Cu}^T]^T$, then the log-likelihood of the joint multivariate Gaussian process is given by:

$$l(\boldsymbol{\theta}, \sigma_\epsilon; \mathbf{y}) = -\frac{P}{2} \log(2\pi) - \frac{1}{2} \log |\mathbf{\Omega}_{P \times P}| - \frac{1}{2} \mathbf{y}^t \mathbf{\Omega}_{P \times P}^{-1} \mathbf{y} \quad (\text{C6})$$

The parameters' estimate can be obtained by maximizing the log-likelihood function in **Eq. C6**. Either multivariate optimization algorithms can be used (Nelder-Mead simplex, conjugate gradient, etc.) to directly maximize the log-likelihood function and Monte Carlo methods can be utilized to simulate the maximum *a posteriori* estimate of $\boldsymbol{\theta}$ and σ_ϵ . Given $\hat{\boldsymbol{\theta}}$ and $\hat{\sigma}_\epsilon$, the joint Gaussian distribution of the observed values \mathbf{y} and the estimated value at a new input point \mathbf{s}^* is expressed as:

$$\begin{pmatrix} \mathbf{y} \\ \mathbf{y}_{316L-Cu}(\mathbf{s}^*) \end{pmatrix} \sim N \left(\mathbf{0}, \begin{bmatrix} \hat{\mathbf{\Omega}}_{P \times P} & \hat{\boldsymbol{\eta}}(\mathbf{s}^*) \\ \hat{\boldsymbol{\eta}}^T(\mathbf{s}^*) & \text{cov}_{316L-Cu,316L-Cu}^f(\mathbf{s}^*, \mathbf{s}^*) + \hat{\sigma}_\epsilon^2 \end{bmatrix} \right) \quad (\text{C7})$$

where $\hat{\boldsymbol{\eta}}^T(\mathbf{s}^*) = [\hat{\boldsymbol{\eta}}_{316L}^T(\mathbf{s}^*), \hat{\boldsymbol{\eta}}_{Cu}^T(\mathbf{s}^*), \hat{\boldsymbol{\eta}}_{316L-Cu}^T(\mathbf{s}^*)]^T$ and $\hat{\boldsymbol{\eta}}_i^T(\mathbf{s}^*) = [\text{cov}_{316L-Cu,i}^f(\mathbf{s}^* - \mathbf{s}_{i1}), \text{cov}_{316L-Cu,i}^f(\mathbf{s}^* - \mathbf{s}_{i2}), \dots, \text{cov}_{316L-Cu,i}^f(\mathbf{s}^* - \mathbf{s}_{ip_i})]$.